Abstract

A precise measurement of the pion beta decay rate will allow accurate testing of the unitarity of the Cabbibo-Kobayashi-Maskawa quark mixing matrix, and of the Conserved Vector Current Hypothesis. The PIBETA collaboration intends to measure this decay rate with an accuracy of better than 0.5%, using a calorimeter comprised of 240 pure CsI crystals. Extensive calibrations of the CsI crystals have been done using cosmic muons. Further studies of the calorimeter response have been made using monoenergetic 70 MeV beam positrons, and using the box spectrum of photons ranging in energy from 55-83 MeV from the single charge exchange reaction $\pi^- p \to \pi^0 n \to \gamma\gamma n$. Finally, a measurement of the Panofsky Ratio, defined as the ratio of the rate of single charge exchange to that of radiative pion capture $\pi^- p \to \gamma n$ in pionic hydrogen, has been made.

Contents

Acknowledgments

I would like to thank my research advisor Dr. Dinko Počanić for his inpsiration and direction throughout my membership in the PIBETA collaboration. His knowledge, enthusiasm, and careful advice have been a very positive and helpful influence for the past three years. I would also like to thank Dr. Emil Frlež for sharing his expertise on numerous topics, especially the cosmic muon tomography project, and for many valuable suggestions during the editing process of this work. Many thanks to Dr. Stefan Ritt for his timely and useful advice and help with data management and calibration algorithms, to Dr. Bernward Krause, for daily helpful discussions about the tomography project and data analysis, and to Thomas Flügel for numerous constructive conversations. I would also like to thank Dr. Ralph Minehart for his suggestions toward the editing and completion of this work, and for several years of good physics instruction.

Thank you Wright, Dori, and Sarah Doyle for welcoming me on various holidays and non-holidays, and for housing me indefinitely and on short notice. Thank you Ken, Victoria, and Anne for your wonderful friendships, and for all of the fun and support you've provided. Thank you Supriya, Drew, and Warren for all of the dinner breaks, ice skating breaks, and for your understanding and friendship when it counted. To my volleyball team: Ken, Lori, Krissy, Kaitie and Ishi, thanks for all of your entertainment and great volleyball.

I would especially like to thank my family for their support and companionship throughout my education.

The Panofsky Ratio, and the Response of the PIBETA Calorimeter to Photons and Positrons

Penelope Lee Slocum
Amherst, New Hampshire

B.A., University of Virginia, 1991
M.A., University of Virginia, 1995

A Dissertation Presented to the Graduate
Faculty of the University of Virginia
in Candidacy for the Degree of
Doctor of Philosophy

Department of Physics

University of Virginia
January 1999

Chapter 1

Motivation

1.1 Introduction

The PIBETA collaboration is focused on making a precise measurement of the pion beta decay rate, $\pi^+ \to \pi^0 e^+ \nu$. Because the pion beta decay is a relatively simple $0^- \to 0^-$ transition, and its radiative corrections are well understood, this measurement will provide a stringent test of the theoretical components of the decay. Specifically, the results will test the Conserved Vector Current Hypothesis, as well as the unitarity of the Cabbibo Kobayashi Maskawa (CKM) quark mixing matrix.

In order to measure the pion beta decay rate successfully, a portion of the PIBETA calorimeter has been tested with a measurement of the Panofsky Ratio. This ratio is defined as the ratio between the rate of single charge exchange and that of radiative pion capture for $\pi^- p$ atoms. The single charge exchange reactions are defined as [19]

$$
\begin{aligned}
&\pi^- + p \to \pi^0 n \\
&\pi^- + p \to \gamma + \gamma + n \\
&\pi^- + p \to e^+ + + e^- + n,
\end{aligned}
\tag{1.1}
$$

and the radiative pion capture reactions are

$$\pi^- + p \rightarrow \gamma n$$
$$\pi^- + p \rightarrow e^+ + e^- + \gamma + n. \qquad (1.2)$$

1.1.1 CKM Matrix

The CKM quark mixing matrix is the transformation between the strong interaction quark eigenstates

$$\begin{pmatrix} u \\ d \end{pmatrix} \begin{pmatrix} c \\ s \end{pmatrix} \begin{pmatrix} t \\ b \end{pmatrix},$$

and the weak interaction quark eigenstates,

$$\begin{pmatrix} u \\ d' \end{pmatrix} \begin{pmatrix} c \\ s' \end{pmatrix} \begin{pmatrix} t \\ b' \end{pmatrix}.$$

The transformation between these strong and weak mass eigenstates takes the form:

$$\begin{pmatrix} d' \\ s' \\ b' \end{pmatrix} = \begin{pmatrix} U_{ud} & U_{us} & U_{ub} \\ U_{cd} & U_{cs} & U_{cb} \\ U_{td} & U_{ts} & U_{tb} \end{pmatrix} \begin{pmatrix} d \\ s \\ b \end{pmatrix}$$

A test of the unitarity of the CKM matrix would serve to limit certain extensions to the current Standard Model of elementary particles. This test can be performed most reliably by a measure of the sum of the elements of the top row of the matrix: $|U_1|^2 = |U_{ud}|^2 + |U_{us}|^2 + |U_{ub}|^2$. If the sum $|U_1|^2$ is equal to unity, then the matrix is unitary. Using the accepted value for U_{us} and the limits on U_{ub}, in combination with the value of U_{ud} extracted from nuclear beta decay, one finds the result $|U_1|^2 = |U_{ud}|^2 + |U_{us}|^2 + |U_{ub}|^2 = 0.9962 \pm 0.0016$. This value includes the most reliable nuclear structure dependent corrections, and is lower than the Standard Model prediction by 2.4σ.

A second evaluation of $|U_1|^2$, using the value for U_{ud} extracted from neutron beta decay, brings the value of $|U_{ud}|^2 + |U_{us}|^2 + |U_{ub}|^2$ up to 1.0096 ± 0.0044, which is higher than the Standard Model prediction by 2.2σ [15].

A precise extraction of U_{ud} is needed to resolve the discrepancy between these two calculations of $|U_1|^2$. This will be accomplished with the measurement of the pion beta decay rate $\tau_{\pi\beta}$, as

$$\frac{1}{\tau_{\pi\beta}} \propto |U_{ud}|^2 {G_V}^2, \tag{1.3}$$

where G_V is the weak vector coupling constant.

1.1.2 Conserved Vector Current Hypothesis

Because the positive and neutral pions are members of an isospin multiplet, it is possible to describe them mathematically with the ladder operators in isospin space. The ladder operators take the form

$$T_{\pm} = \sqrt{2} \sum_k \left[a_0^*(\mathbf{k}) a_{\mp}(\mathbf{k}) + {a_{\pm}}^*(\mathbf{k}) a_0(\mathbf{k}) \right], \tag{1.4}$$

where $a_0(\mathbf{k})$ ($a_0^*(\mathbf{k})$) is the absorption (emission) operator for the neutral pion, and $a_{\pm}(\mathbf{k})$ (${a_0}^*(\mathbf{k})$) are the absorption (emission) operators for the charged pions. Applying the operator T_+ to a state with one pion with a given charge produces another state with a pion of the same momentum but with the charge increased by one unit. [9]

Using the isospin ladder operator formalism, the vector part of the interaction for nuclear beta decay [9] becomes:

$$\begin{aligned} j_\mu^\beta(x) &= g\overline{\Psi}_p(x)\gamma_\mu\Psi_n(x) \\ &= -\frac{g}{\sqrt{2}}\overline{\Psi}(x)\gamma_\mu\tau^{(+)}\Psi(x) \\ &= -\frac{g}{2\sqrt{2}}\left[\overline{\Psi}(x), \gamma_\mu\tau^{(+)}\Psi(x)\right]. \end{aligned} \tag{1.5}$$

If one compares Equ. 1.5 with the electromagnetic current of a nucleon system, which takes the form

$$\begin{aligned} j_\mu^{nucl,el}(x) &= \frac{ie}{2}\left[\overline{\Psi}_p(x), \gamma_\mu \Psi_p(x)\right] \\ &= \frac{ie}{4}\left[\overline{\Psi}(x), \gamma_\mu(1+\tau_3)\Psi(x)\right] \\ &= \frac{ie}{4}\left[\overline{\Psi}(x), \gamma_\mu \Psi(x)\right] + \frac{ie}{4}\left[\overline{\Psi}(x), \gamma_\mu \tau_3 \Psi(x)\right], \end{aligned} \tag{1.6}$$

it is apparent that the second term in Equ. 1.6 can be understood as another component of the nuclear beta decay vector current in Equ. 1.5. For further clarification, the vector current from Equ. 1.5 may be written as

$$j_\mu^\beta(x) = \frac{ig}{e}\sqrt{2}\,\vec{\mathbf{j}}_\mu^{\,nucl,(+)}(x). \tag{1.7}$$

Upon further study of Equ. 1.6, one finds that the electromagnetic current of the nucleon system is not a conserved quantity [9]. However, if one adds another term corresponding to the pion electromagnetic current, a continuity equation is created:

$$\frac{\partial j_\mu^{el}(x)}{\partial x_\mu} = 0 = \frac{\partial j_\mu^{nucl}(x)}{\partial x} + \frac{\partial j_\mu^\pi}{\partial x_\mu} \tag{1.8}$$

Because this added term for the pion electromagnetic current can be shown to have only an isotopic vector part [9], the continuity equation 1.8 can be written as

$$\frac{\partial j_\mu^{nucl,S}(x)}{\partial x_\mu} + \frac{\partial}{\partial x_\mu}\left[\vec{\mathbf{j}}_\mu^{\,nucl,(0)}(x) + \vec{\mathbf{j}}_\mu^{\,\pi,(0)}(x)\right] = 0, \tag{1.9}$$

where $j_\mu^{nucl,S}(x)$ is the isotopic scalar part of the nucleon system electromagnetic current, and $\vec{\mathbf{j}}_\mu^{(0)}(x)$ is one component of the appropriate vector electromagnetic current.

In order to be invariant under rotations in isospin space, each of the two terms in Equ. 1.9 must be conserved separately. Consequently, each component of the vector term must also be conserved. Hence, the following conservation law must be true:

$$\frac{\partial}{\partial x_\mu}\left[\vec{\mathbf{j}}_\mu^{nucl,(\pm)}(x)+\vec{\mathbf{j}}_\mu^{\pi,(\pm)}(x)\right]=0. \tag{1.10}$$

The addition of the pion electromagnetic current term in Equ. 1.8, which results in the conservation law of Equ. 1.10, has implications for the form of the beta decay electromagnetic vector current given in Equ. 1.5. Specifically, in order to explain the apparent equality of the weak interaction vector coupling constants G_V in nuclear beta decay and in muon decay, a corresponding pion electromagnetic current term should be added to the beta decay nucleon electromagnetic current in Equ. 1.5.

This added term in the expression for $j_\mu^\beta(x)$ implies the existence of a new contribution to the weak interaction Hamiltonian. The new contribution drives the beta decay of the pion, $\pi^+ \rightarrow \pi^0 e^+ \nu_e$ or $\pi^- \rightarrow \pi^0 e^- \nu_e$. [9] By measuring the pion beta decay rate precisely, and comparing it with the theoretical value obtained from the modified weak Hamiltonian, one can determine whether the CVC hypothesis is true.

1.1.3 Radiative Correction

The calculation of radiative corrections to the pion beta decay rate can be taken from the nuclear independent radiative corrections to $0^+ \rightarrow 0^+$ transitions in nuclear beta decay. At $O(\alpha)$, these corrections neglect the strong interaction effects in nuclear beta decay, and can be applied to the purely weak pion beta decay. This radiative correction function is based on a function $g(E, E_m, m)$

which has been derived by Sirlin [12], and takes the form

$$\begin{aligned}
g(E,E_m,m) &= 3ln\left(\frac{m_p}{m}\right) - \frac{3}{4} + 4\left[\frac{\tanh^{-1}\beta}{\beta} - 1\right] \times \\
&\left[\frac{(E_m - E)}{3E} - \frac{3}{2} + ln\frac{2(E_m - E)}{m}\right] + \frac{4}{\beta}L\left(\frac{2\beta}{1+\beta}\right) \\
&+ \frac{1}{\beta}tanh^{-1}\beta\left[2(1+\beta^2) + \frac{(E_m - E)^2}{6E^2} - 4\tanh^{-1}\beta\right] \qquad (1.11)
\end{aligned}$$

where m is the electron mass, E_m is the electron end-point energy, p is the electron momentum, $\beta = p/E$, and $L(x)$ is the Spence function:

$$L(x) = \int_0^x \frac{ln(1-t)}{t}\,dt \qquad (1.12)$$

Integrating the Spence function from 0 to $\frac{2\beta}{1+\beta}$, one obtains $L = -1.5934$.

When applied to pion beta decay and averaged over the electron spectrum, the function $\overline{g}(E,E_m,m)$ becomes [18]

$$\overline{g}(E,E_m,m) = \frac{\int_{m_e}^{E_m} \frac{(E_m-E)^2 p_e E}{\left[1+\frac{2m_+}{m_0}(E_m-E)\right]} g(E,E_m,m)\,dE}{\int_{m_e}^{E_m} \frac{(E_m-E)^2 p_e E}{\left[1+\frac{2m_+}{m_0}(E_m-E)\right]}\,dE} \qquad (1.13)$$

where m_+ is the π^+ mass and m_0 is the π^0 mass. To a good approximation, the denominator is found to be 57.127 $(MeV)^5$ [12].

Integrating the numerators numerically over the electron energy, one obtains $\overline{g}(E,E_m,m) = 9.760$. This can be compared with the asymptotic result for large E_m, which neglects recoil [18],

$$\overline{g}(E,E_m,m) \cong 3ln\left(\frac{m_p}{2E_m}\right) + \frac{81}{10} - \frac{4\pi^2}{3} = 8.868 \qquad (1.14)$$

The radiative correction is derived by Marciano and Sirlin [13] and takes the form

$$\{1 + \frac{\alpha}{2\pi}\left[ln\left(\frac{m_p}{m_A}\right) + 2C\right] - \frac{\alpha(m_p)}{2\pi}\left[\overline{g}(E_m) + A_g\right]\}S(m_p,m_z) \qquad (1.15)$$

where $S(m_p, m_z)$ is a QED short-distance enhancement factor equal to 1.02256, and $\alpha(\mu)$ is a running QED coupling which satisfies

$$\mu \frac{d}{d\mu} \alpha\mu \;=\; b_0 \alpha^2(\mu) \;+ \text{higher orders} \tag{1.16}$$

such that $\alpha(0) = 1/137.089$ and $\alpha(m_p) = 1/133.93$. A_g is a small perturbative QCD correction estimated to be -0.34, and C is a nuclear structure-dependent correction which is 0 for $0^+ \rightarrow 0^+$ transitions. m_A is a low energy cutoff applied to the short-distance part of the γW box diagram, and ranges from 400 MeV to 1600 MeV. Using this range of m_A, the radiative correction to superallowed $0^+ \rightarrow 0^+$ Fermi transition rates is found to be between 1.0334 and 1.0350. [13]

1.2 Panofsky Ratio

The Panofsky Ratio value is of interest because it connects the pion-nucleon scattering amplitude to the pion photoproduction amplitude, and it provides a value with which several other low energy pion relations may be tested. For example, the ratio R is defined as

$$R = \frac{\sigma(\gamma n \rightarrow \pi^- p)}{\sigma(\gamma p \rightarrow \pi^+ n)}. \tag{1.17}$$

From this ratio, and the assumption of the invariance of the electromagnetic interaction under time reversal, one can calculate the reaction rate for $\pi^- p \rightarrow \gamma n$.

By extrapolating this calculated reaction rate for $\pi^- p \rightarrow \gamma n$ to threshold, one can use the measured value of the Panofsky Ratio (P) to determine the rate for the pion-nucleon scattering reaction $\pi^- p \rightarrow \pi^0 n$. The resulting equation is

$$\sigma(\pi^- p \rightarrow \pi^0 n) = 2P \cdot (q_\gamma^2 / q_\pi^2) \sigma(\pi^- p \rightarrow \gamma n), \tag{1.18}$$

where q_γ and q_π are the center of mass momentum of the photon and pion, respectively.

One can compare this calculation of $\sigma(\pi^- p \rightarrow \pi^0 n)$ to that obtained from $\pi^{\pm} p$ elastic scattering data. By using the principle of isospin invariance for the extraction of $\sigma(\pi^- p \rightarrow \pi^0 n)$ from the scattering data, and comparing the result with the calculation in Equation 1.18, one can ultimately test the principle of isospin symmetry in the πN system. [19]

In addition to allowing useful calculations of the pion-nucleon scattering amplitude, the Panofsky Ratio reactions produce photons whose energies are comparable to that of the photons produced in the pion beta decay. By measuring the response of the PIBETA calorimeter to the photons resulting from the single charge exchange and pion capture reactions, one can predict the behavior of the calorimeter for the pion beta decay measurement.

1.2.1 Kinematics of Single Charge Exchange and Pion Capture Reactions

In this section, the kinematics of the two main reactions in the Panofsky Ratio will be discussed. It will be shown that the single charge exchange reaction produces a box spectrum of photons ranging in energy from 55 to 83 MeV, and the radiative pion capture reaction emits a monoenergetic photon at 129 MeV.

Single Charge Exchange

From conservation of momentum in the reaction $\pi^- p \rightarrow \pi^0 n$,

$$p_- + p_p = p_0 + p_n, \tag{1.19}$$

where p_-, p_p, p_0, and p_n are the momenta of the negative pion, proton, neutral pion, and neutron, respectively. Assuming that the pionic hydrogen $\pi^- p$ atoms are at rest, and solving for the energies E_0 and E_n of the π^0 and the neutron in the lab frame, one finds

$$E_0 = \frac{(m_- + m_p + E_B)^2 - {m_n}^2 + {m_0}^2}{2\,(m_- + m_p + E_B)} \tag{1.20}$$

$$= 137.9\ MeV \tag{1.21}$$

which corresponds to $\beta_0 = 0.204$, and

$$E_n = m_- + m_p + E_B - E_0 \tag{1.22}$$

$$= 940.0\ MeV, \tag{1.23}$$

where m_-, m_p, m_n, and m_0 are the masses of the negative pion, proton, neutron, and neutral pion, respectively. E_B is the mean binding energy of the pionic hydrogren, and is equal to -0.37±0.08 keV. [6]

In the rest (primed) frame of the π^0, the $\pi^0 \rightarrow \gamma\gamma$ decay produces two anticollinear photons, as shown in Fig. 1.1. In order to calculate the momenta of the photons in the lab frame, one must perform the appropriate transformation. For this purpose, the momentum of the π^0 in the lab (unprimed) frame is defined to be in the **x** direction. Consequently, the boost from the primed frame to the lab frame is along the negative **x** direction, as shown in Fig. 1.1.

In the primed frame, the four-momenta of the two photons take the form:

$$p_1{}' = (E', p'\sin\theta, p'\cos\theta, 0) \tag{1.24}$$

$$p_2{}' = (E', -p'\sin\theta, -p'\cos\theta, 0)\,, \tag{1.25}$$

where $E' = p' = m_0/2 = 67.5$ MeV. Transforming to the lab (unprimed) frame with a boost in the negative **x** direction for $\beta = 0.204$,

$$\begin{pmatrix} E_1 \\ p_{1x} \\ p_{1y} \\ p_{1z} \end{pmatrix} = \begin{bmatrix} \gamma & \gamma\beta & 0 & 0 \\ \gamma\beta & \gamma & 0 & 0 \\ 0 & 0 & 1 & 0 \\ 0 & 0 & 0 & 1 \end{bmatrix} \begin{pmatrix} E' \\ p'\sin\theta \\ p'\cos\theta \\ 0 \end{pmatrix} = \begin{pmatrix} \gamma E' + \gamma\beta p'\sin\theta \\ \gamma\beta E' + \gamma p'\sin\theta \\ p'\cos\theta \\ 0 \end{pmatrix}$$

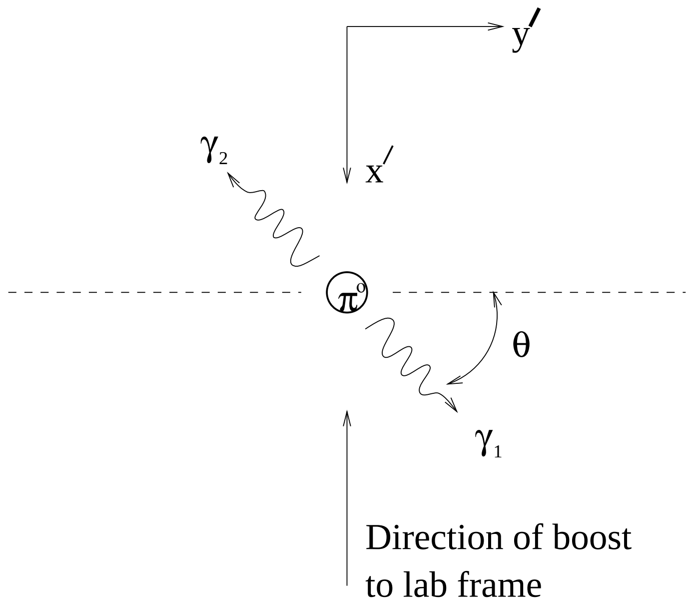

Figure 1.1: *Decay of a neutral pion into two photons, in the rest (primed) frame of the pion.*

and

$$\begin{pmatrix} E_2 \\ p_{2x} \\ p_{2y} \\ p_{2z} \end{pmatrix} = \begin{bmatrix} \gamma & \gamma\beta & 0 & 0 \\ \gamma\beta & \gamma & 0 & 0 \\ 0 & 0 & 1 & 0 \\ 0 & 0 & 0 & 1 \end{bmatrix} \begin{pmatrix} E' \\ -p'\sin\theta \\ -p'\cos\theta \\ 0 \end{pmatrix} = \begin{pmatrix} \gamma E' - \gamma\beta p'\sin\theta \\ \gamma\beta E' - \gamma p'\sin\theta \\ -p'\cos\theta \\ 0 \end{pmatrix}.$$

From the above expressions for p_1 and p_2 in the lab frame, one can see that the energy and momenta of the two photons are completely determined by the angle θ in the primed frame. Because the probability of values for the angle θ is uniform from 0° to 180°, the spectrum of energies for the two photons forms a flat "box" spectrum, ranging from the minimum to the maximum allowed values.

The relative angle ξ between the two photons can be calculated from the general formula for the angle Ψ_{AB} between two vectors $\mathbf{A}$ and $\mathbf{B}$,

$$\cos\Psi_{AB} = \frac{\mathbf{A} \cdot \mathbf{B}}{|\mathbf{A}||\mathbf{B}|}. \tag{1.26}$$

As a result, the expression for ξ takes the form

$$\cos\xi = \frac{(\gamma\beta E' + \gamma p'\sin\theta)(\gamma\beta E' - \gamma p'\sin\theta) + (p'\cos\theta)(-p'\cos\theta)}{\sqrt{(\gamma\beta E' + \gamma p'\sin\theta)^2 + (p'\cos\theta)^2}\sqrt{(\gamma\beta E' - \gamma p'\sin\theta)^2 + (-p'\cos\theta)^2}}$$

Finally, the energy of one photon in the lab frame is plotted against ξ in Fig. 1.2. From the graph, one can see that the photon energies in the lab frame range from 54.9 MeV to 83.0 MeV.

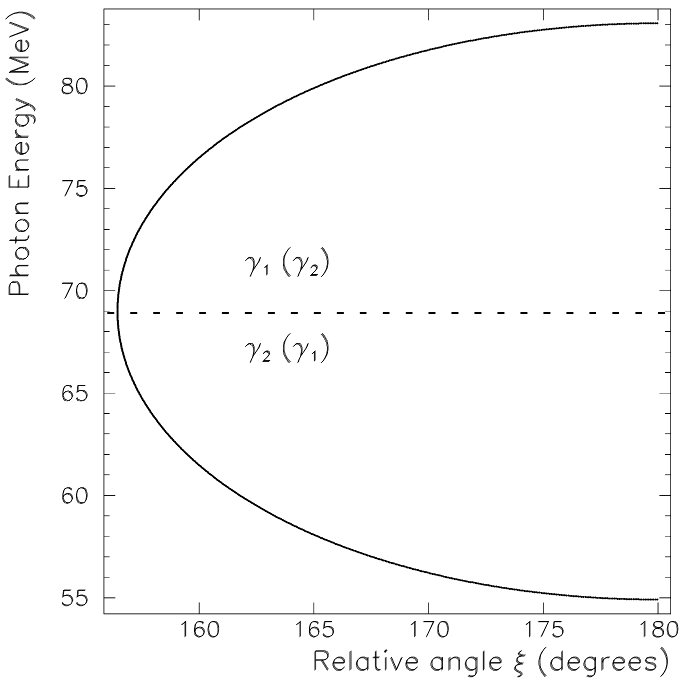

Figure 1.2: *Energy spectrum for photons from the decay $\pi^0 \to \gamma\gamma$ plotted against the relative angle ξ between the two photons, all in the lab frame.*

Radiative Capture

From energy and momentum conservation in the reaction $\pi^- p \rightarrow n\gamma$,

$$E_n = \frac{(m_- + m_p + E_B)^2 + {m_n}^2}{2\,(m_- + m_p + E_B)} \tag{1.27}$$

$$= 948.5\ MeV, \tag{1.28}$$

where E_n is the total energy of the neutron, and all other variables are defined in Section 1.2.1. By energy conservation, the energy of the emitted photon E_γ is found to be

$$E_\gamma = m_- + m_p + E_B - E_n \tag{1.29}$$

$$= 129.4\ MeV. \tag{1.30}$$

Chapter 2

1997 Apparatus and Beam Line

In this chapter the $\pi e1$ beam line, a secondary beam line stemming from the main 590 MeV proton ring cyclotron at the Paul Scherrer Institute, will be discussed. In addition, the CsI and NaI detector arrays, liquid hydrogen target, and beam counters will be introduced.

2.1 $\pi e1$ Beam Line

The $\pi e1$ beam line supplies high intensity pion and muon beams with momenta ranging from 10 to 500 MeV/c. Figure 2.1 shows the layout of the beam line [17].

Two modes of operation are available [17]:

- Mode **A** provides high flux with low momentum resolution. Its momentum is limited by the focusing strength of the first quadrupoles to values lower than 280 MeV/c.
- Mode **B** is a low acceptance, high momentum resolution version up to momenta of 500 MeV/c.

The defining characteristics of the $\pi e1$ beam line are summarized in Table 2.1.

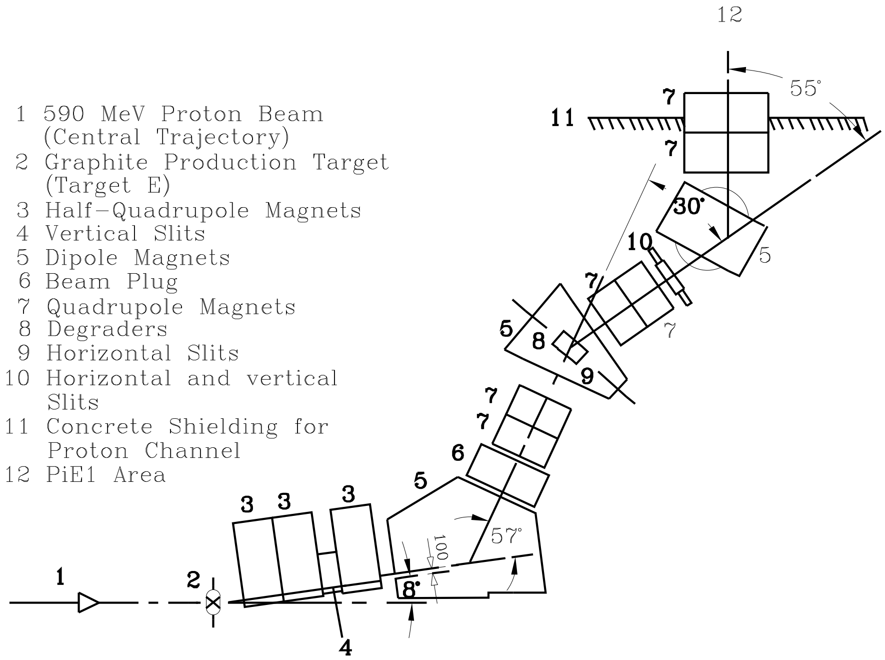

Figure 2.1: *Magnetic elements of* $\pi e1$ *beam line.*

	Mode A	Mode B
Length [m]	16	16
Max. momentum [MeV/c]	280	500
Solid angle [msr]	32	13
Momentum acceptance (FWHM)	7.8 %	8.0 %
Momentum resolution (FWHM)	0.8 %	0.26 %
π^+ stop density $[g^{-1}mA^{-1}s^{-1}]$	2.5 10^7	1.0 10^7

Table 2.1: *Characteristics of the* $\pi e1$ *beam line in Mode* **A** *(high flux) and Mode* **B** *(high momentum resolution).*

In the 1997 data run, the $\pi e1$ beam line was tuned in Mode **B** for 116 MeV/c negative pions. This tune is shown in Figure 2.2 as the output of the TRANSPORT [20] program calculation. In the figure, the top solid line represents the beam envelope in the horizontal (x) direction, and the bottom solid line the beam envelope in the vertical (y) direction. The arrows represent collimators and slits in the beam path, and the dotted line is the momentum dispersion measured in cm/% in the x direction.

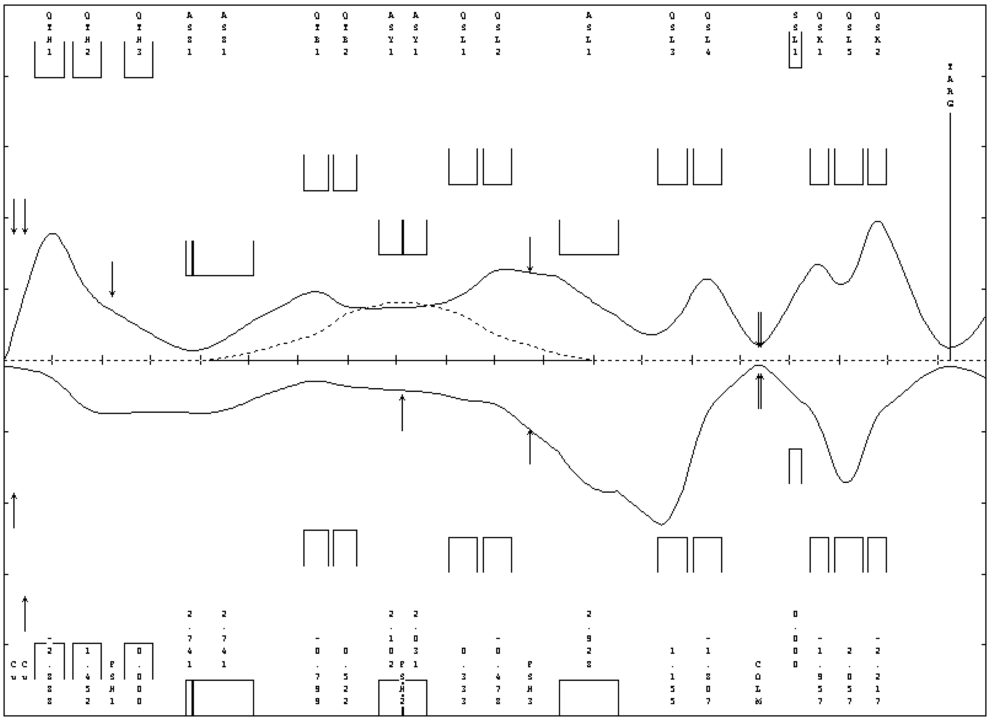

Figure 2.2: *The beam tune for the 1997 data run. The top part of the graph represents the x direction, and the bottom the y direction. The arrows indicate collimation, and the dotted line is the beam momentum dispersion, measured in cm/%. These calculations were made with the TRANSPORT program.*

2.2 1997 Apparatus

2.2.1 CsI Detector

The CsI detector is an array of 44 optically isolated CsI crystals (see Fig. 2.3). This array can be divided into 21 "outer" crystals, which comprise the outer ring of detectors, and 23 "inner" crystals. These 44 crystals are a subset of 240

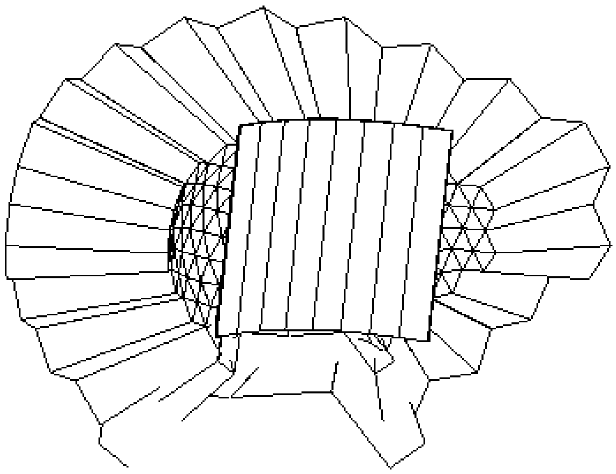

Figure 2.3: *Array of 44 pure CsI crystals used during the 1997 beam time.*

crystals which, when assembled, form a spherical detector covering $\sim 80\%$ of 4π steradians (see Fig. 2.4). The completed sphere has an inner radius of 26.0 cm and an outer radius of 48.0 cm. The individual CsI crystal shapes are calculated from a class II geodesic breakdown of an icosahedron [10]. From the breakdown, nine different crystal shapes of varying frequency result (see Tab. 2.2).

Light output from the CsI crystals is collected and amplified with photomultiplier tubes of three inch and two inch diameter, for whole and half crystals, respectively. The photomultiplier tubes, Thorn EMI 9822QKB and 9923QKB, have quartz windows which are transparent to the UV light emitted by the CsI crystals. The tubes are coupled to the CsI crystals with optically transparent Dow Corning SYLGARD glue.

In order to identify charged particles, an approximately half-cylindrical thin plastic scintillator veto detector was placed in front of the 1997 CsI array (see

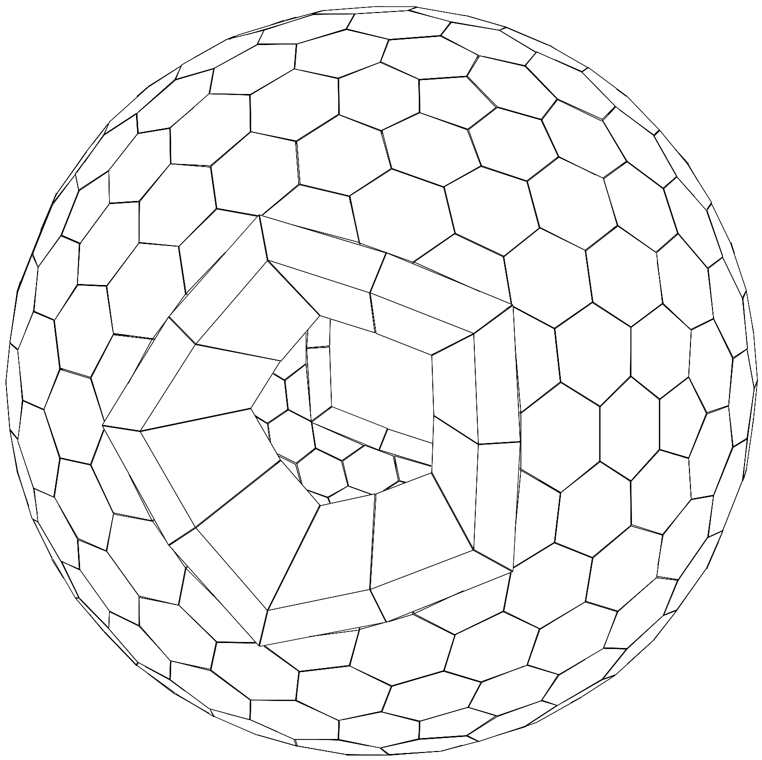

Figure 2.4: *The full PIBETA calorimeter of 240 pure CsI crystals.*

Crystal Volume Type	Name	Quantity
Pentagon	PENT	10
Hexagon A	HEXA	50
Hexagon B	HEXB	50
Hexagon C	HEXC	50
Hexagon D	HEXD	40
Half Hexagon D1	HEXD1	10
Half Hexagon D2	HEXD2	10
Veto 1	VETO1	10
Veto 2	VETO2	10

Table 2.2: *Nine CsI crystal volume types, and frequency of appearance in the completed PIBETA calorimeter.*

Fig. 2.3). The detector is comprised of eight thin Bicron BC-400 [3] plastic staves coupled to light guides and one-inch Burle S83062E [4] photomultiplier tubes. The staves have a thickness of 3.2 mm, a width of 4.0 cm, and a length of 300 mm.

2.2.2 NaI Detector

The NaI detector is an 8×8 array of optically isolated NaI(Tl) Polyscin^R scintillator bars. The dimensions of each bar are 63.5×63.5×406 mm^3. The array is encased inside an air-tight container. The lateral and rear walls of the container are comprised of 19 mm thick aluminum plates. Covering the front face of the array is a 0.5 mm thick steel sheet, layered with 20 mm of styrofoam and 2 mm of aluminum foil. Light output from the scintillator bars is read with 64 photomultiplier tubes (Philips PM2202) which are coupled to the NaI by 64 pyrex windows with 60 mm Plexiglas light guides. For charged particle identification, a 1 cm thick 54.6×54.6 plastic veto covers the front face of the array. A diagram of the detector is shown in Fig. 2.5. [1]

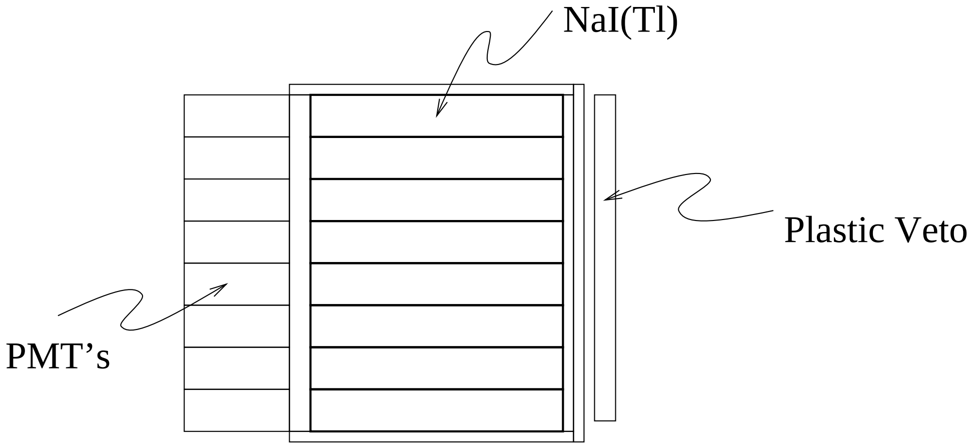

Figure 2.5: *Cross section of the array of 64 NaI(Tl) rectangular crystals.*

2.2.3 Liquid Hydrogen Target and Beam Counters

The geometric reconstruction of the liquid hydrogen target used in the measurements and Monte Carlo simulation is shown in Fig. 2.6. The target housing encloses a cylindrical volume of liquid hydrogen, of radius 2 cm and height 8 cm. The liquid hydrogen sits in a cylindrically shaped mylar container of wall thickness 150 μm.. The mylar container is surrounded by vacuum, which is enclosed by an aluminum cylindrical housing of inner radius 6.0 cm and wall thickness 1 mm. In the path of the incident beam is a 2 cm thick CH_2 degrader and 2.4 cm of ^{12}C degrader. This configuration of degraders produces the maximum stopping rate for pions in the liquid hydrogen target.

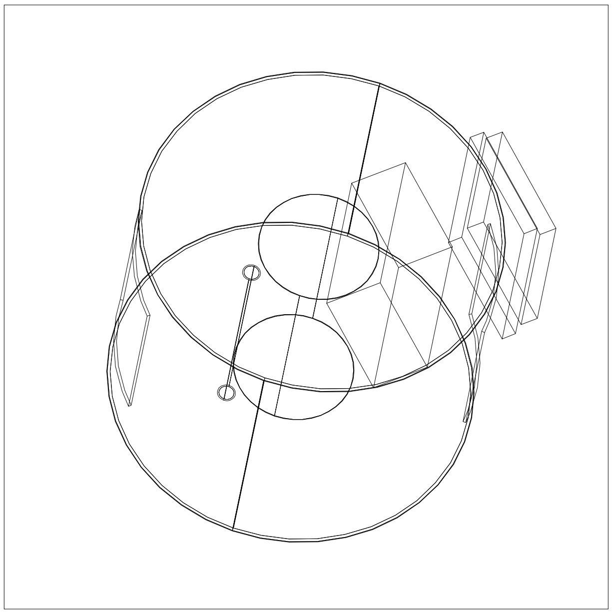

Figure 2.6: *Geometric reconstruction of the liquid hydrogen target used in the GEANT simulation of the Panofsky Ratio measurement. The liquid hydrogen is contained in the aluminum cylindrical object in the center. the rectangular objects are a series of carbon degraders which ensure that the 116 MeV/c π^- beam stops approximately in the center of the liquid hydrogen.*

The beam counter B0 is a thin plastic scintillator, placed immediately before the quadrupole magnet in the $\pi e1$ area. The beam counter B1 is a thin plastic "pill" shaped counter, placed between the quadrupole and the liquid hydrogen target. It is attached to the 2.4 cm of ^{12}C degrader described in the previous paragraph. Its active area is 1×1 cm, with a thickness of 0.2 cm.

2.2.4 $\pi e1$ Area Layout

Figure 2.7 shows the $\pi e1$ area layout for the Panofsky Ratio measurement. The 116 MeV/c negative pion beam comes from the right of the figure. The CsI and NaI detectors are placed 180° apart. The liquid hydrogen target is positioned in the beam, between the CsI and NaI arrays. The B0 and B1 beam counters are located immediately before the quadrupole and before the target, respectively.

With this experimental layout, it is possible to detect the nearly anti-collinear photons from the reaction $\pi{-}p \rightarrow \pi^0 n \rightarrow \gamma\gamma n$, as shown in Fig. 2.8. This detection requires a "two arm trigger" (See Sec. 2.2.5).

2.2.5 Electronics and Trigger Configurations

Components of Event Triggers

The CsI array is a subset of the final 240-element CsI spherical detector, as noted in Sec. 2.2.1. In order to define the trigger for the 240-element detector, the sphere has been divided into sixty overlapping clusters of CsI crystals. These clusters are then divided into ten superclusters. The size of the clusters and superclusters have been designed for optimum trigger efficiency, noise suppression, and event pile-up rejection in the detection of $\sim$70 MeV photons from the pion beta decay $\pi^- \rightarrow \pi^0 e^- \nu_e \rightarrow \gamma\gamma e^- \nu_e$ [10].

As a subset of the final spherical detector, the 44-element array contains

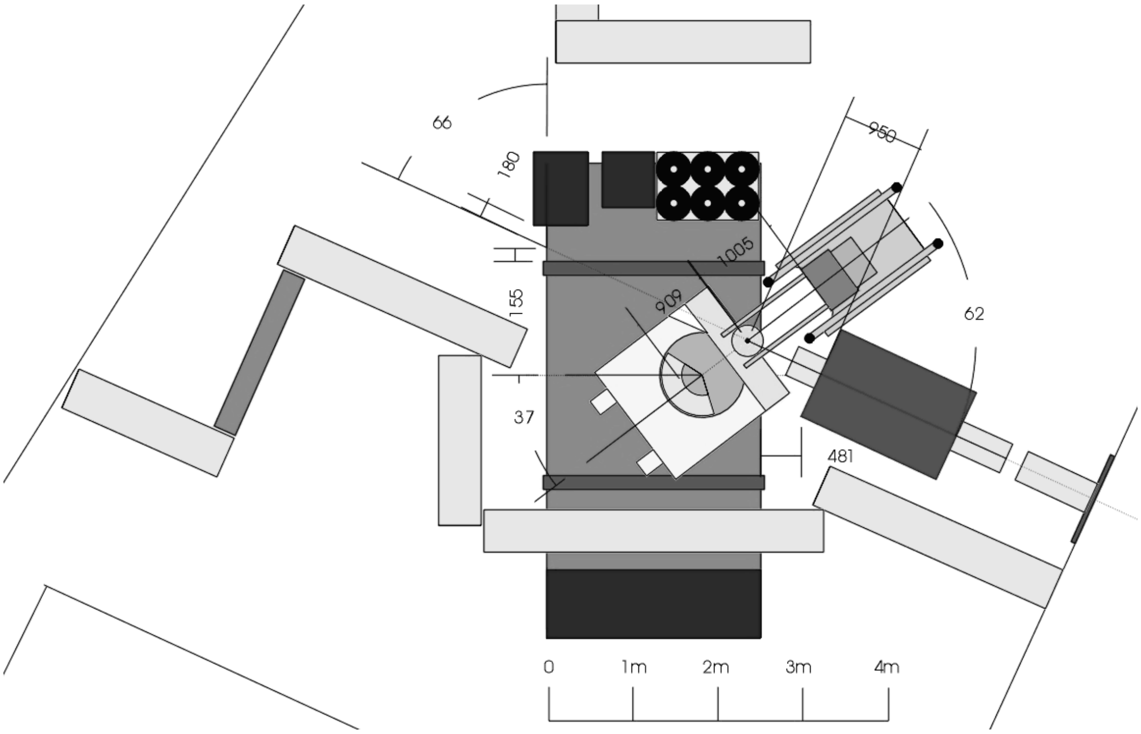

Figure 2.7: *Beam area (πe1) layout for Panofsky Ratio measurement. The 116 MeV/c π^- beam comes from the right of the figure, and stops in the liquid hydrogen target (shown as the small circular object in the figure). The CsI (larger circular object) and NaI arrays are shown to be positioned 180° apart, out of the path of the beam.*

representative crystals from ten of the clusters and three of the superclusters. The array is triggered when the sum of the analogue to digitial converter (ADC) values from one cluster exceeds a threshold of approximately 5 MeV. Specifically, the CsI trigger is equal to the logical OR of the three superclusters, which is equivalent to the logical OR of the ten clusters.

Like the CsI array, the NaI array is divided into subsections of detectors in order to define the trigger. In the 8×8 array, there are 36 'inner' crystals, and 28 'outer' crystals. The NaI array is triggered when the sum of the ADC values of

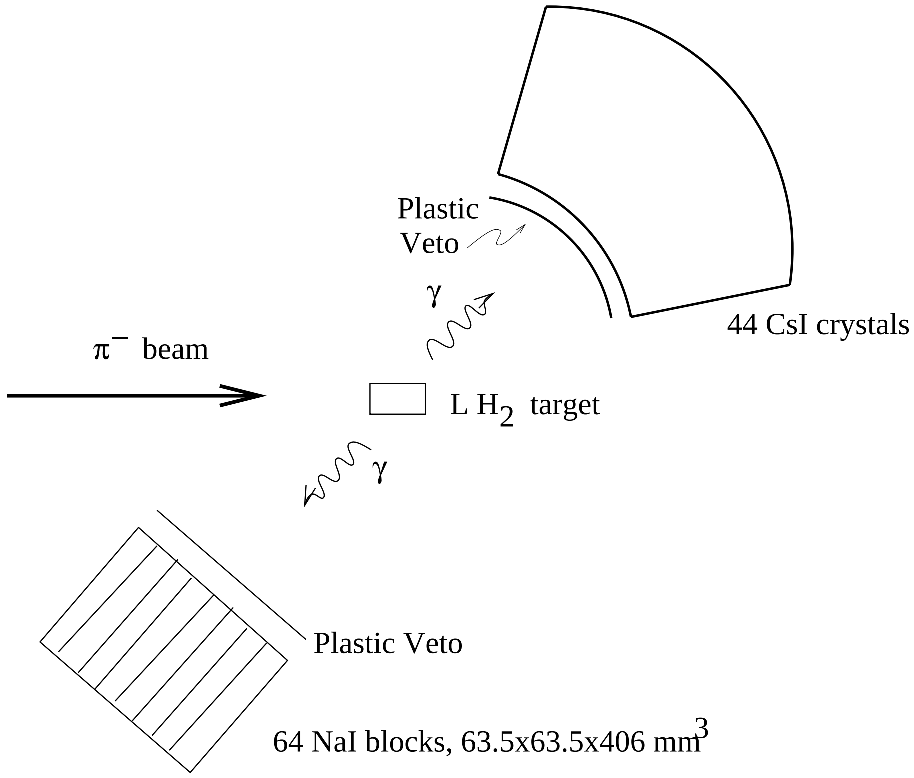

Figure 2.8: *Experimental layout for the Panofsky Ratio measurement, showing the detection of the two nearly anti-collinear photons from the reaction* $\pi - p \rightarrow \pi^0 n \rightarrow \gamma\gamma n$

the inner detectors exceeds a discrimator threshold equivalent to approximately 50 MeV, and the sum of the ADC values of the outer detectors is less than another threshold of approximately 15 MeV.

Another component to the event triggers is the coincidence between the beam counters B0 and B1. This coincidence is included in the event trigger to ensure the presence of a beam particle, and to select the correct type of beam particle. For the 116 MeV/c π^- beam, there is an electron contamination of a few percent. Due to the thickness of the B1 counter, one can discriminate between pions and electrons by their time of flight. Figure 2.9 shows a reconstruction of the coincident signals from B0 and B1, with the timing set to exclude electrons from the trigger.

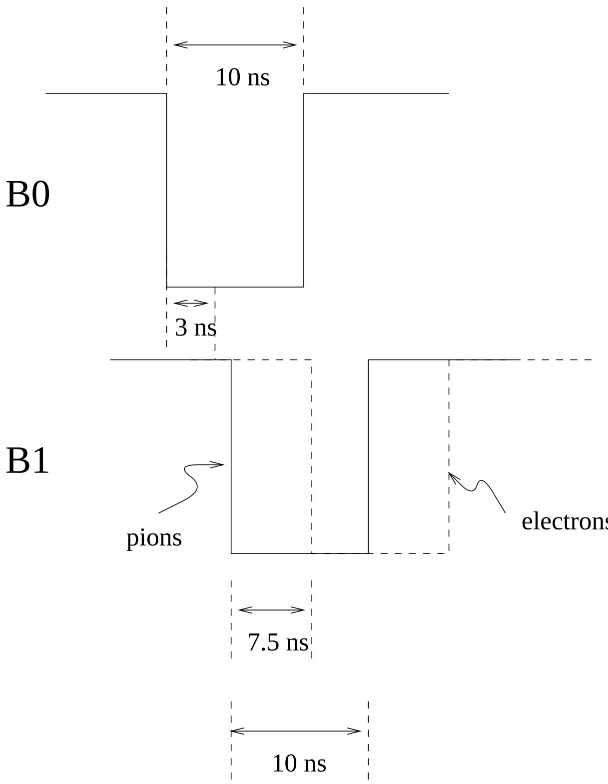

Figure 2.9: *Logic pulses forming the coincidence between beam counters 'B0' and 'B1'. The beam electrons are excluded from the coincidence by their time of flight.*

Event Triggers

With the area layout described in Sec. 2.2.4, it is possible to construct both a single arm and a two arm coincident trigger. The two arm trigger is used to detect the two approximately anticollinear photons emitted after the single charge exchange reaction $\pi^- p \rightarrow \pi^0 n$. It incorporates both the CsI and the NaI detectors, as well as the B0$\times$B1 coincidence. The trigger thresholds on the CsI and NaI arrays are set as described in Sec. 2.2.5. The timing of the two arm trigger, shown in Fig. 2.10, is such that the CsI array starts the time to digital converter (TDC).

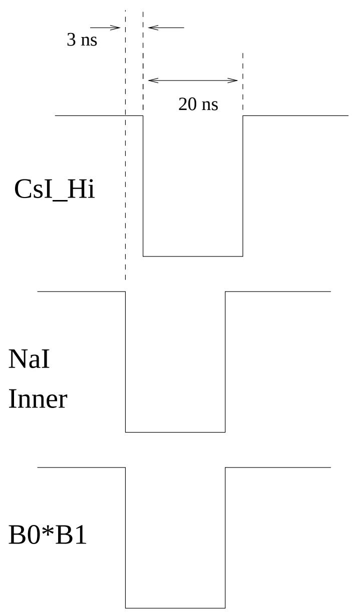

Figure 2.10: *Reconstruction of the signals for the two arm trigger configuration (CsI* NaI Inner* $\overline{\text{NaI Outer}}$ *(B0* B1).*

The two single arm triggers are comprised of the B0×B1 coincidence, and one of either the CsI or NaI detectors. In this way, it is possible to detect the photons from the single charge exchange reaction and the 129 MeV photon from the pion capture reaction $\pi^- p \rightarrow \gamma n$. Like the two arm trigger, the thresholds for triggering the arrays are set as noted in Sec. 2.2.5. The timing of each single arm trigger is determined appropriately by the CsI and NaI arrays. The CsI single arm trigger configuration is shown in Fig. 2.11.

The rates for the single arm and two arm triggers depend on that of their components. These trigger component rates for the 116 MeV/c beam runs are

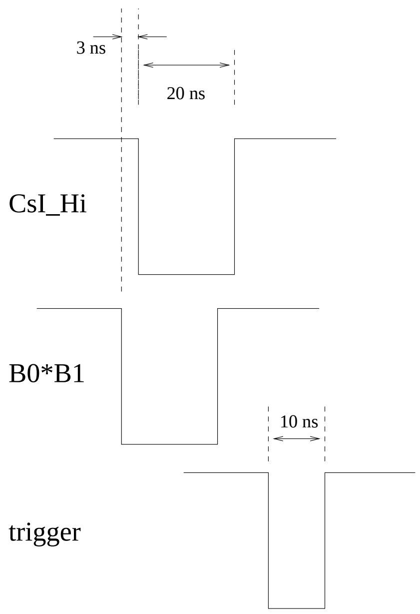

Figure 2.11: *Reconstruction of the signals for the CsI one arm trigger configuration (CsI∗ (B0∗ B1)).*

summarized in Table 2.3. The schematic of the electronics used in the 1997 beam time are shown in Figs. 2.12 through 2.20.

Counter	Rate (Pulses/sec.)
B0	370k
B1	130k
B0∗B1	91k
CsI Hi	6k
CsI Lo	9k
NaI Inner Hi	1k
NaI Inner Lo	2k
NaI Outer Hi	1k
NaI Outer Lo	3k

Table 2.3: *Experimental rates for 1997 Panofsky Ratio measurement.*

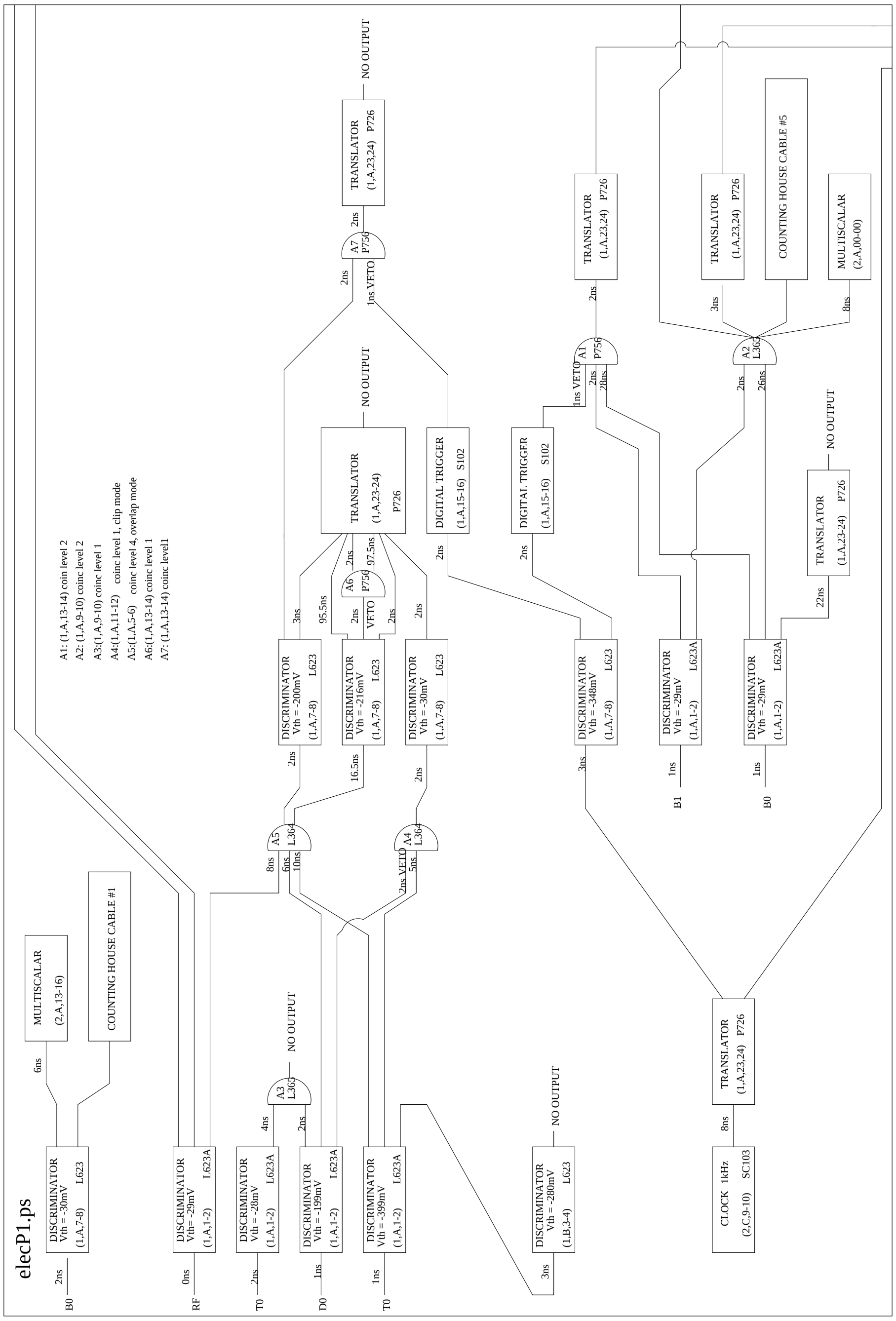

Figure 2.12: *First of eight panels showing a schematic of the electronics used during the 1997 beam time. Drawing courtesy of Michael Dugger, Arizona State University.*

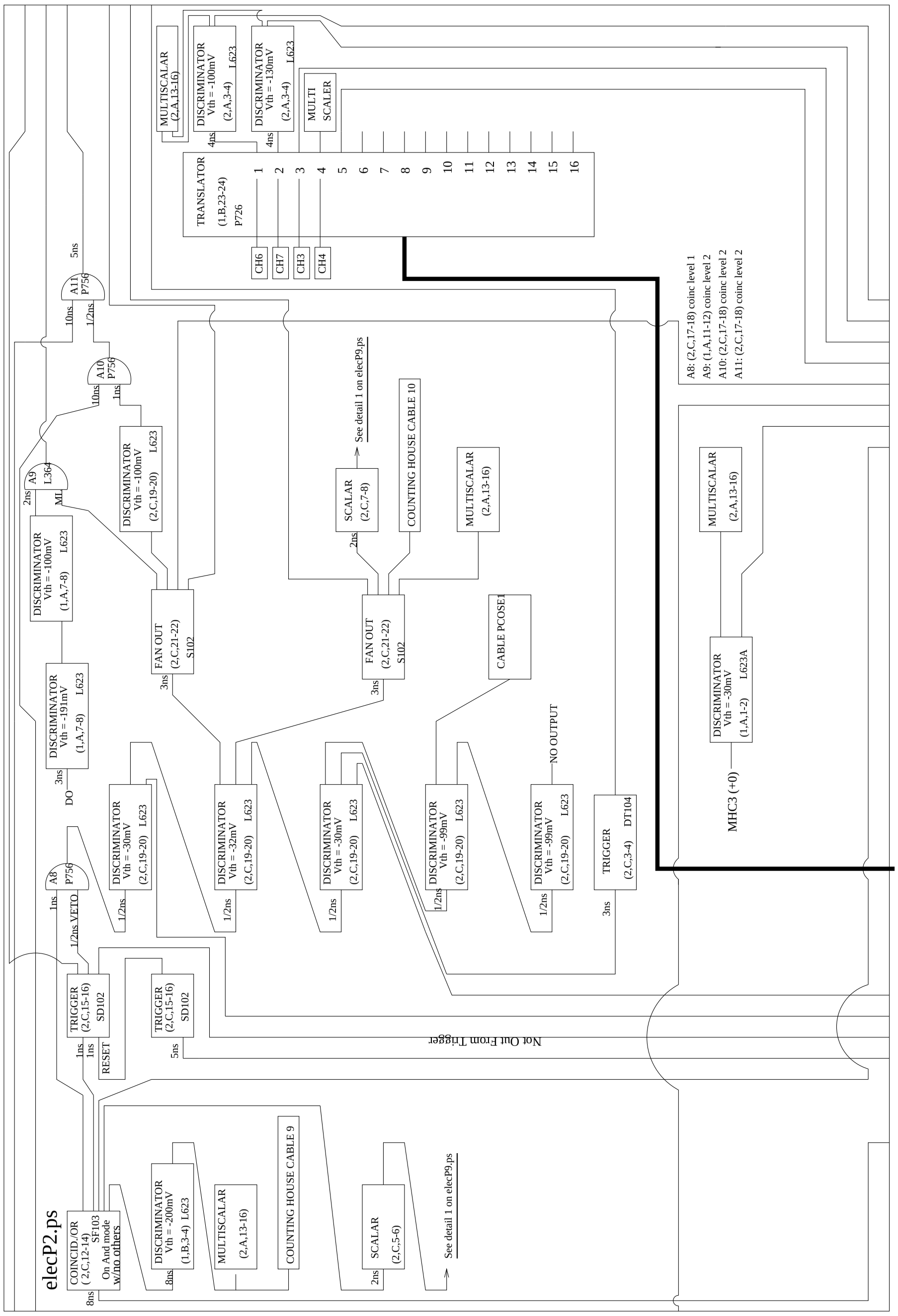

Figure 2.13: *Second of eight panels showing a schematic of the electronics used during the 1997 beam time. Drawing courtesy of Michael Dugger, Arizona State University.*

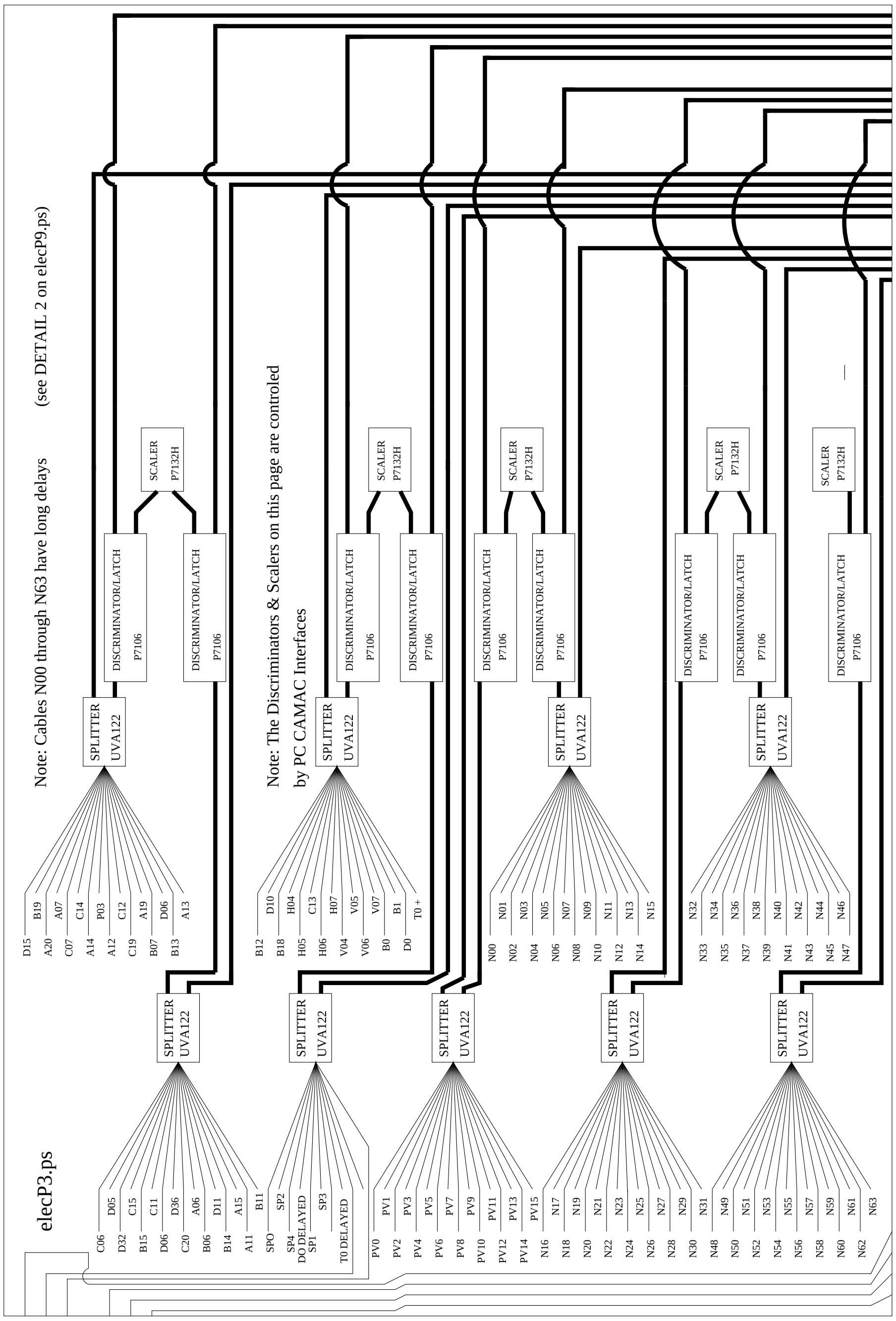

Figure 2.14: *Third of eight panels showing a schematic of the electronics used during the 1997 beam time. Drawing courtesy of Michael Dugger, Arizona State University.*

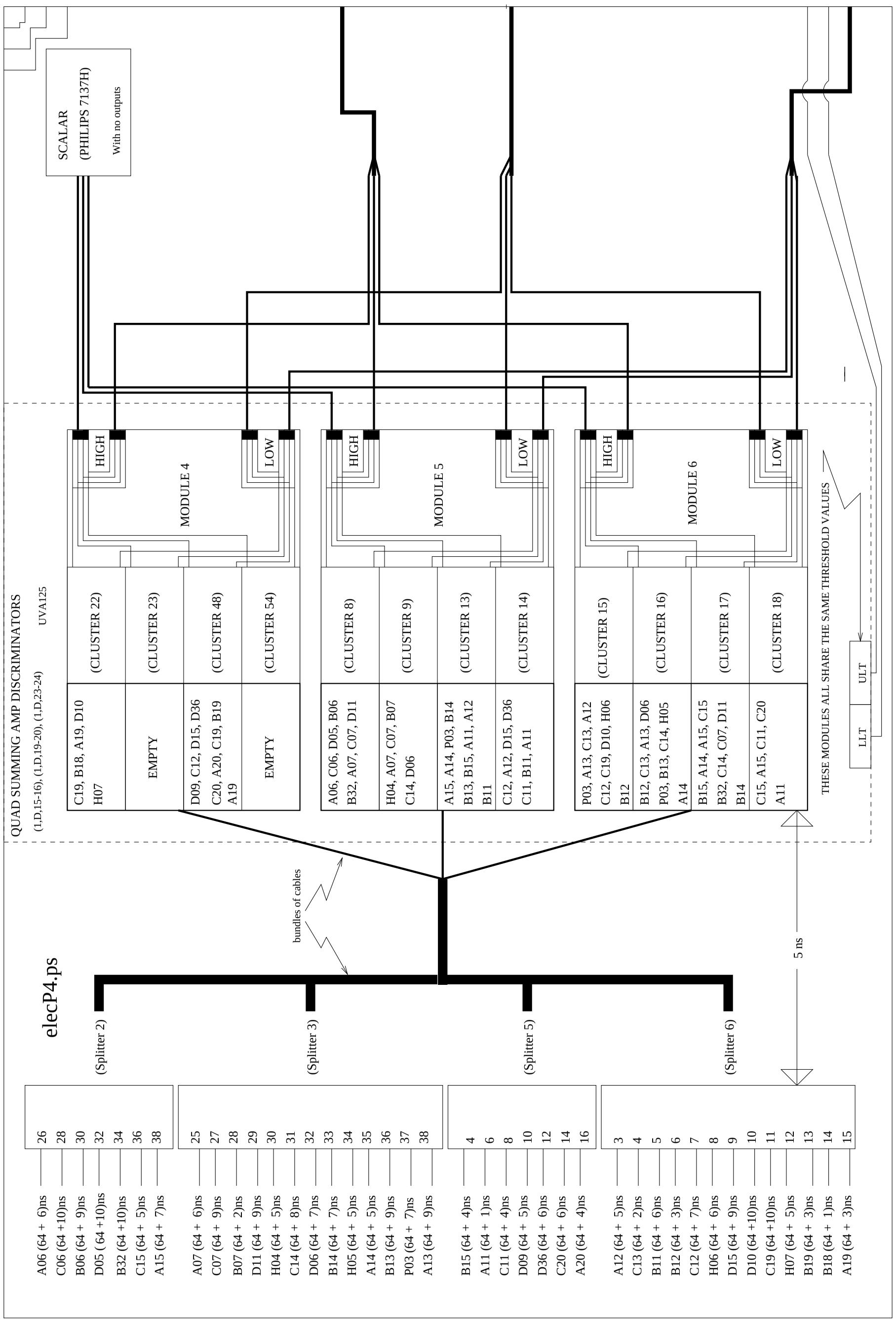

Figure 2.15: *Fourth of eight panels showing a schematic of the electronics used during the 1997 beam time. Drawing courtesy of Michael Dugger, Arizona State University.*

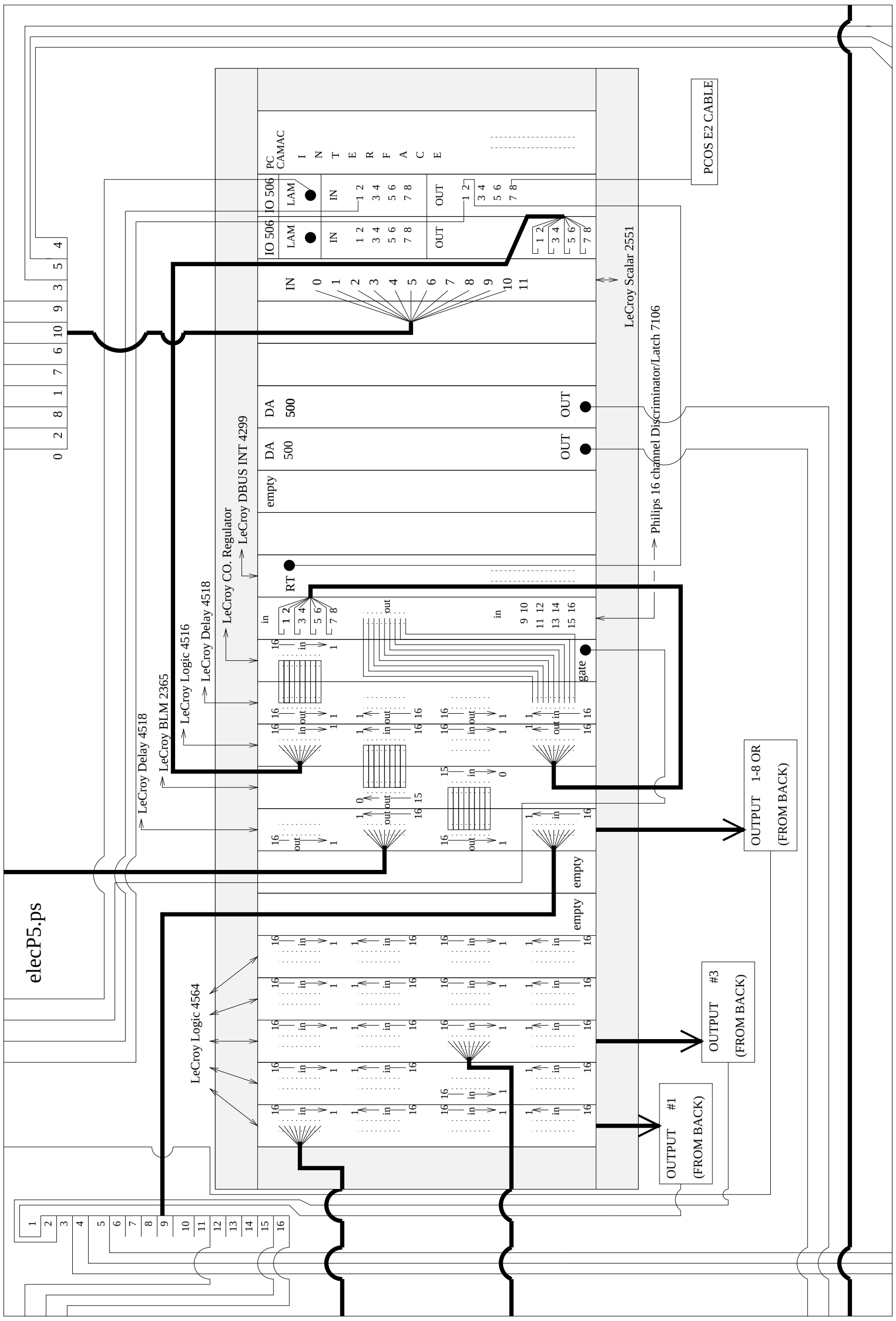

Figure 2.16: *Fifth of eight panels showing a schematic of the electronics used during the 1997 beam time. Drawing courtesy of Michael Dugger, Arizona State University.*

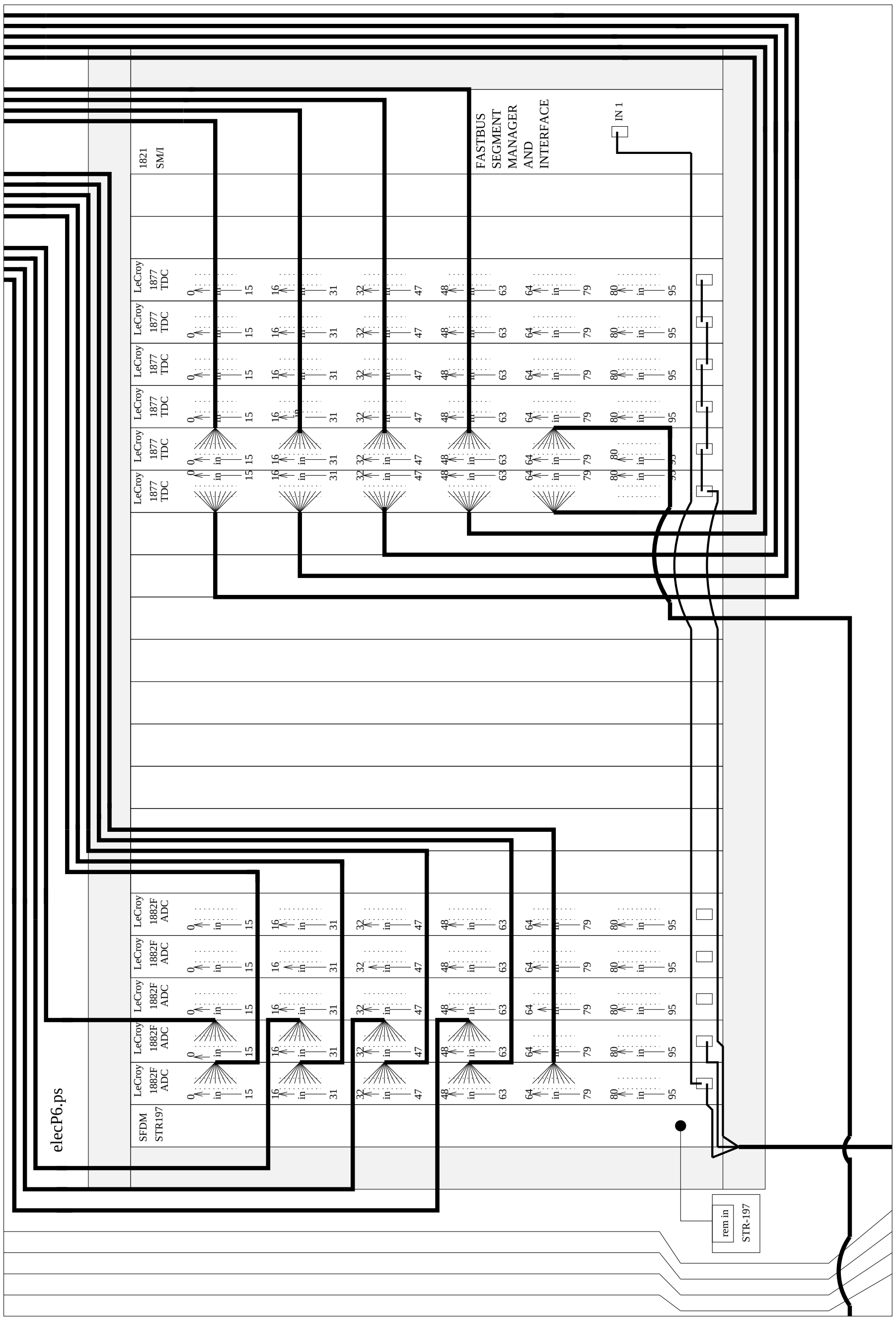

Figure 2.17: *Sixth of eight panels showing a schematic of the electronics used during the 1997 beam time. Drawing courtesy of Michael Dugger, Arizona State University.*

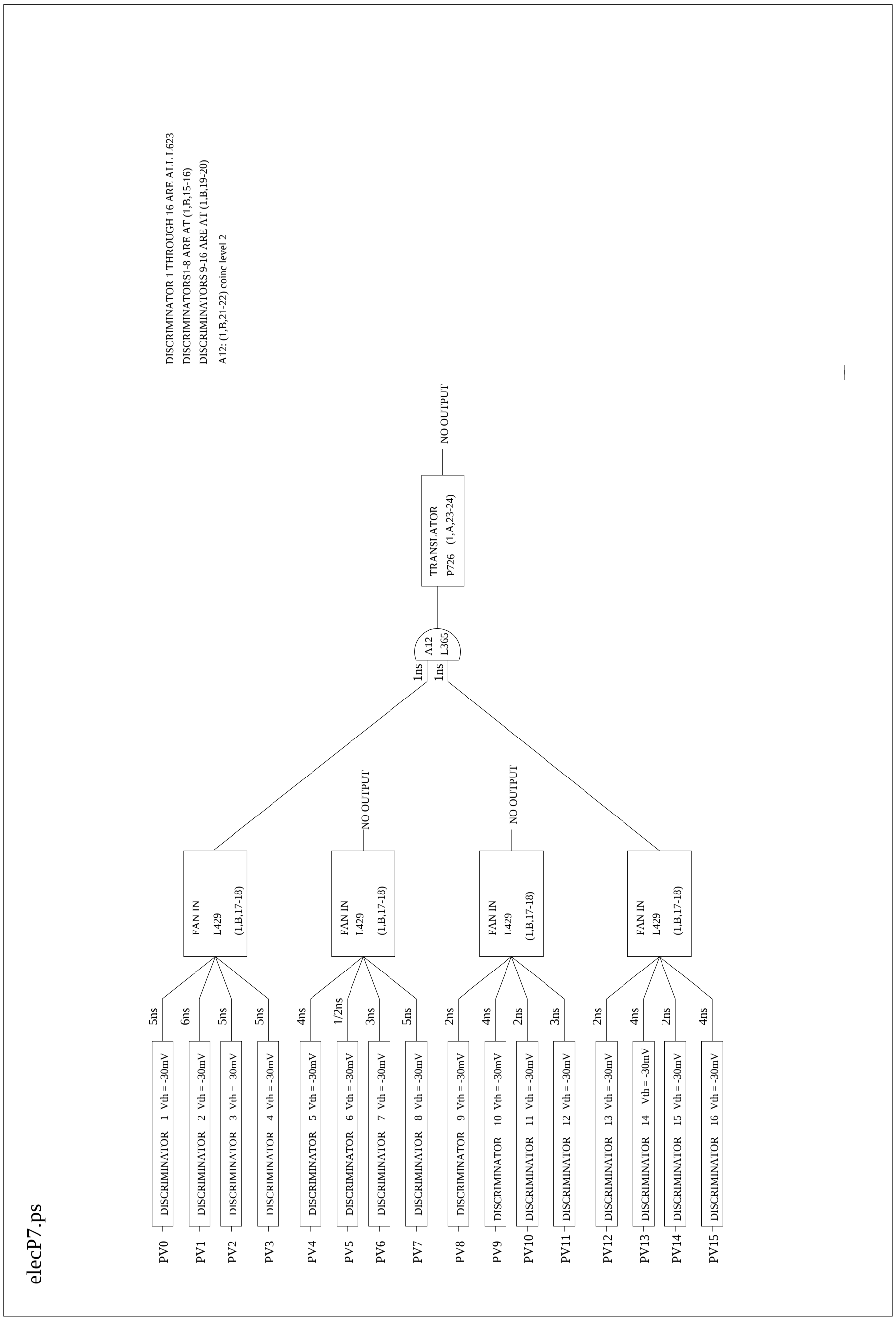

Figure 2.18: *Seventh of eight panels showing a schematic of the electronics used during the 1997 beam time. Drawing courtesy of Michael Dugger, Arizona State University.*

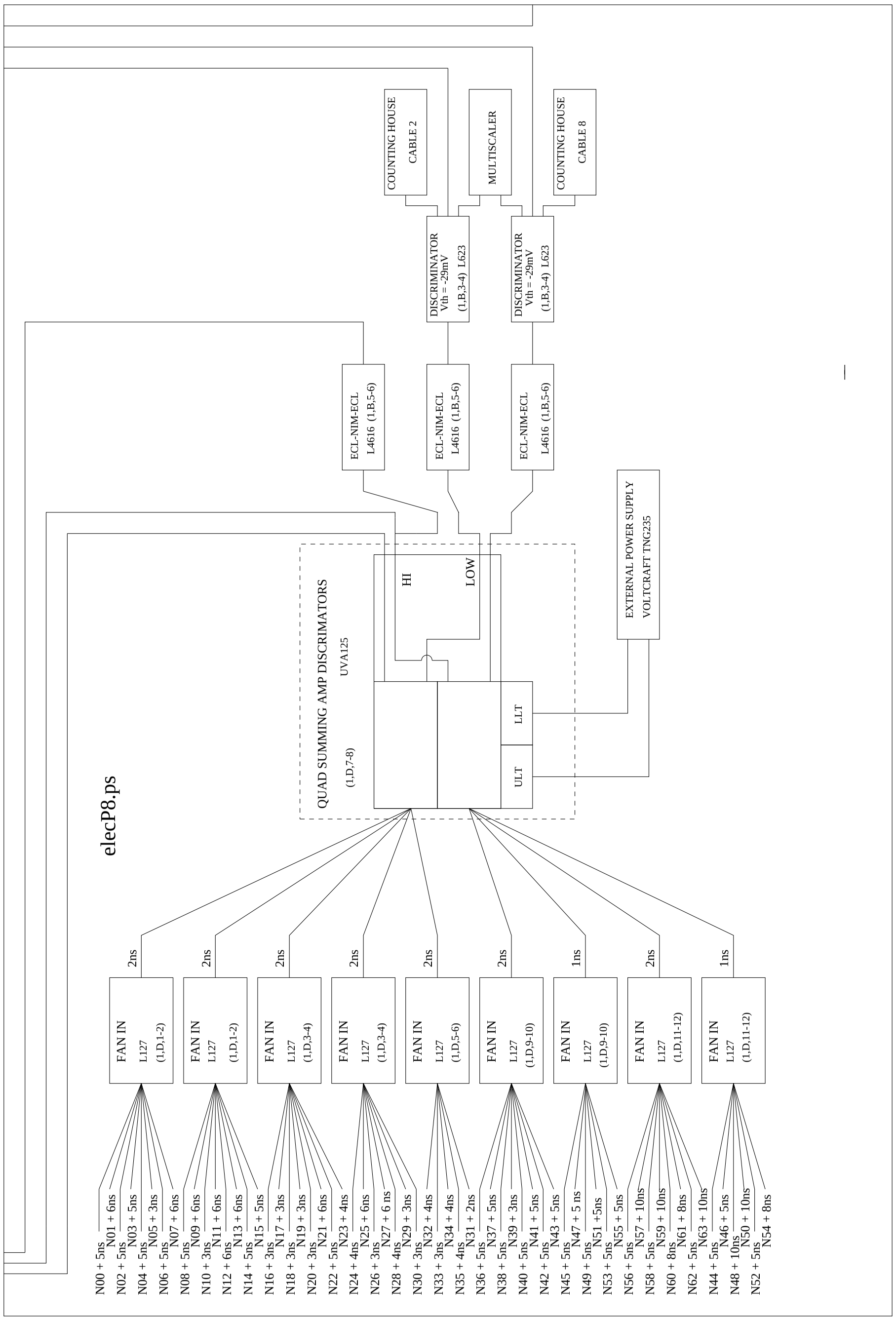

Figure 2.19: *Eighth of eight panels showing a schematic of the electronics used during the 1997 beam time. Drawing courtesy of Michael Dugger, Arizona State University.*

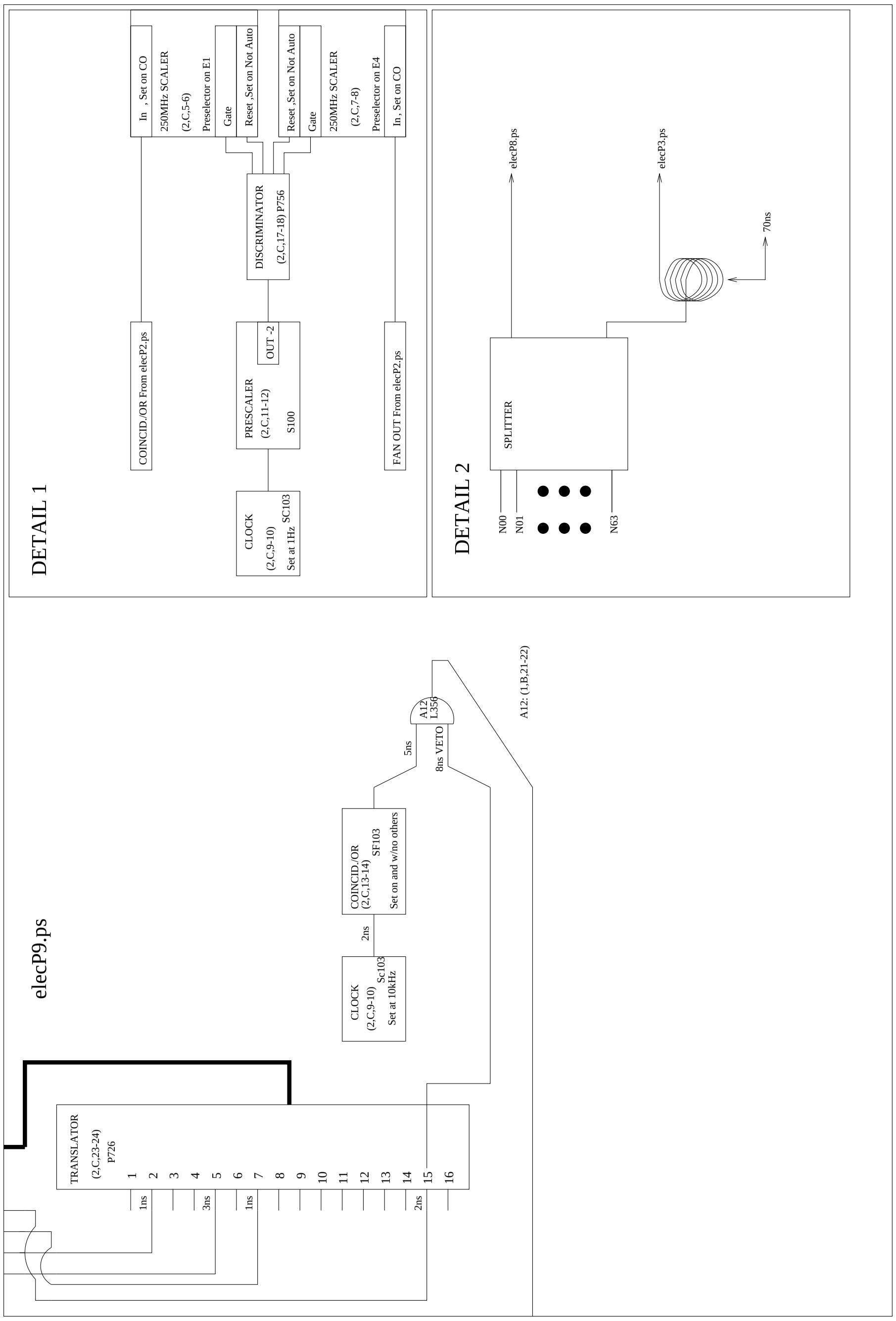

Figure 2.20: *One of eight panels showing a schematic of the electronics used during the 1997 beam time. Drawing courtesy of Michael Dugger, Arizona State University.*

Chapter 3

Tomography of Scintillators

3.1 Experimental Motivation for Scintillator Tomography

In order to calibrate the GEANT Monte Carlo simulation of the PIBETA detector response, it is necessary to account for the light output and position-dependent nonuniformities of each CsI crystal in the calorimeter. These quantities are entered into the simulation as a smearing factor and a spatially dependent weighting function in the crystal energy depositions. This chapter discusses the experimental techniques used to measure the light output and nonuniformities of the crystals, and the results of the measurements.

The light output, expressed in terms of number of photoelectrons per MeV deposited by minimum ionizing particles, can be measured by making use of the fact that the photoelectron statistics follow a Poisson distribution. Such a distribution is a limiting form of the binomial distribution

$$P(r) = \frac{N!}{r!(N-r)!} p^r (1-p)^{N-r}, \tag{3.1}$$

where p is the probability of success in a single trial, N is the number of trials, and $P(r)$ is the probability of r successes in N trials. The Poisson distribution arises in the limiting case where $p \to 0$ and $N \to \infty$, and takes the form

$$P(r) = \frac{\mu^r e^{-\mu}}{r!}, \tag{3.2}$$

where μ is the mean. This distribution lends itself to the description of photoelectron statistics because of the low probability for a charged particle to interact with one scattering center, combined with the presence of a large number of scattering centers inside one CsI crystal. In a Poisson distribution, the standard deviation σ is equal to the square root of its mean. Consquently, if one represents the light output in the CsI crystal as the number of photoelectrons per MeV n_p times the energy deposited by minimum ionizing particles E, then one can deduce

$$\sigma^2 = \frac{E}{n_p}. \tag{3.3}$$

Using this relation, one can extract the number of photoelectrons per MeV from the slope of a graph of sigma squared plotted against energy.

The light output nonuniformities are measured through the transmission tomography of the CsI crystals, using high energy cosmic muons as the probe. By determining the light output and muon trajectory length in the crystal, one can calculate the spatial light output nonuniformity, normalized over pathlength. This can be done in both the longitudinal and transverse directions. These directions correspond to the z and x axes, respectively, which are shown in Figure 3.1.

3.2 Experimental Apparatus

3.2.1 Cosmic Muon Tomography Detector

In order to measure the spatial light output nonuniformity, Thorn EMI 9822QKB photomultipliers are coupled to the CsI crystals with optically trans-

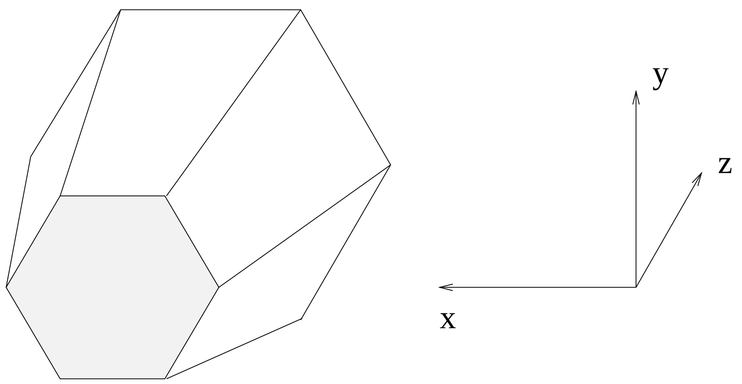

Figure 3.1: *Geometry and coordinate system for a hexagonal CsI crystal. The Z axis represents the longitudinal direction, and the X axis represents the transverse direction.*

parent Dow Corning SYLGARD glue, and are placed into a designated light-tight aluminum 'Cosmic Muon Tomography' (CMT) box. Two pairs of flat, multi wire drift chambers (MWDC) are mounted above the box, and one pair is fixed below it. By having a total of three wire chamber pairs, the muon trajectories can be both reconstructed and checked for scattering. The wire chambers have an effective coverage of about 60×60 cm. Under the box and chambers there are two 1 cm thick plastic scintillators ('SB1' and 'SB2'), and just above the scintillators there is a 5 cm thick layer of lead bricks. Figure 3.2 shows a diagram of the apparatus. The lead bricks serve to help stop cosmic muons with kinetic energies lower than ~160 MeV, as shown with the Monte Carlo simulation. This ensures that the accepted muons are minimum ionizing particles that travel straight through the crystals and the entire apparatus.

Six crystals can be positioned in the box at one time, and are connected to signal and high voltage cables which feed through from the electronics outside the box. The trigger for an acceptable cosmic muon event consists of at least one crystal being hit, in coincidence with a signal from both scintillators. The

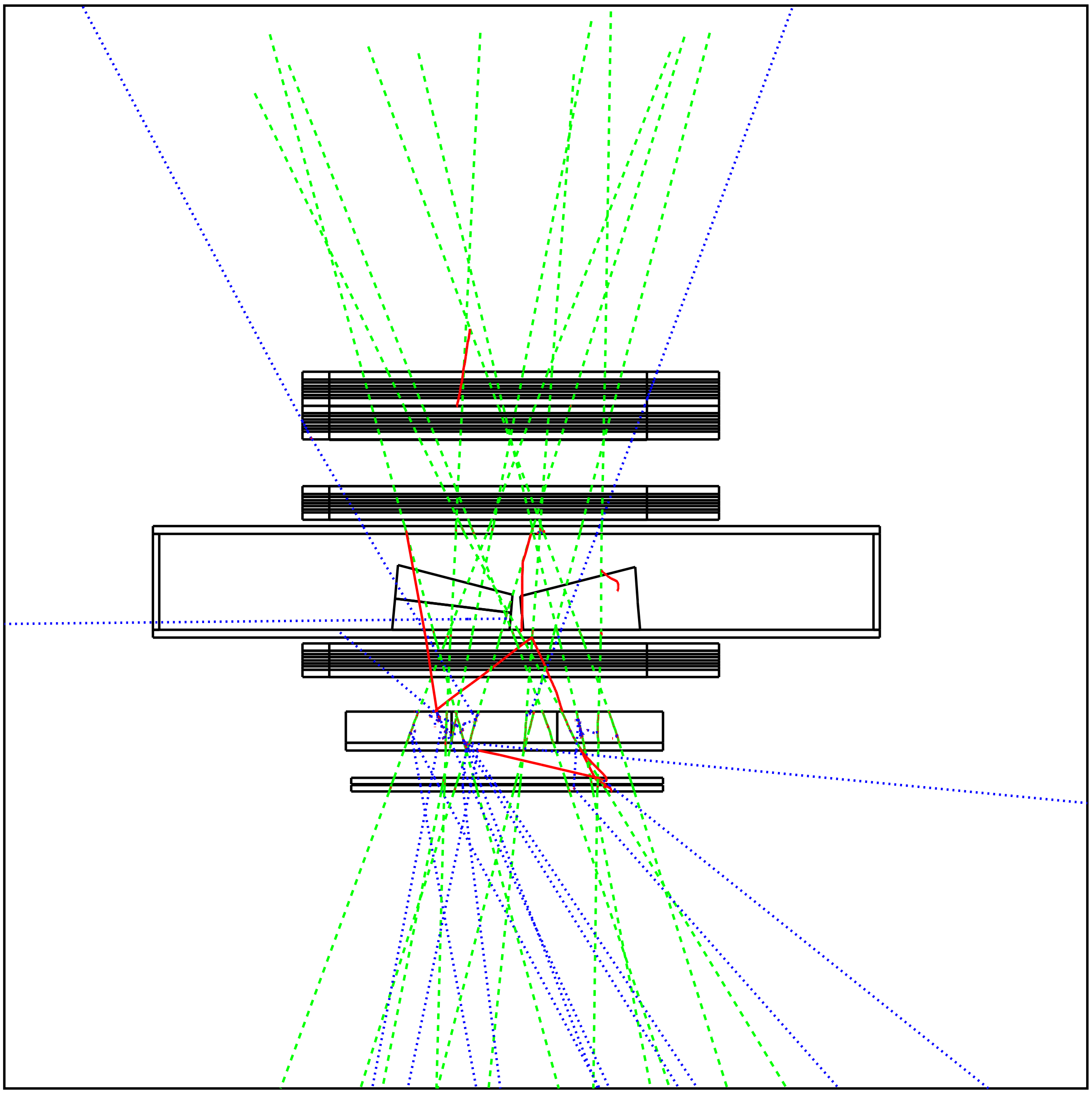

Figure 3.2: *Monte Carlo simulation of penetrating cosmic muons interacting with the CMT experimental apparatus. Two of a possible six CsI crystals positioned in the apparatus are shown. The lower three black rectangular objects are multi wire drift chambers (MWDC); two are above the box and one is below the box. Also shown is a layer of 5 cm thick lead brick below the lowest MWDC, and two flat plastic scintillators at the bottom.*

trigger rate is approximately 1 Hz, which means that each crystal requires one week to be reliably tomographed. Although the wire chamber information is not used to define the trigger, it is used offline to reconstruct the trajectories of the accepted muons and to reject particles with scattered trajectories. The electronics logic is shown in figure 3.3

The number of photoelectrons per MeV is measured by attaching a light emitting diode (LED) to the CsI crystal. It is then clocked to flash at 10 kHz. The trigger for an 'LED' event is simply a signal from at least one of the six crystals in the box. The light intensity from the LED is varied to produce peaks equivalent to $\sim$10 MeV to $\sim$100 MeV in five or six steps, which produces five or six discrete peaks in the detector's recorded energy spectrum. By plotting the square of the standard deviations against the means of these peaks, one can extract the number of photoelectrons per MeV from the slope, as shown in Fig. 3.4.

3.2.2 Radioactive Source Tomography Apparatus: RASTA

Slow counting rates with cosmic muons, coupled with the requirement of high statistics for accurate tomography analysis, result in CMT run durations that are impractical for treating all 240 CsI detector elements. Therefore, an alternative method has been developed to tomograph the CsI crystals. The Radioactive Source Tomography Apparatus (RASTA) utilizes a ^{137}Cs source instead of cosmic muons as the tomography probe. The source, which emits 0.66 MeV photons, is scanned over the length of the crystal in 2 cm steps. A diagram of the RASTA set-up is shown in Figure 3.5. The trigger rate for this operation is roughly 3 kHz, which is much higher than the 1 Hz rate for the CMT apparatus. Consequently, each crystal can be tomographed by RASTA in about one hour, as compared to one week in the CMT apparatus.

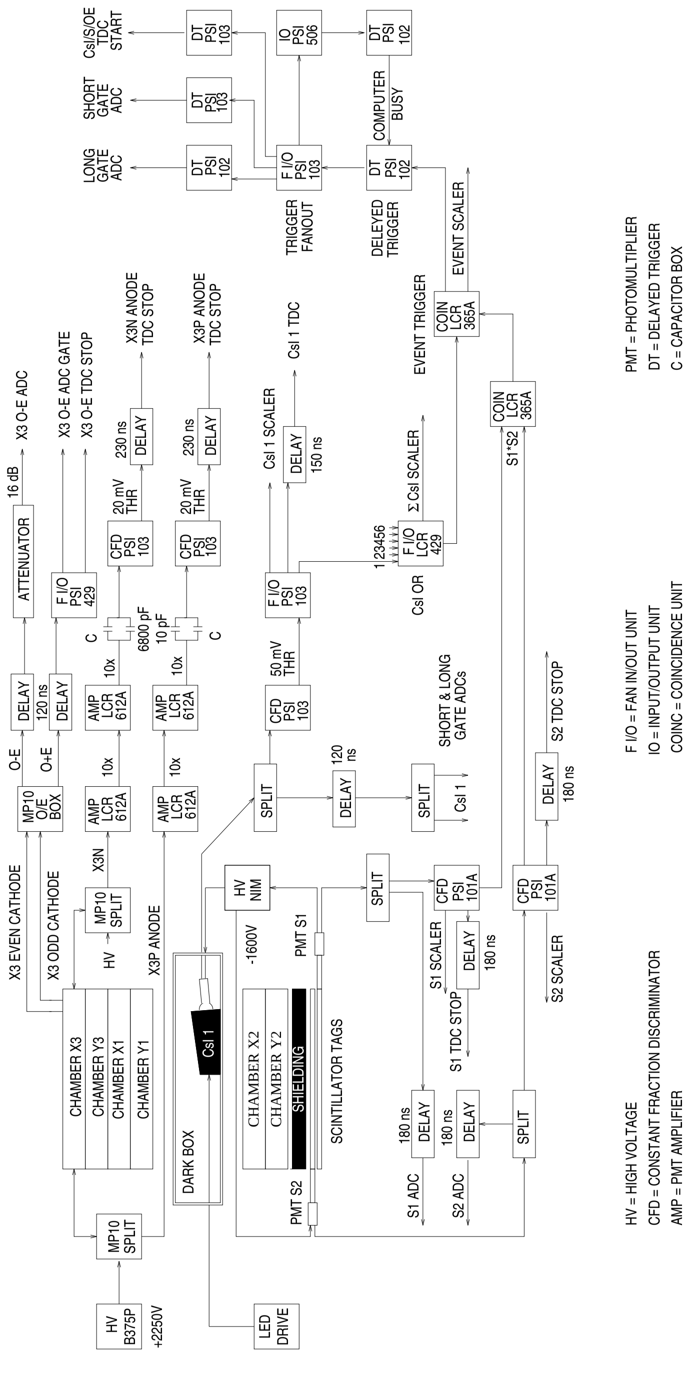

Figure 3.3: *Schematic diagram of the electronics logic for the tomography apparatus. The trigger for a cosmic muon event is a signal from at least one CsI detector, in coincidence with the two scintillators SB1 and SB2.*

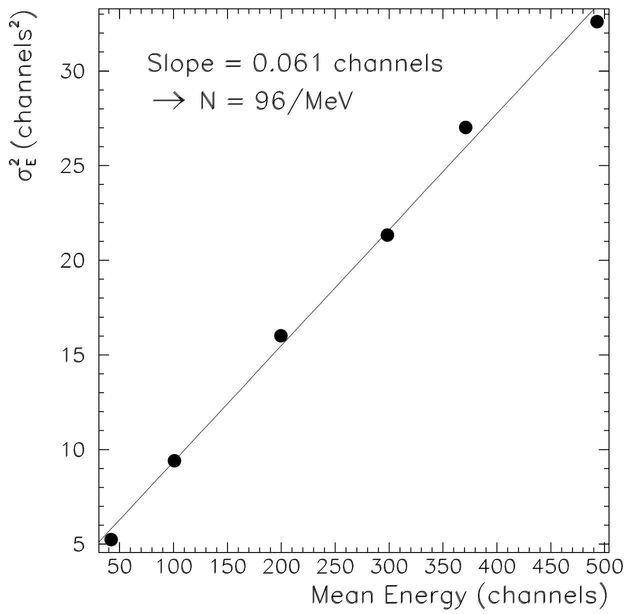

Figure 3.4: *Graph of σ^2 against Energy for pentagonal crystal "S003". From the inverse of the slope of the graph, one finds that the number of photoelectrons per MeV for this crystal is 96/MeV.*

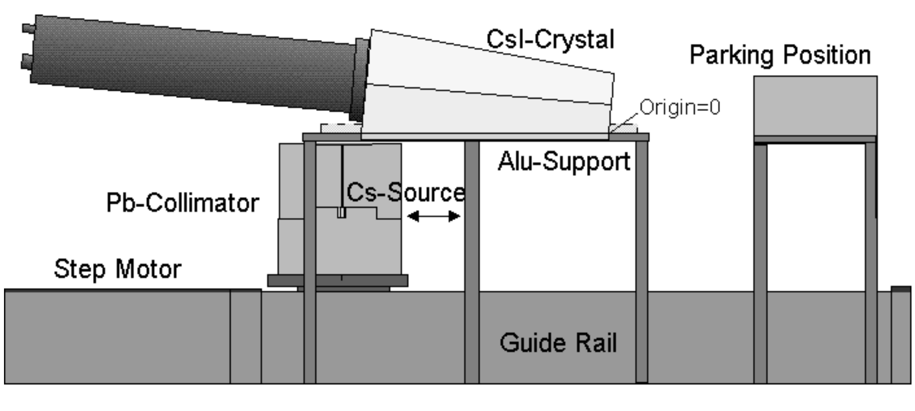

Figure 3.5: *Radioactive Source Tomography Apparatus (RASTA). A ^{137}Cs source, collimated by a 6 mm diameter hole bored through a 5 cm thick lead brick, is scanned along the surface of the crystal by a step motor, in 2 cm increments.*

Like the CMT apparatus, the RASTA apparatus is a dark box with feed-through connectors for the signal and high voltage cables from the electronics outside the box. The RASTA apparatus can accomodate one CsI detector at a time. The trigger for one event consists of a signal from the CsI detector. The electronics logic is shown in Figure 3.6. The number of photoelectrons per MeV is measured with the RASTA apparatus using the same technique as in the CMT box, which is described in Section 3.2.1.

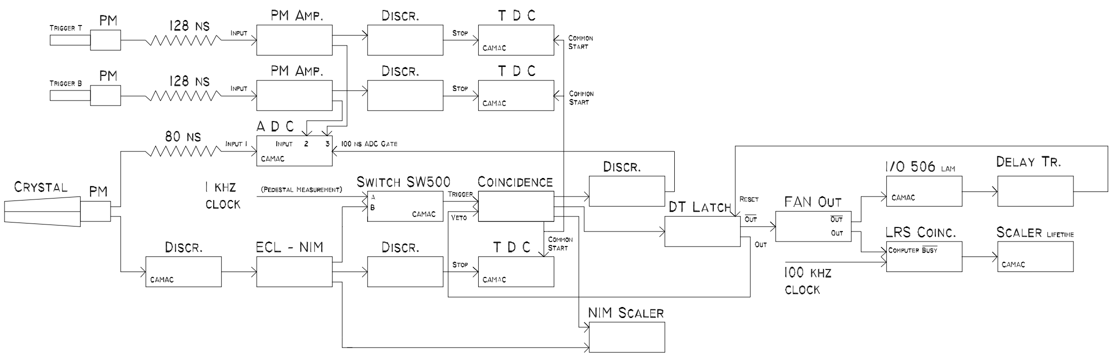

Figure 3.6: *Schematic of the electronics the RASTA apparatus. The trigger for one event consists of a signal from the CsI detector.*

3.3 Results and Discussion

3.3.1 Cosmic Muon Tomography Results

Crystal Light Collection Nonuniformities

The first step in the data reduction for light nonuniformity calculations with the CMT device, after pedestal subtraction and gain matching, is to describe the geometry of the scintillator in the reference frame of the dark box. This information is needed in order to translate the wire chamber trajectories into particle entry and exit points in the scintillator volume, which are then used to calculate the muon pathlength. The CMT coordinate system is shown in Figure 3.7, with six CsI crystals and photomultiplier tubes appropriately positioned. From the figure, one can see that there are actually two coordinate systems; one for the three crystals on the left, and one for the three crystals on the right. In this way, the positive z-axis always points from the narrow front face of the crystal, to the wide back face. As a check in the geometry, one can plot the reconstructed muon entry and exit points in the three orthogonal planes to see that they form the outline of the CsI crystal volume. Figure 3.8 shows these plots for one hexagonal CsI crystal.

Finally, using the calculated pathlength and the ADC value for each event, one can determine the average light output per unit pathlength integrated over the trajectory defined by the entry and exit points.

The light output per unit pathlength can be plotted along the axes of the crystal. Figure 3.9 shows the light output per unit pathlength ('s/d') along the longitudinal (z) and transverse (x) axes for two CsI crystals. To represent the longitudinal light nonuniformity of the crystal, the graph has been fit with straight lines in three separate regions: the front 10 cm of the crystal, the middle 8 cm, and the back 4 cm. These boundaries have been chosen by inspection of

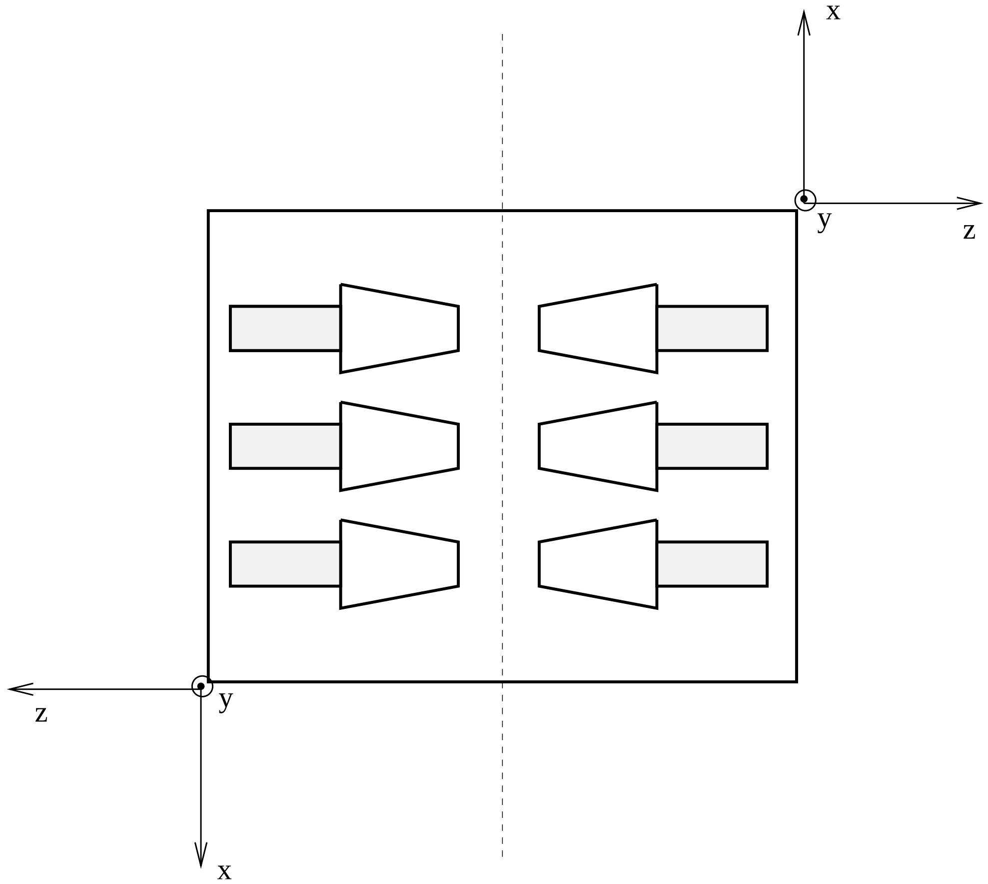

Figure 3.7: *Coordinate system of CMT apparatus with six CsI crystals and photomultiplier tubes in place. The two coordinate systems shown correspond to the left three crystal positions and the right three crystal positions, respectively.*

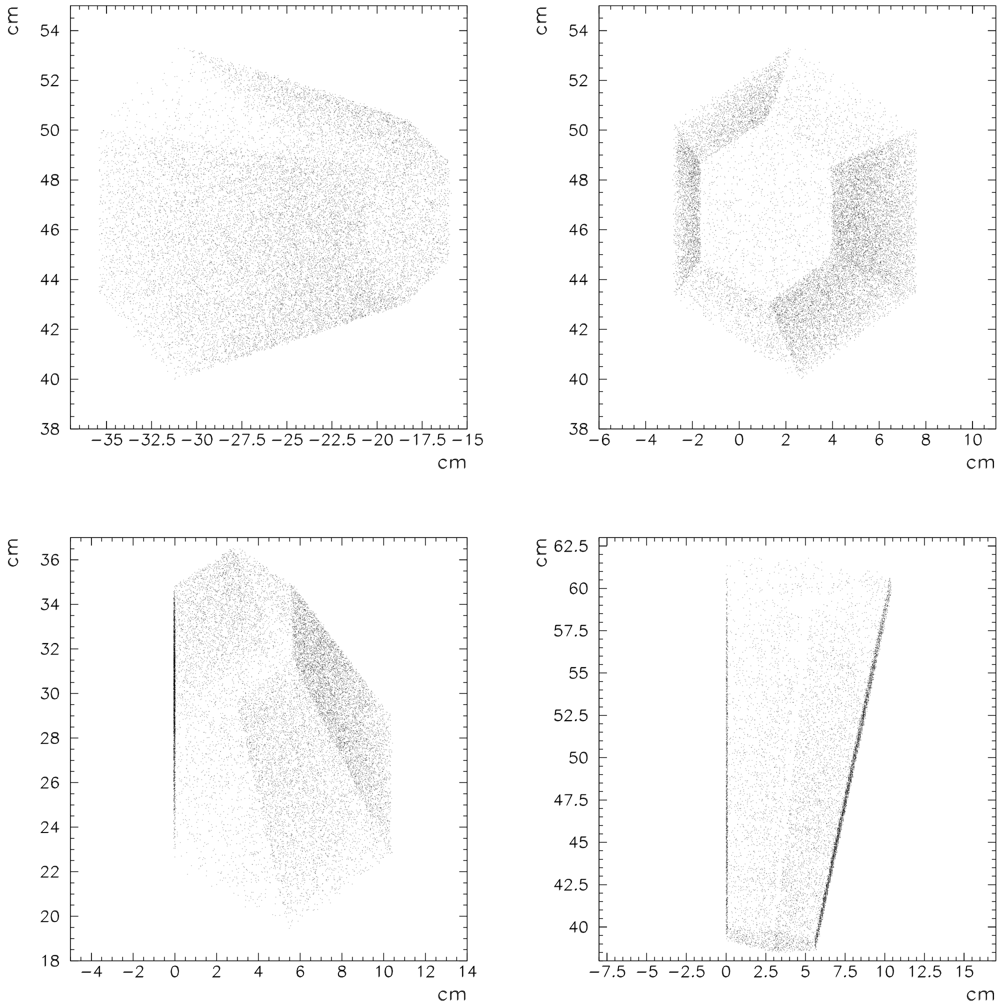

Figure 3.8: *Reconstructed entry and exit points of cosmic muons in one CsI crystal.*

apparent discontinuities in the nonuniformity spectrum. The slopes of the fitted lines, divided by the average value of the light output per pathlength in the region of interest, represent the spatial nonuniformities of the light output for the crystal in percent per centimeter.

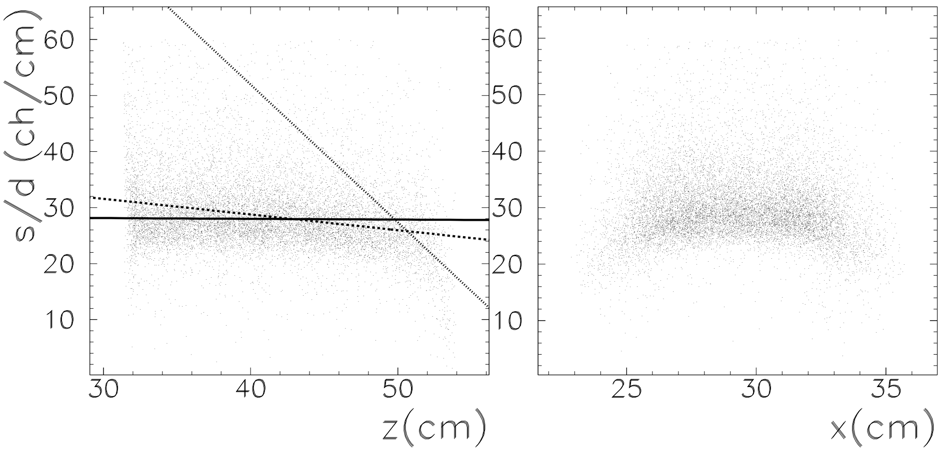

Figure 3.9: *Light output per unit pathlength as a function of the longitudinal (left panel) and transverse (right panel) average crystal coordinate, for one hexagonal CsI crystal. The longitudinal nonuniformity is quantified with the slopes of three straight lines (shown), which are fit to the plot in three predetermined regions.*

The fitting algorithm used is a "maximum likelihood" method [16]. A chi-squared fitting routine was also tried, but was not successful due to the influence of a small number of points which were much higher than the majority. The maximum likelihood method minimizes the sum of the absolute deviations

$$\sum_{i=1}^{N} \left| y_i - y(x_i; a_1 ... a_M) \right|, \tag{3.4}$$

where $a_1 ... a_M$ are the parameters which describe the fit to the data set y_i. In comparison, the chi-square method minimizes the quantity

$$\chi^2 = \sum_{i=1}^{N} \left(\frac{y_i - y(x_i; a_1 ... a_M)}{\sigma_i} \right)^2, \tag{3.5}$$

where σ_i is the standard deviation of each measurement y_i. The maximum likelihood method is useful in cases where a Gaussian model for measurement errors is a bad approximation. It assumes that the measurement error is the same for all data points, thereby minimizing the influence of data points which deviate greatly from the majority of the measurements.

To visualize the light output distribution qualitatively, one can make a two dimensional histogram of the light output per pathlength as a function of the axial and transverse coordinates. Figure 3.10 shows such a histogram for one hexagonal crystal.

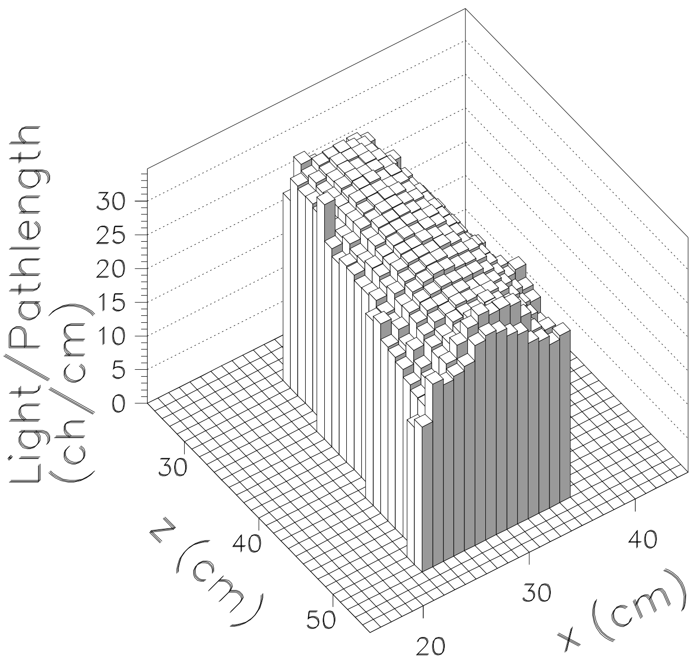

Figure 3.10: *Two-dimensional light output per pathlength of one hexagonal CsI crystal, projected onto the horizontal plane.*

Results of Light Output Measurements

The analysis of the LED spectra also involves several steps. First, an energy calibration is done based on the expected position of the muon peak. Next, the five or six discrete energy peaks are fit with a Gaussian function to determine their means and standard deviations. Finally, the slope of the graph of sigma squared against energy is measured and the number of photoelectrons per MeV (n_p) is extracted, as described in Section 3.1.

3.3.2 RASTA Results

The light output nonuniformity results from the RASTA apparatus are reasonably consistent with those from the CMT box. Discrepancies arise from the differing detection mechanisms in each apparatus, and from the varying processes by which 0.66 MeV photons (RASTA) and $\sim$1 GeV muons interact with the CsI material. These differences are manifested as follows:

- The 0.66 MeV photons from the ^{137}Cs source are not minimum ionizing particles in the CsI. Their energy is also below the 1.022 MeV e^+e^- pair production threshold. Therefore, they interact with the CsI primarily through Compton scattering and the photoelectric effect. Because materials with higher atomic number Z are the most favored for photoelectric absorption in the $\sim$1 MeV range, the CsI is particularly responsive to the 0.66 MeV photons in this way.

  Unlike the 0.66 MeV photons, the $\sim$1 GeV cosmic muons are minimum ionizing particles, and interact by ionizing the molecules in the CsI. In general, they exhibit very little brehmstrahlung due to their energy and relatively large mass. Any muons which do scatter and emit brehmstrahlung are identified as such, and are ignored to preserve accurate tracking information.

- There is a difference in the distribution of energy deposition between the RASTA and CMT apparatus. The cosmic muons transfer their energy uniformly along their tracks in the CsI material. On the other hand, while the 0.66 MeV photons from the $^{1}37$Cs source can probe the entire volume of the crystal, the Monte Carlo simulation shows that they deposit six times as much energy near the crystal surface as they do at the central (z) axis. [8] This feature leads to the extraction of different optical nonuniformity coefficients, because of inherent averaging over varying scintillation volumes in the two methods.

- Finally, the position resolution of each event in the RASTA box is determined by the position of the collimated ^{137}Cs source, and not through tracking with wire chamber data as in the CMT apparatus.

Figure 3.11 shows the light output collection nonuniformity slopes for hexagonal crystal S034 from both the RASTA and CMT apparatus. There is reasonably good agreement in the region $0 < z < 10$ cm. The tomography results for both methods are quantified for crystal S034 in Table 3.1.

Method	Slope 0:10 cm	Slope 10:18 cm	Slope 18:22 cm
CMT	0.7±0.1(%/cm)	-1.0±0.3(%/cm)	-11.261±4(%/cm)
RASTA	0.77 (%/cm)	-1.88 (%/cm)	-5.8 (%/cm)

Table 3.1: *Comparison of light output collection nonuniformities for crystal S034, measured with CMT and RASTA.*

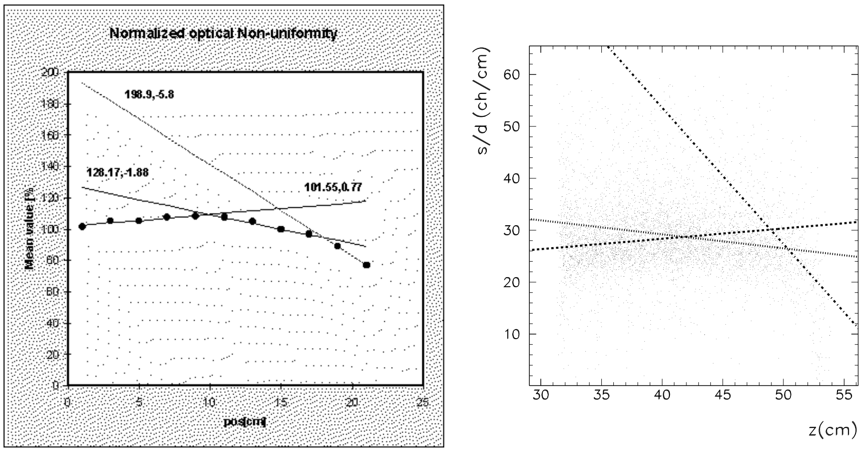

Figure 3.11: *Comparison of tomography results for hexagonal crystal s034, using the RASTA apparatus (left panel) and the CMT apparatus (right panel). The three fitted lines in each case depict the nonuniformity results for the regions 0:10 cm, 10:18 cm, and 18:22 cm.*

3.4 Tomography of PIBETA Plastic Veto Staves

The optical properties of six of the Bicron BC-400 thin plastic staves which make up the twenty-element PIBETA cylindrical veto hodoscope have been characterized using the CMT apparatus. These measurements were difficult to make, due to several factors. First, two of the six multi wire drift chambers in the CMT apparatus experienced an electrical short somewhere inside the enclosed gas chambers. Thus, because extensive repairs to the wire chambers were needed, the measurements were halted with the limited number of cosmic muon events which had been collected prior to this. Secondly, the plastic staves are 60 cm long, which limits the uniformity of the cosmic muon event acceptance. Specifically, the active area of the CMT apparatus is $60{\times}60$ cm^2, but is not uniform over this region. As a result, the ends of the plastic staves appear to be less illuminated than the middle, which affects the extraction of quantities such as attenuation length and index of refraction. The geometry specifications of one plastic veto stave are depicted in Figure 3.12.

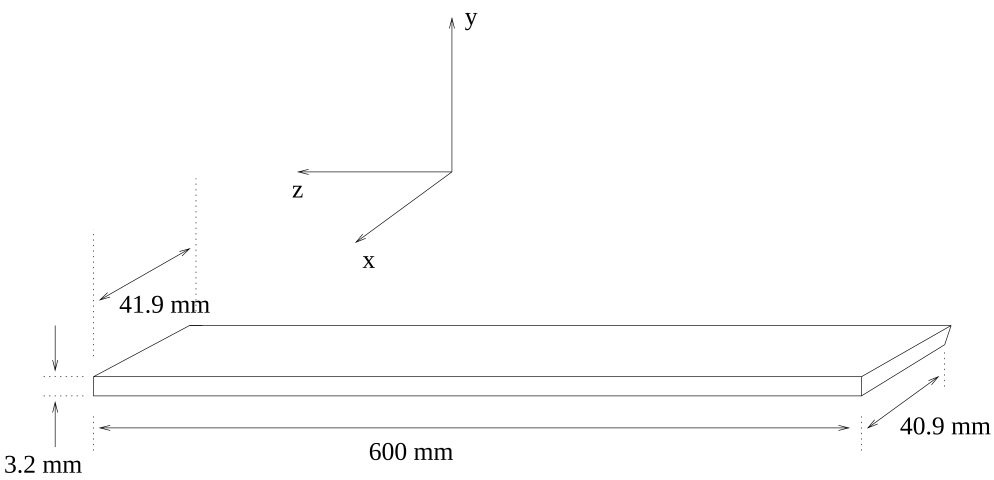

Figure 3.12: *Geometry of plastic veto stave. Not shown are the light guides and photomultipliers at each end.*

In order to measure the scintillator light output nonuniformities and attenuation lengths, the staves have been coupled to light guides and arranged in the tomography box as follows:

- The staves have been arranged in the box in stacks of three, separated vertically by aluminum spacers. In this way, it is possible to determine both light output and timing information.

- Burle S83062E bialkali cathode photomultiplier tubes have been coupled with an air gap to the lightguides at each end of the stave, with HV and signal cables feeding through from the electronics outside the box. The electronics logic is essentially the same as that of the CsI crystal tomography, a schematic of which is shown in Figure 3.3.

- The trigger consists of a signal from any one of the the six ADC channels, in coincidence with both plastic scintillators 'SB1' and 'SB2'.

As a first check in the analysis, one can plot the reconstructed entry and exit points of the cosmic muons intersecting the staves, extracted from wire chamber information. The results serve to check the reconstructed geometry and orientation of the set-up. Figure 3.13 shows the extracted entry and exit points for one stave, in the $x-y$, $x-z$, and $y-z$ planes.

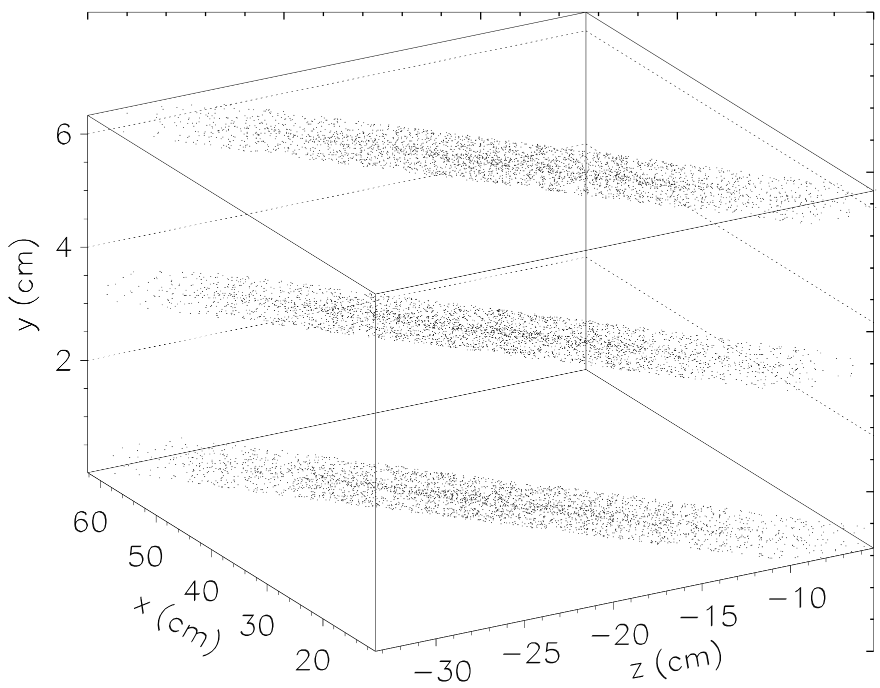

Figure 3.13: *Reconstructed coordinates of cosmic muon hits in plastic veto stave.*

The axial light output per unit pathlength can be plotted for each end of the stave, using the appropriate ADC channel value divided by the calculated pathlength. A typical plot of the light output per unit pathlength against the axial direction is shown in Figure 3.14, measured from both ends of the stave. By

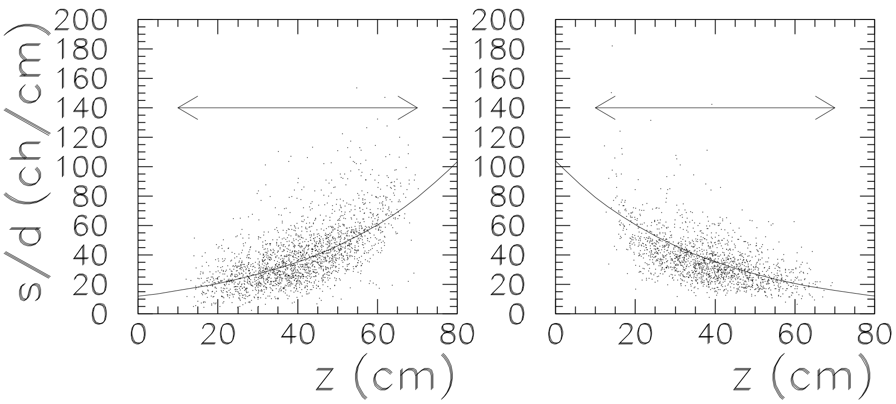

Figure 3.14: *Light output per unit pathlength as a function of axial direction for plastic veto stave, measured from both ends of the stave. The arrows represent the length of the actual stave.*

fitting the scatter plot with an exponential function of the form $f(x) = e^{\lambda x + C}$, where λ and C are constants, one can determine the 1/e attenuation length λ^{-1}. The fit was done using the "maximum likelihood" method described in Section 3.3.1. The measured attenuation lengths have been tabulated for the six studied staves in table 3.2. A conceptual diagram of the light attenuation along the stave is shown in Figure 3.15

The transverse light output per unit pathlength is plotted in Figure 3.16, measured from both ends of the stave. The plots have been fit with a straight line, the slope of which can be used to calculate the transverse nonuniformity in percent per centimeter. The results are reported in table 3.2.

In order to view the light output per unit pathlength without the attenuation, it is useful to plot the 'geometric mean' M of the two ADC values from each end

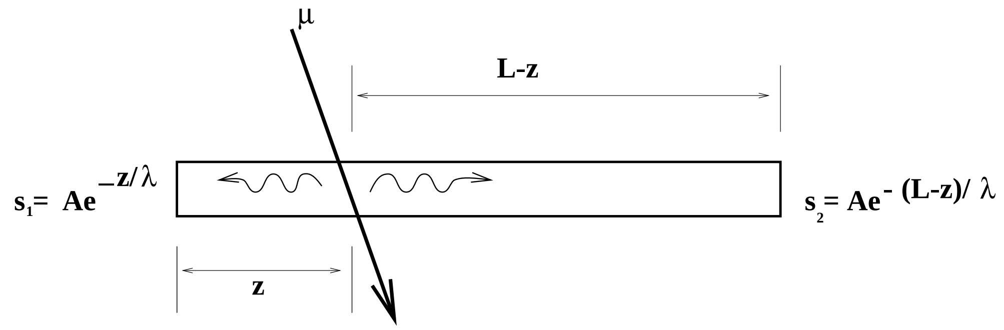

Figure 3.15: *Light attenuation along the length of a plastic veto stave.*

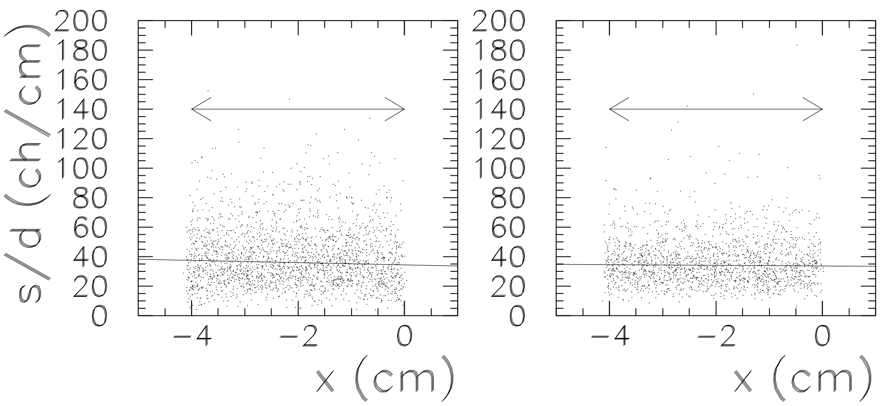

Figure 3.16: *Light output per unit pathlength plotted against the transverse direction for one plastic veto stave.*

of the stave. This quantity is defined as

$$M = \sqrt{s_1 s_2}, \tag{3.6}$$

and is independent of position. The geometric mean in the axial direction is plotted in Figure 3.17. From the figure, one can confirm that the geometric mean of the ADC values from each end of the stave is constant with respect to

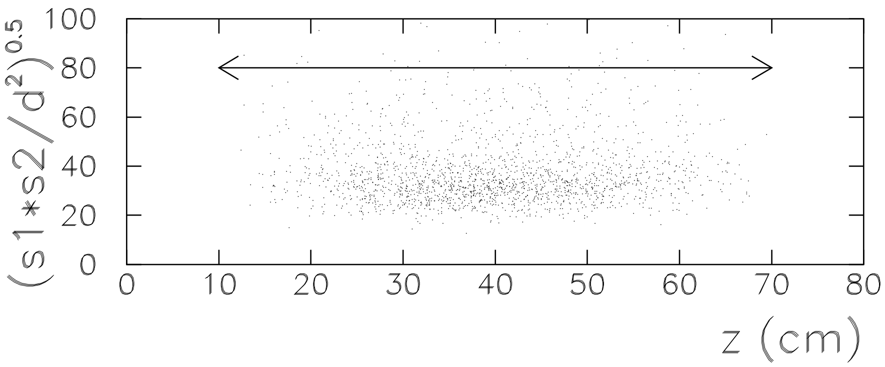

Figure 3.17: *Geometric mean of the light output per unit pathlength for one stave, in the axial direction. The arrow represents the length of the stave.*

position.

The light output per unit pathlength can also be reconstructed in two dimensions. A typical example is shown in Figure 3.18, which depicts the light output per unit pathlength in both the axial and transverse directions, from each end of the stave.

As a check in the tomography measurements, it is useful to calculate the index of refraction for each stave. This can be done by graphing $\ln(s_1/s_2)$ against $t_1 - t_2$, where s_1 and s_2 are the ADC values at each end of the stave, and t_1 and t_2 are the TDC values for each end of the stave. Figure 3.19 shows such a plot, with the straight line fit used to determine the slope. This fit was also done with the maximum likelihood method. From Figure 3.15, s_1 and s_2 have the values

$$s_1 = Ae^{-\lambda x} \tag{3.7}$$

$$s_2 = Ae^{-\lambda(L-x)}. \tag{3.8}$$

If the velocity of light in the stave is v, then $t_1 = x/v$, and $t_2 = (L - x)/v$.

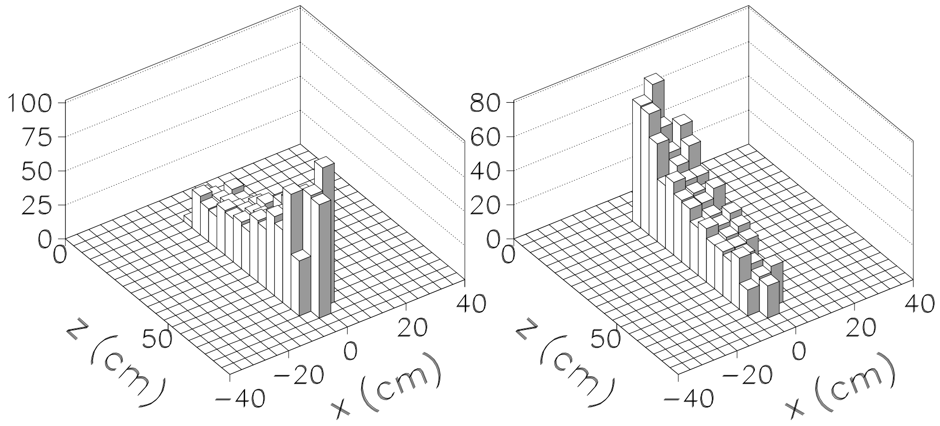

Figure 3.18: *Reconstructed two-dimensional of light output per unit pathlength for plastic veto stave. Each histogram represents the output read by one photomultiplier tube at the end of the stave.*

Consequently, the slope of a graph of $\ln(s_1/s_2)$ plotted against $t_1 - t_2$ is equal to $-\lambda v$. By measuring this slope m, one can calculate the effective index of refraction n in the following way:

$$n = \frac{c}{-m/\lambda}. \tag{3.9}$$

Table 3.2 lists the results of the plastic veto stave tomography. The error bars are quite large in some cases. As explained above, the cosmic muon statistics were limited by a malfunction in the multi wire drift chambers. Another contribution to the uncertainty was the nonuniform acceptance of the CMT apparatus over its active area. This led to difficulty in determining the attenuation lengths accurately from a fit to the data. The expected attenuation length for the Bicron BC-400 plastic scintillator material is 160 cm. [3]. However, this specification has been measured for a 1×20×200 cm cast sheet of the plastic scintillator material. This difference in geometry from that of the PIBETA plastic veto hodoscope

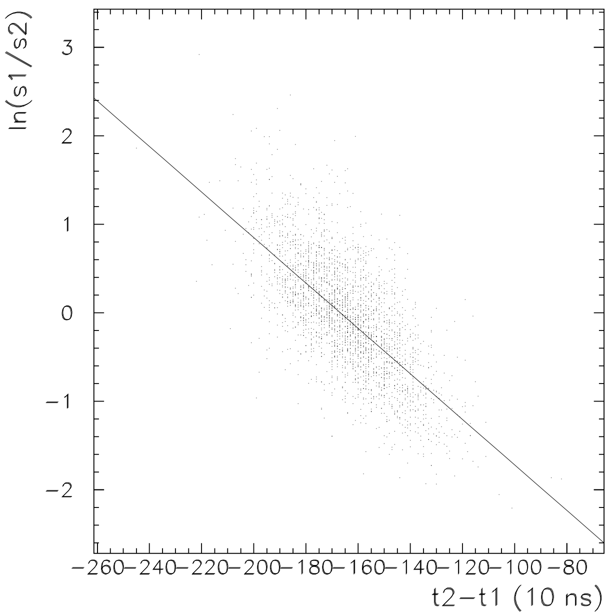

Figure 3.19: *Graph of the log of the ratio of the two ADC values from each end of one plastic veto stave, plotted against the difference in TDC values for each end of the stave. The slope of the straight line fit to this graph is used to determine the index of refraction of the stave.*

Stave	λ_1^{-1} (PMT 1)	λ_2^{-1} (PMT 2)	Transverse Nonuniformity (average PMT 1-2)	Index of Refraction
1	37±15 cm	45±50 cm	-1.3±5%/cm	2.8±1.8
2	44±350 cm	45.7±70 cm	-1.0±4%/cm	2.3±3.2
3	207±200 cm	50±200 cm	1.1±5%/cm	1.7±0.7
4	31±130 cm	36±65 cm	0.9±4%/cm	2.7±2.6
5	48±100 cm	51±150 cm	1.8±5%/cm	7.1±40.0
6	47±100 cm	36±100 cm	0.1±4%/cm	2.0±1.3

Table 3.2: *Tomography results for six studied plastic veto staves.*

staves accounts for the tendency toward a discrepancy between the measured values in table 3.2, and the manufacturer's specifications.

The expected value for the index of refraction n of the plastic stave material is 1.5. From the table it is clear that the measured values for n tend to be higher than this value. This is an expected result, due to the increased pathlength travelled by light undergoing many total internal reflections along the length of the stave. The TDC values for the light output depend on the discrimator levels, as only a small fraction of light travels straight down the length of the stave to stop the TDC early. The majority of the emitted light is reflected multiple times in the stave before reaching the PMT, which results in a larger TDC value and a larger value for n.

Chapter 4

Energy Calibration of Pure CsI Detectors

4.1 First and Second Level Pedestal Corrections

The pedestal value of the ADC output is an effective offset. It is defined by the integration of the excess signal from the gate pulse which allows current to pass into the ADC. In order to correct for this offset, the pedestal values are measured and recorded periodically during data acquisition for each ADC channel. This is done by using a clock as the trigger, which avoids the acceptance of data signals from the various detectors. Then, during the data replay, these pedestals are subtracted from their respective ADC channels, on an event by event basis.

Following the first (absolute) pedestal subtraction, a second pedestal subtraction algorithm is implemented to remove low energy common mode noise from the data. The second pedestal subtraction algorithm works as follows:

- Groups of ADC channels are defined according to observed correlations in their noise spectra.

- For each event, the algorithm selects the channel from each group with the lowest ADC value. The detector associated with this channel is assumed not to have registered light from an electromagnetic shower.

- A noise threshold is defined which is equal to the lowest ADC value in each group plus a predefined offset.
- The events in each group which fall below this noise threshold are averaged, and then subtracted from each channel's ADC value in the group.

Figure 4.1 depicts a typical pedestal spectrum, before and after the second pedestal subtraction algorithm. One can see that noise level decreases from ≈40 channels (1.6 MeV) to about 5 channels (0.2 MeV). Figure 4.2 shows the 44 CsI pedestal spectra, after the first and second pedestal subtraction have been implemented. By inspection of this histogram, one can see that a summing threshold of $T_{CsI} = 5$ channels (0.2 MeV) can be chosen to separate noise from data. All CsI ADC values which are below T_{CsI} are considered to be noise and are ignored, while all that are above T_{CsI} are summed as data.

The first and second pedestal subtraction algorithms are also applied to the 64-element NaI array, after which one can safely select $T_{NaI} = 10$ channels (0.4 MeV). Figure 4.3 shows the 64 NaI pedestal spectra after the first and second pedestal subtractions. This discrepancy between T_{CsI} and T_{NaI} is due to the fact that the ADC gate width for the NaI detectors was longer (800 ns) than that of the CsI detectors (100 ns). Hence, more low energy noise was integrated by the ADC for the NaI channels.

Finally, one can see the root mean square values for the corrected CsI and NaI pedestal histograms in Fig. 4.4. The root mean square value x_{rms} is calculated as

$$x_{rms} = \sqrt{\frac{1}{N}\sum_i (x_i - \mu)^2}, \tag{4.1}$$

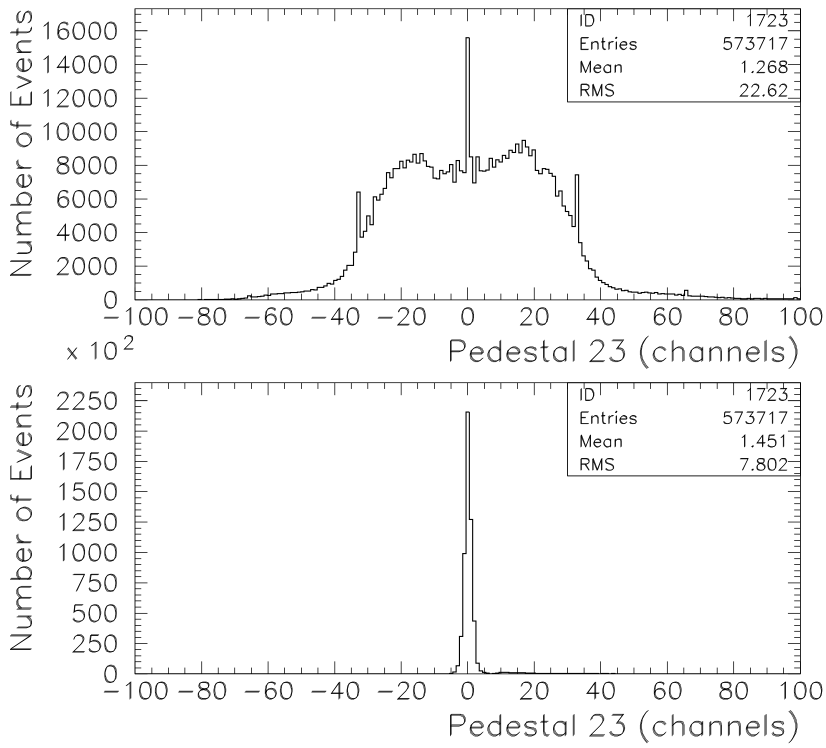

Figure 4.1: *CsI Pedestal spectra before and after second pedestal subtraction algorithm has been implemented.*

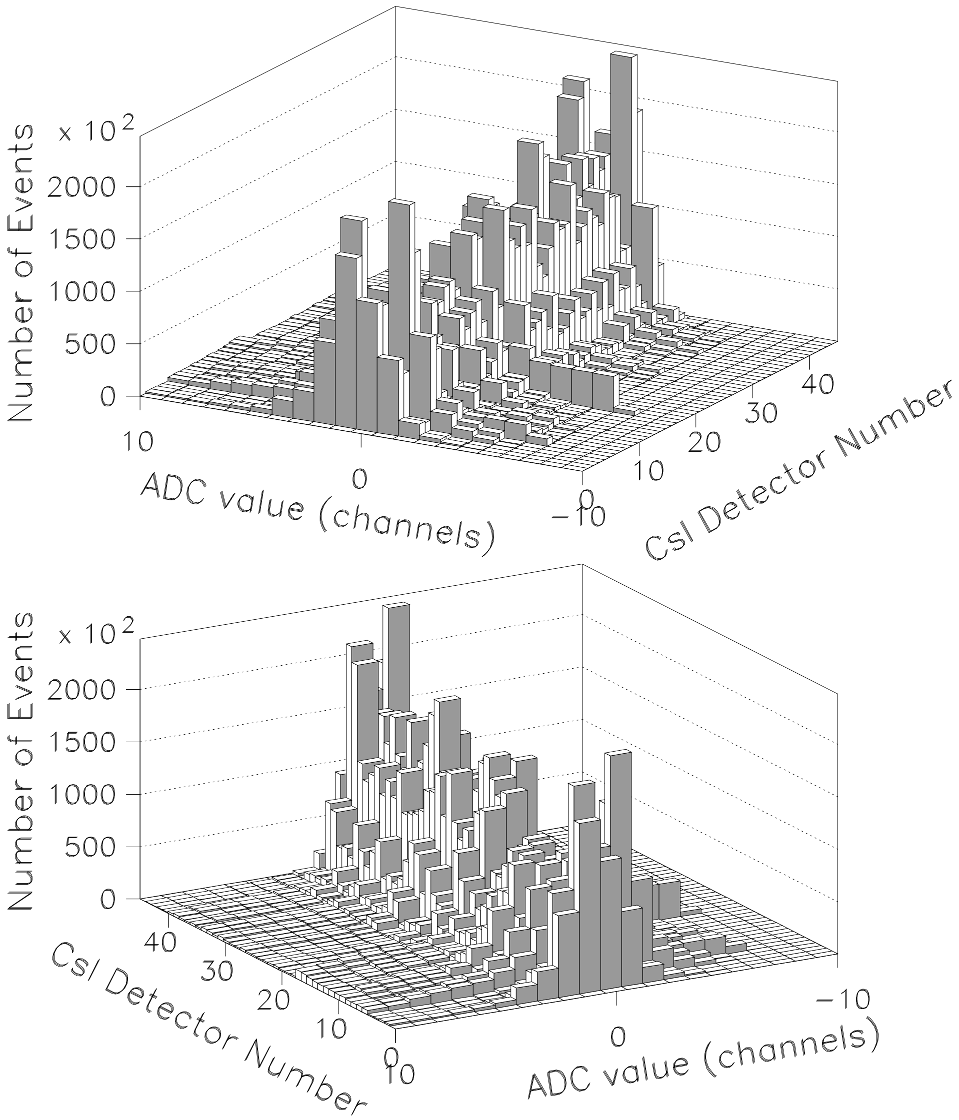

Figure 4.2: *Final CsI pedestal spectra after both first and second pedestal corrections, viewed from two different angles.*

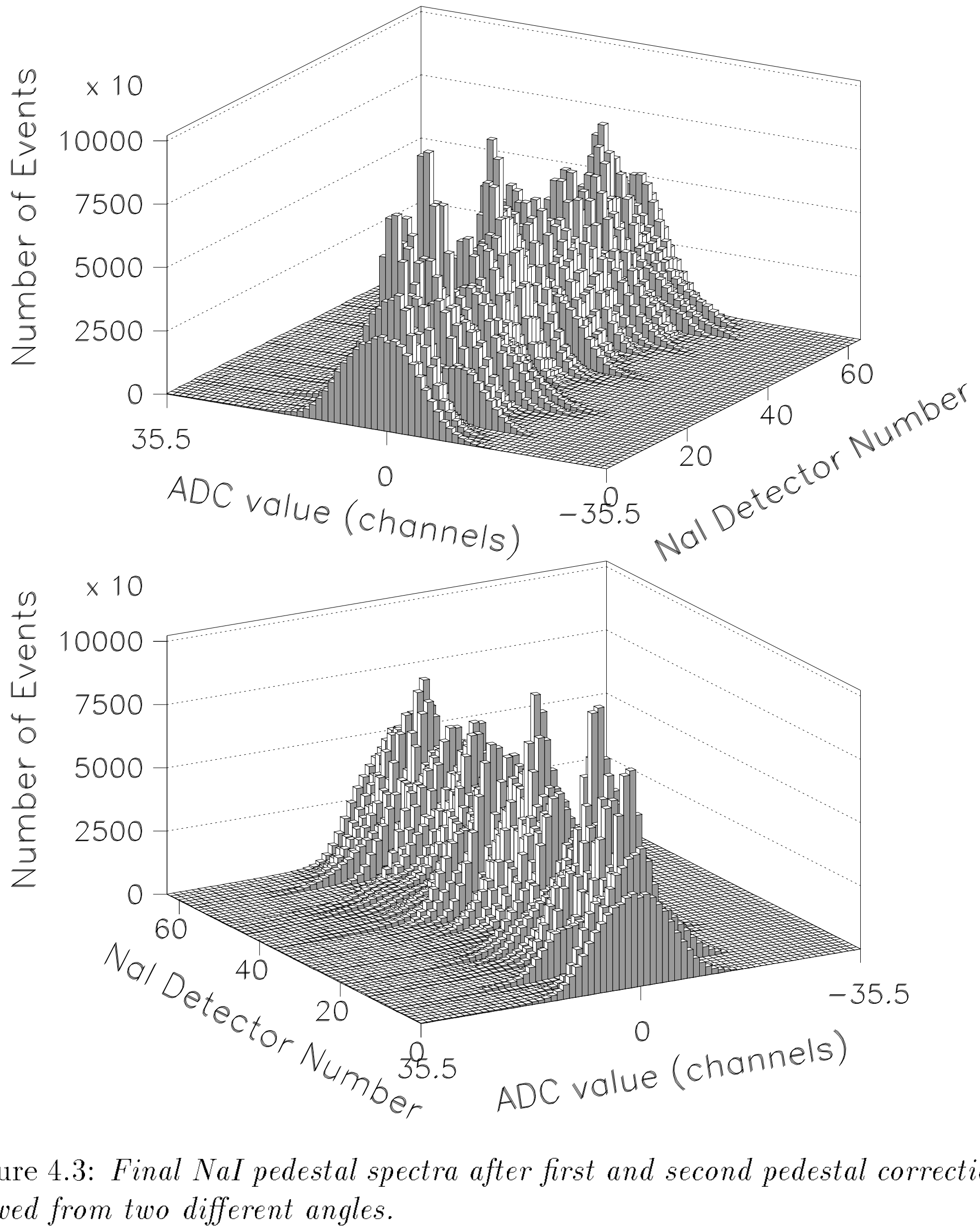

Figure 4.3: *Final NaI pedestal spectra after first and second pedestal corrections, viewed from two different angles.*

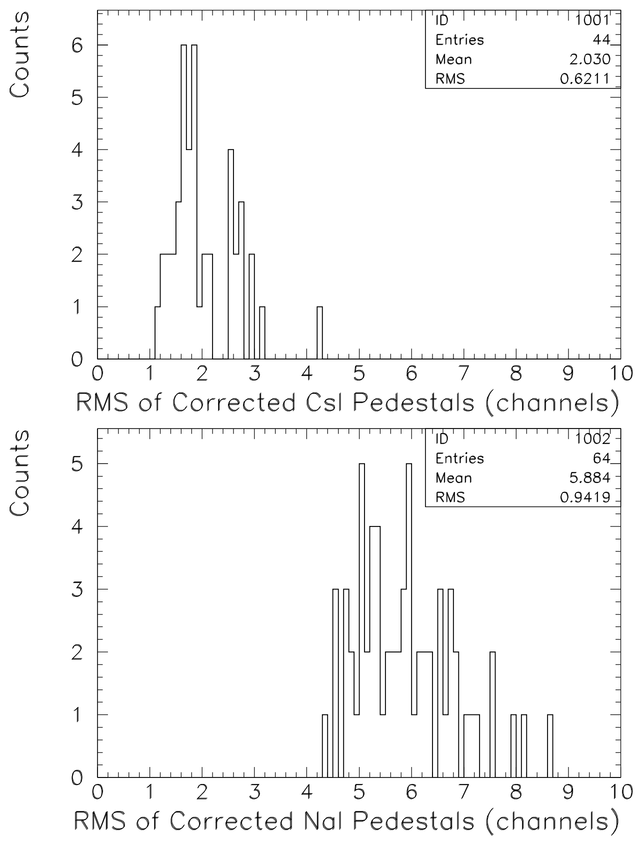

Figure 4.4: *Root mean square x_{rms} values of the corrected CsI and NaI ADC pedestal histograms.*

where x_i is the ADC value of the ith bin in the pedestal histogram, μ is the mean, and N is the total number of events.

4.2 Gain Matching

4.2.1 Gain Matching Algorithm

In the 1997 data run, there were two beams: one of 70 MeV/c positrons, and one of 116 MeV negative pions (see Chapter 2). Clearly, the 70 MeV/c positrons can be treated as monoenergetic particles in the gain matching. Likewise, the 116 MeV/c π^- beam incident on the liquid hydrogen target leads to the reaction $\pi^- p \rightarrow \gamma n$, where the outgoing photon is monoenergetic at 129 MeV/c. Consequently, it is possible to apply nearly identical gain matching algorithms to data from both beams, based on the presence of monoenergetic particles in each one.

The detector gain matching for monoenergetic particles is accomplished by an iterative algorithm which aligns the peak positions of the summed 44 CsI and 64 NaI detector histograms. Each of these histograms contains the summed energy deposited into the calorimeter per event, with the requirement that 50% of the shower be contained in the crystal of interest. By applying the software gain corrections produced in the gain matching algorithm, the peak positions are placed into a channel which is close to the individual online peak positions. These online peak positions were chosen based on the following:

- The ADC unit has 4096 channels.
- Events which are relevant to the Panofsky Ratio measurement and positron runs deposit up to 100-120 MeV into the calorimeter.

Therefore, the 70 MeV positron peak is placed into approximately channel 2100, and, using slightly higher ($\approx$2-3%) PMT high voltages, the 129 MeV photon peak is placed into channel ≈3000. Finally, after the gain matching, an absolute energy calibration is performed based on the results of the GEANT [7] Monte Carlo simulation of the experiment.

The first step in the gain matching algorithm is to determine which crystals were actually illuminated by the monoenergetic particles. This is done simply by counting the number of events per detector in the histograms described in the previous paragraph. Only crystals which contain a minimum number of events in the histogram are included in the algorithm.

Next, the peak positions of the summed spectra are determined through a fit with a Gaussian-exponential function. This function $f(x)$ is described by four parameters: height of the Gaussian h, mean of the Gaussian μ, standard deviation of the Gaussian σ, and a transition point t between the Gaussian and exponential function (see Fig. 4.5). By requiring that $f(x)$ and $f'(x)$ be continuous at $x = \mu + t$, the function takes the following form:

$$f(x) = \begin{cases} he^{\frac{-(x-\mu)^2}{2\sigma^2}} & \text{if} \quad x > (\mu + t) \text{ and } t < 0 \text{ or} \\ & \phantom{\text{if}} \quad x < (\mu + t) \text{ and } t > 0, \\ e^{\frac{t}{\sigma^2}\left(\frac{t}{2} - (x-\mu)\right)} & \text{if} \quad x < (\mu + t) \text{ and } t < 0 \text{ or} \\ & \phantom{\text{if}} \quad x > (\mu + t) \text{ and } t > 0. \end{cases} \tag{4.2}$$

A typical fit with this function to a data spectrum resulting from a 70 MeV monoenergetic positron beam is shown in Fig. 4.6.

After determining the peak position μ from the fit to the data, the gain correction factor Y is calculated as

$$Y = \frac{X}{\mu}, \tag{4.3}$$

where X is the required peak position. The new gain G' is related to the previously calculated gain G by

$$G' = G \times Y. \tag{4.4}$$

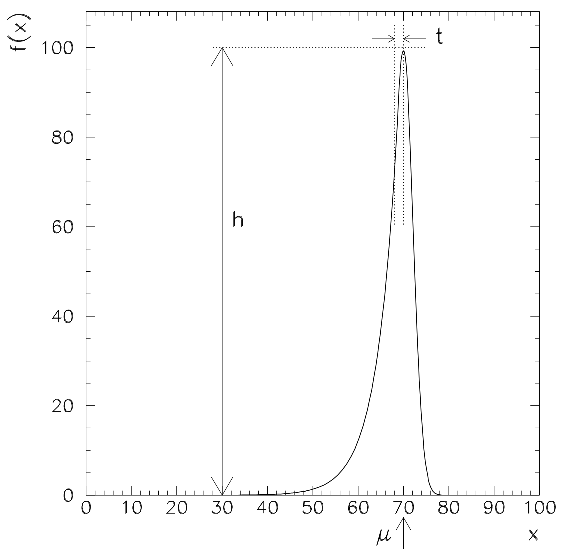

Figure 4.5: *Gaussian-exponential function $f(x)$, defined by the height h of the Gaussian, the mean μ of the Gaussian, the standard deviation σ of the Gaussian, and the transition point t between Gaussian and exponential.*

The uncertainty in G' is propagated through the iterations. From the theory of error propagation [2], for $x = f(u, v)$,

$$\sigma_x{}^2 = \sigma_u{}^2 \left(\frac{\delta x}{\delta u}\right)^2 + \sigma_v{}^2 \left(\frac{\delta x}{\delta v}\right)^2 + 2\sigma_{uv}{}^2 \left(\frac{\delta x}{\delta u}\right)\left(\frac{\delta x}{\delta v}\right), \tag{4.5}$$

and the error in the correction factor Y is calculated to be

$$\sigma_Y = \frac{X}{(\mu)^2}\ \sigma_\mu. \tag{4.6}$$

Hence, the uncertainty in G' is propagated through iterations of the algorithm as

$$\sigma_{G'}{}^2 = \sigma_Y{}^2 (G')^2 + \sigma_G{}^2 (Y)^2 \tag{4.7}$$

$$= \frac{X}{(\mu)^2}\ \sigma_\mu^2 (G')^2 + \sigma_G{}^2 (Y)^2. \tag{4.8}$$

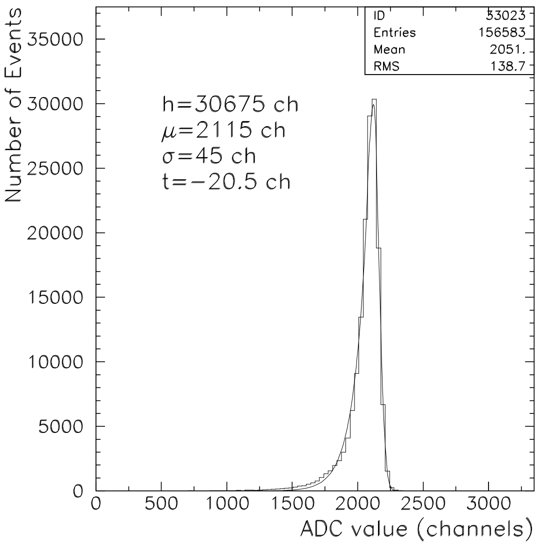

Figure 4.6: *Fit with a Gaussian exponential function, to data resulting from a 70 MeV monoenergetic positron beam.*

The gain matching algorithm is allowed to iterate until the average change in the gains $\overline{\Delta_{gain}}$ is less than the average standard deviation of the correction factors Y,

$$\overline{\Delta_{gain}} <= \overline{\sigma_Y}. \tag{4.9}$$

When this condition is met, the gain matching algorithm has converged. Fig. 4.7 shows a plot of the standard deviation σ of the CsI calorimeter's response function in a 70 MeV positron beam plotted against the iteration number of the gain matching algorithm. One can see that the energy resolution of the calorimeter improves with the convergence of the algorithm.

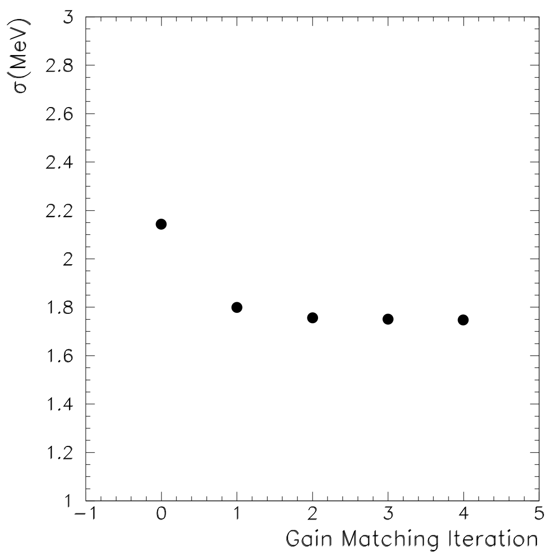

Figure 4.7: *Standard deviation σ of the CsI response function in a 70 MeV positron beam, plotted against the iteration number of the gain matching algorithm.*

4.2.2 Temporal Stability

The temporal stability of the CsI detector gains can be studied by plotting the software gains against the data run number, for each illuminated CsI crystal. Figure 4.8 shows this plot for the CsI detectors during ~100 runs, or a time period of ~4 days. One can see that the gains show a large shift beginning at run 492, at which time the CsI array was warmed from ~14°C to ~25°. The software gains increase to compensate for the fact that the CsI crystals output less light at warmer temperatures.

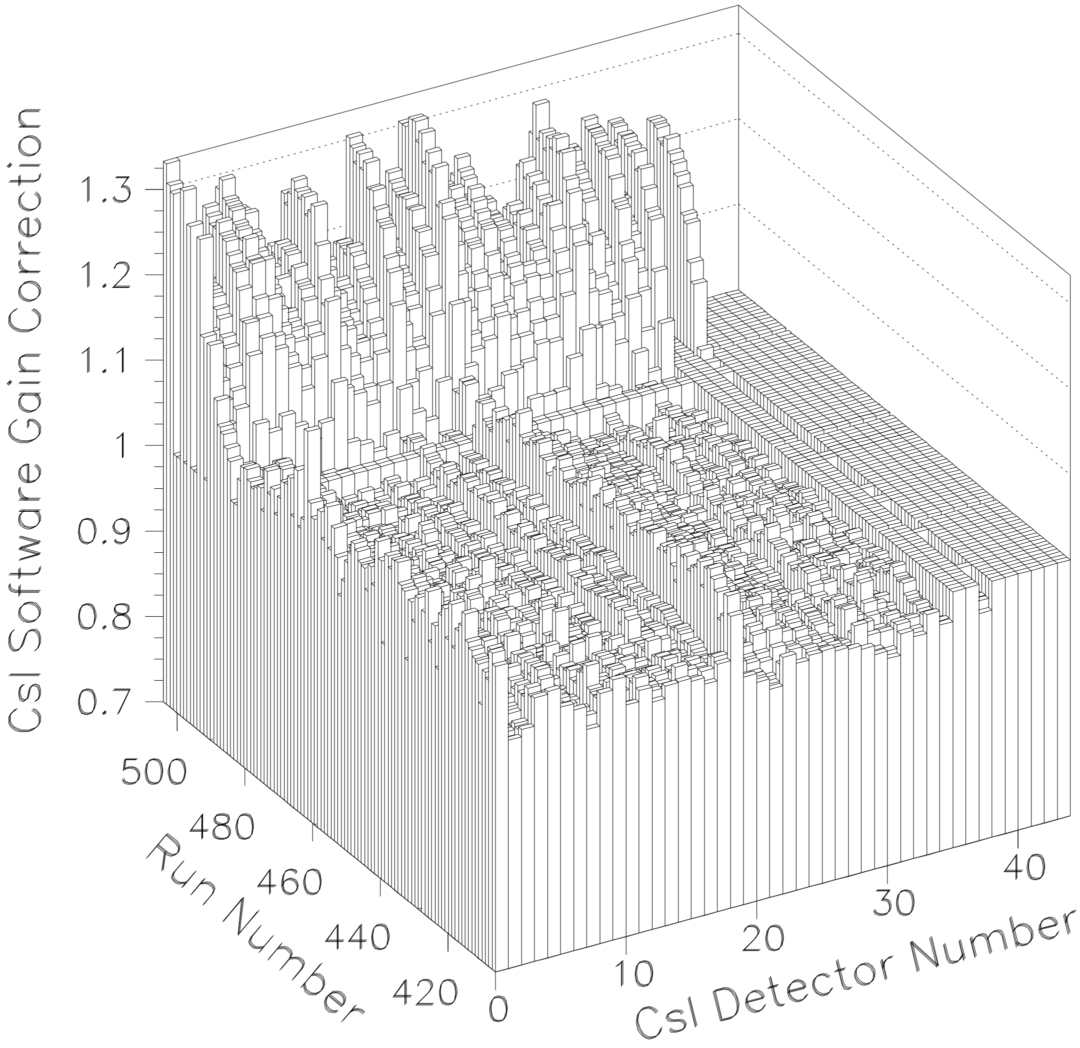

Figure 4.8: *Gain plotted against Run Number for the CsI detectors.*

Chapter 5

Angular Resolution of CsI and NaI Detector Arrays

5.1 Shower Origin Reconstruction Algorithm

In order to determine kinematically the momentum of the photons from the reaction $\pi^- p \rightarrow pi^0 n \rightarrow \gamma\gamma n$, it is necessary to find the location of the photons' entry into the calorimeter. In addition, it is useful to know where the resulting electromagnetic shower originates, so that the neighboring crystal detectors may be identififed, and appropiately summed or ignored (see Chapter 6).

The origin of the shower is reconstructed from the CsI and NaI crystal ADC values (data) or energy depositions (simulation) using a geometric weighting algorithm. The algorithm works by first finding the fraction of energy q_i deposited in each crystal,

$$q_i = \frac{ADC_i}{\sum ADC}, \tag{5.1}$$

where the sum in the denominator includes all CsI or NaI detectors. Next, the coordinate x is calculated according to the weighting formula

$$x = \frac{\sum x_i q_i^{\alpha}}{\sum q_i^{\alpha}} + dx, \tag{5.2}$$

where x_i is the coordinate of the ith crystal, dx is a correction based on the angle of incidence of the particle with the detector array, and the exponent α is a constant which is defined by the nature of the shower development in the CsI and NaI arrays. The coordinates x_i of the crystals in the NaI array are defined in a Cartesian coordinate system, while those in the CsI array spherical. The values of α_{CsI} and α_{NaI} are determined by optimizing the average angular resolution of each crystal array in the GEANT Monte Carlo simulation. This optimization is discussed in Sec. 5.2.

5.2 Angular Resolution Optimization

The average angular resolution of the CsI and NaI detector arrays has been measured and optimized in the GEANT simulation. It is defined as the average angular difference $\overline{\Gamma}$ between the direction of the thrown particles in the simulation in terms of θ and ϕ, and the direction of the reconstructed shower origin coordinates in terms of θ' and ϕ'. From Equ. 1.26, this angular difference Γ takes the form:

$$\Gamma = \mathrm{acos}(\sin(\theta)\cos(\phi)\sin(\theta')\cos(\phi') + \sin(\theta)\sin(\phi)\sin(\theta')\sin(\phi') + \cos(\theta)\cos(\theta')). \quad (5.3)$$

The optimization of $\overline{\Gamma}$ for each detector has been done with respect to two parameters: the ADC weighting exponents α_{CsI} and α_{NaI} from Equ. 5.1, and the parameters λ_{CsI} and λ_{NaI} which are related to the shower penetration depth in each detector. The latter are used to calculate an angle of incidence correction in the shower origin reconstruction (see Sec. 5.2.2).

5.2.1 ADC Weighting Exponent

The values of the ADC weighting exponent α_{CsI} and α_{NaI} have been determined by optimizing the average angular resolution $\overline{\Gamma}$ of both the NaI and CsI detectors. Using the GEANT code to simulate the box spectrum of 55-83 MeV photons from the single charge exchange reaction $\pi^- p \rightarrow \pi^0 n \rightarrow \gamma\gamma n$, the average angular resolution $\overline{\Gamma}$ has been minimized with respect to α_{CsI} and α_{NaI}. The plots of $\overline{\Gamma}$ against α are shown in Fig. 5.1 for the CsI and NaI detectors. The cut imposed on these measurements requires that the sum of the energies deposited into the "inner" (See Chapter 2) detectors of each array exceed 50 MeV. From Fig. 5.1, it is clear that the optimal values for the weighting exponents are

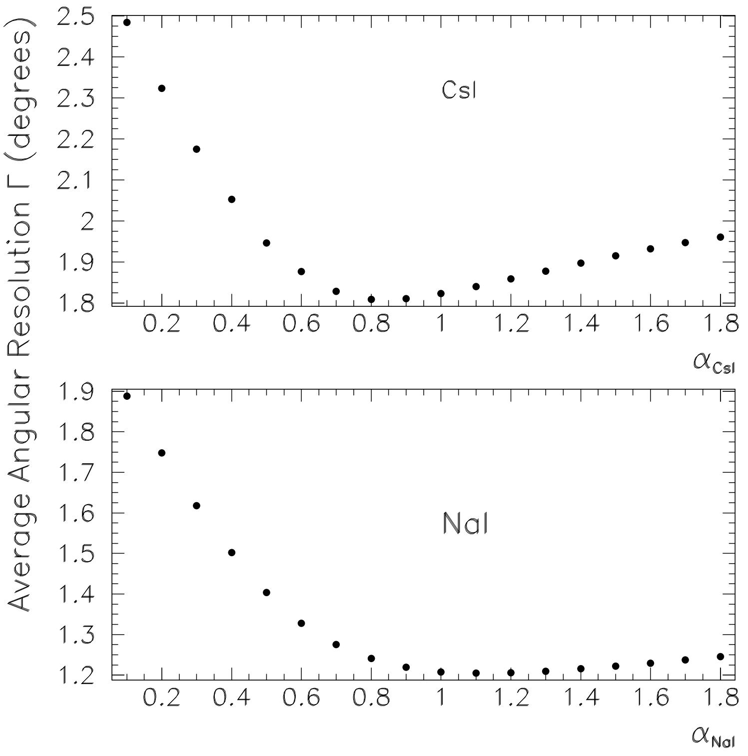

Figure 5.1: *Angular resolution plotted against the ADC weighting exponent α for CsI and NaI, with angle of incidence corrections.*

$\alpha_{\mathrm{CsI}} = 0.8$, and $\alpha_{\mathrm{NaI}} = 1.1$.

5.2.2 Shower Depth Parameter

The average angular resolution has also been minimized with respect to the shower depth parameters λ_{CsI} and λ_{NaI}. These parameters are used to calculate an angle of incidence correction which is applied (dx in Equ. 5.1) to the reconstructed shower origin coordinates. This correction is important because the incident particles are not necessarily normal to the surfaces of the crystals in the detector arrays. Such a particle, with a non-zero transverse momentum component, can result in a shower origin which is offset from the actual impact point of the particle with the calorimeter surface.

By assuming that the target is a point source, the angle of incidence of the particle can be calculated for each event. This approximation holds as long as the actual target size is small compared to the distance between the target and detector arrays.

For the NaI detector, the angle of incidence correction is calculated along the two directions in the plane of the front face of the array, $\hat{x}$ and $\hat{y}$. The technique used is similar to the one suggested by A. Bay et. al. [1]. The shift Δx (or Δy) is applied according to Fig. 5.2, where λ_{NaI} is related to the electromagnetic shower penetration depth and is a function of energy. From Fig. 5.2 one can see that $ds = \lambda_{\mathrm{NaI}}\sin(\psi)$.

For the CsI detector, which has a spherical geometry, the angular correction $d\psi$ is applied to produce a shift in the $\hat{\theta}$ and $\hat{\phi}$ directions, which are also along the front face of the array. First, the angle of incidence β_1 with the normal to the detector surface is calculated in each direction $\hat{\theta}$ and $\hat{\phi}$, as shown in Fig. 5.3. Next, because the linear correction x is small compared to the distance to the target r, one can assume that $\beta_1 \approx \beta_2$. Assuming that the linear correction x is much less than the sphere radius R, one can see from Fig. 5.3 that $x \approx$

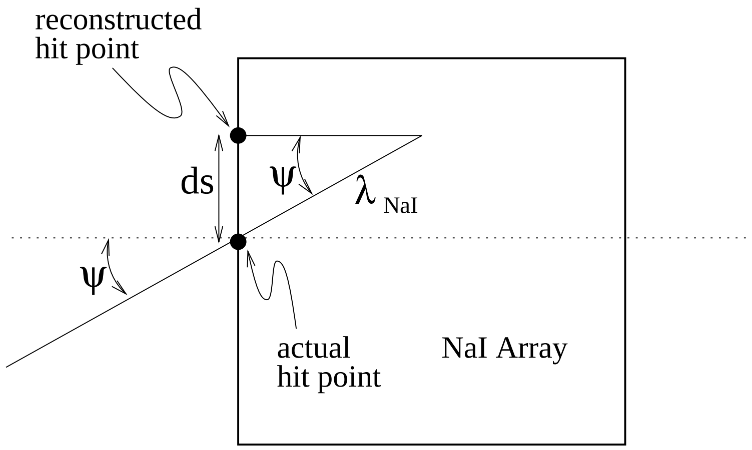

Figure 5.2: *Geometry used to calculate angle of incidence corrections $d\psi$ to shower reconstruction coordinates in NaI array.*

$\lambda_{\rm CsI}\sin(\beta_2) \approx \lambda_{\rm CsI}\sin(\beta_1)$. Finally, the angular correction $d\psi$ in both the $\hat{\theta}$ and $\hat{\phi}$ directions takes the form

$$d\psi \;\cong\; \frac{x}{r} \;\cong\; \frac{\lambda_{\rm CsI}\sin\beta_1}{r} \tag{5.4}$$

The values of the shower depth parameters $\lambda_{\rm CsI}$ and $\lambda_{\rm NaI}$ have been chosen for optimal average angular resolution. Figure 5.4 shows the plots of average angular deviations $\overline{\Gamma}$ plotted against λ, for 55-83 MeV photons from the reaction $\pi^- p \rightarrow \pi^0 n$ in the GEANT simulation. One can see that the optimal values are $\lambda_{\rm CsI} = 6$ cm and $\lambda_{\rm NaI} = 9$ cm. These penetration depths reflect the fact that the NaI crystals have a lower atomic number than the CsI crystals, shown in the larger value for $\lambda_{\rm NaI}$.

Finally, the event-by-event angular deviations Γ are plotted in Fig. 5.5, with and without the angle of incidence corrections. It is clear that there is a significant improvement with the inclusion of the correction. The CsI $\overline{\Gamma}$ decreases from 2.3° to 1.8°, and the NaI $\overline{\Gamma}$ from 1.3° to 1.2°.

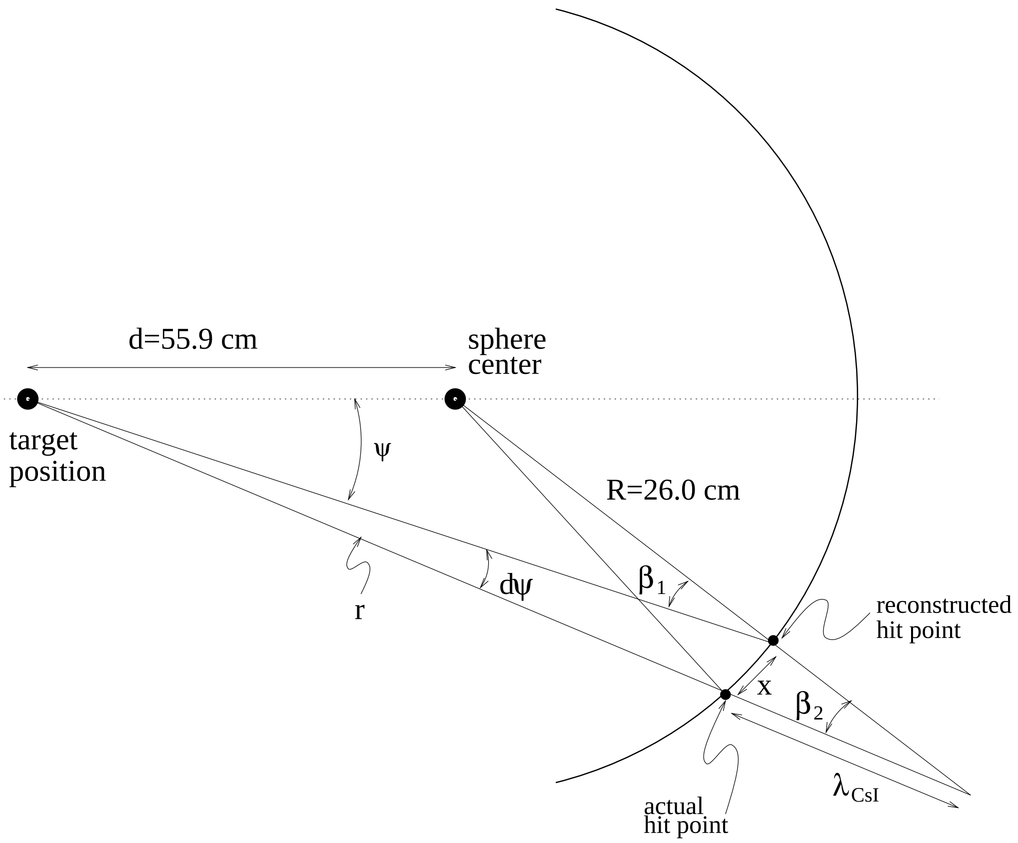

Figure 5.3: *Geometry used to calculate the angle of incidence correction $d\psi$ to the reconstructed shower coordinates in the CsI array.*

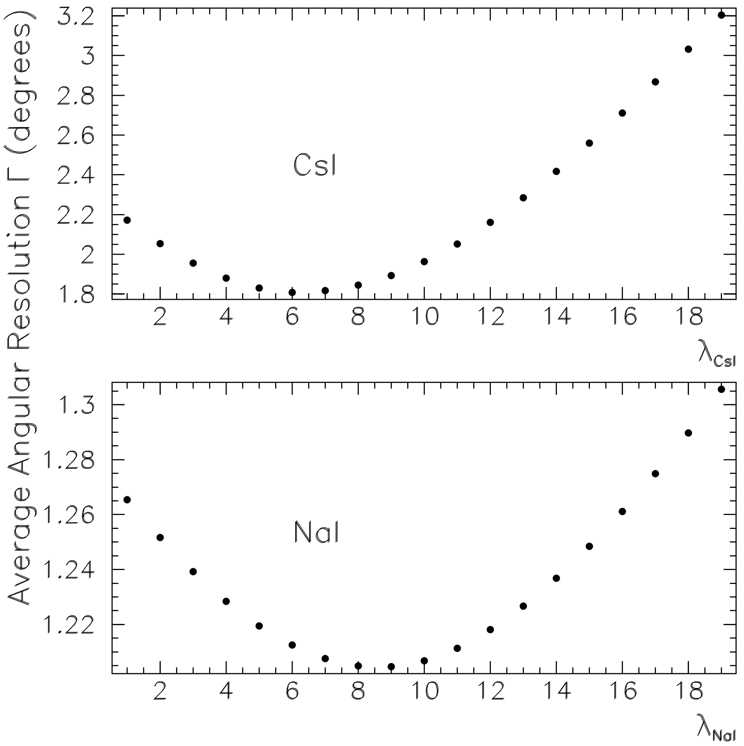

Figure 5.4: *Average angular deviation plotted against the shower penetration depth parameter λ, for the CsI array (top panel) and NaI array (bottom panel).*

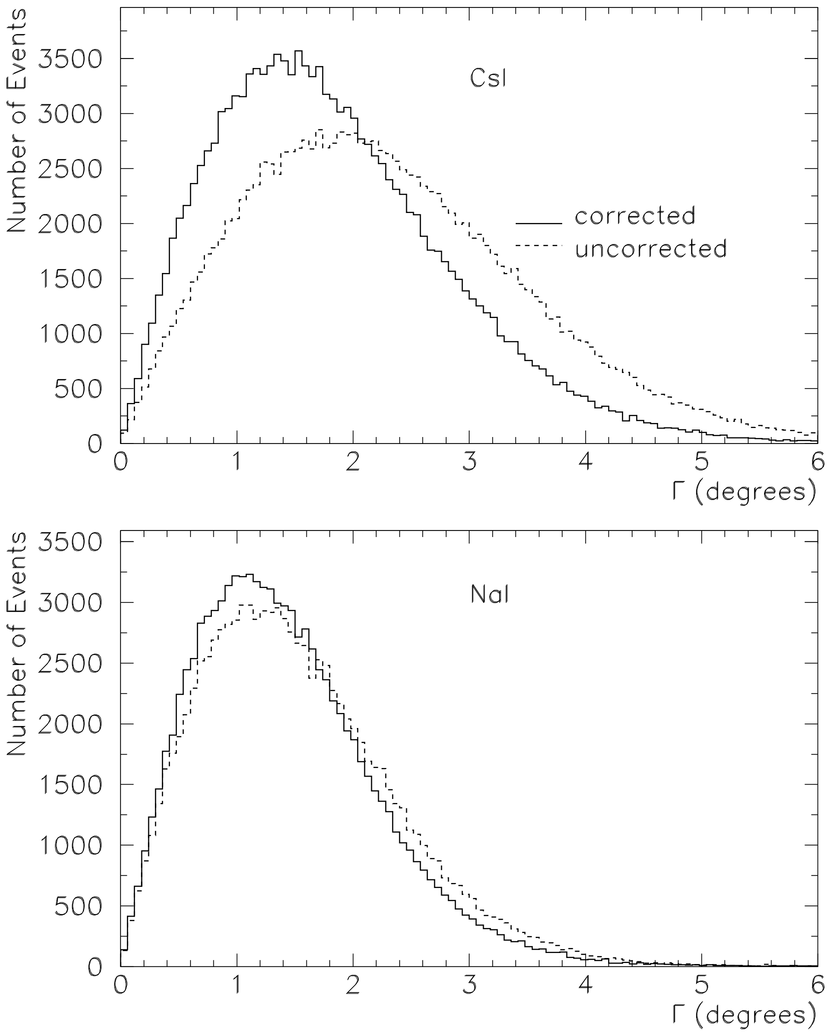

Figure 5.5: *Angular deviations* Γ*, with and without the angle of incidence corrections, for the CsI array (top panel) and NaI array (bottom panel).*

Chapter 6

Clustering Algorithm and Calorimeter Response to Photons and Positrons

The clustering algorithm discussed in this chapter is designed to facilitate the study of optimal cluster size in the PIBETA calorimeter, for single particle final states in the 44-crystal array. More specifically, for each event, only the relevant crystal ADC values should be accepted and summed. The best cluster size for events resulting in single particle final states is determined by optimizing the following three quantities:

- Event reconstruction efficiency
- Energy resolution
- Event pile-up rejection.

6.1 Cluster size definition

In order to study efficiently the effect of cluster size on the above three items, the algorithm allows for convenient cluster size variation. A cone of opening angle Ψ is defined, with its apex at the center of the detector (See Fig. 6.1). The

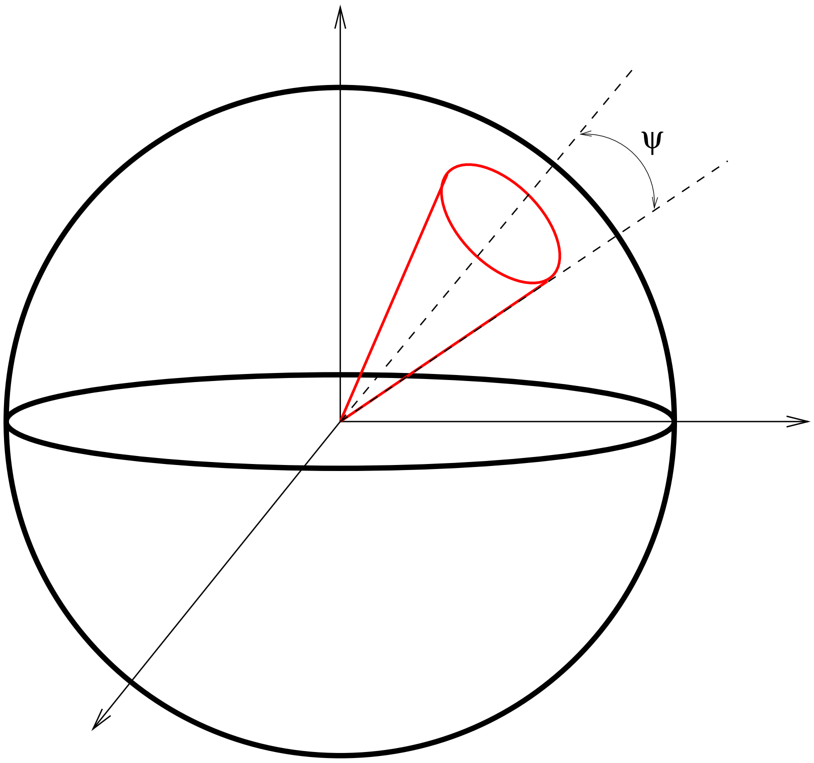

Figure 6.1: *Cone of opening angle* Ψ *to define size of cluster.*

cone opens from the center to intersect a solid angle segment of the calorimeter, centered around the previously reconstructed origin of the electromagnetic shower. This shower origin is found through an iterative combination of the shower reconstruction process discussed in Chapter 5, and the cone algorithm discussed in this chapter. The steps to reach the final cluster definition, beginning with the shower reconstruction algorithm, are as follows:

1. The CsI crystal detectors with the highest three ADC values of the array are identified.

2. Using only the ADC values from these three crystals, the shower origin is calculated according the procedure described in Chapter 5.

3. A cone of opening angle Ψ is placed around the shower origin, in order to select a cluster of crystals.

4. Using the ADC values from the cluster in step 3, the shower origin is reconstructed again.

5. Finally, the cone of opening angle Ψ is placed around the shower origin from step 4, which defines the cluster of crystals which is used to complete the optimization study.

By implementing this algorithm, and recording the number of CsI crystals which are intercepted by the solid angle cone for each opening angle Ψ, one can see the characteristic number of crystals selected for various cluster sizes. Figure 6.2 shows the number of crystals included in three cones of differing opening angles Ψ.

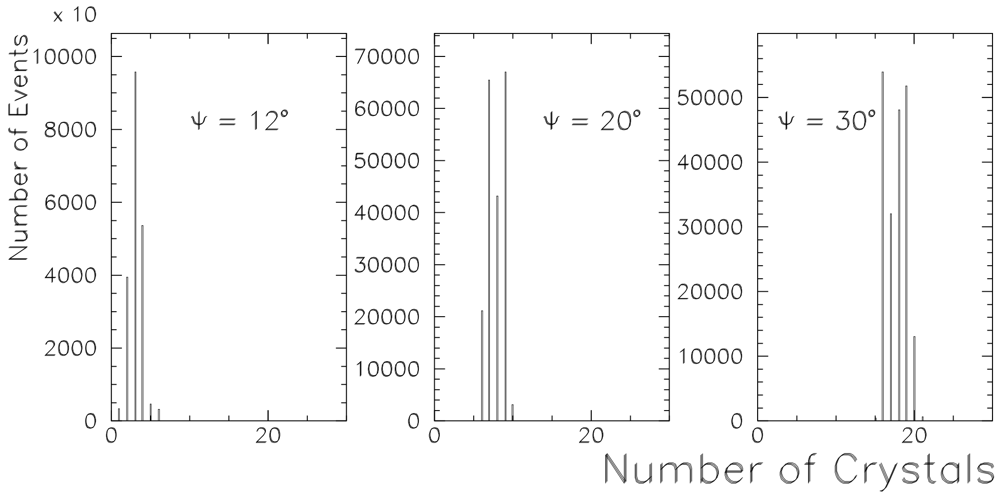

Figure 6.2: *Number of crystals intersected by the cone used for cluster definition, for three different opening angles Ψ of the cone.*

6.2 Cluster Size Optimization

6.2.1 Energy Resolution

The optimal cluster size for best energy resolution has been found by applying the cone technique to data obtained from a 70 MeV positron beam, and from a subset of photons selected from the photon box spectrum in the reaction $\pi^- p \rightarrow \pi^0 n \rightarrow \gamma\gamma n$. This subset contains photons with energies close to 55 and 83 MeV, and is selected kinematically by requiring that the relative angle ξ between the two photons be greater than 175° (See Chapter 7). By interpolating between the results for photons at these two energies 55 and 83 MeV, one can deduce and plot the results for 70 MeV photons. Finally, due to the fact that the photons were incident on the detector array isotropically, and the 70 MeV positron beam was concentrated at the center of the array, a cut has been implemented in the photon data such that less than 2 MeV are deposited in the outer ring of crystals. Figure 6.3 shows the plot of energy resolution against cluster size for these two data sets. One can see that the energy resolution appears to be optimal for a cone angle of about 30°.

For comparison, the 70 MeV positron and 70 MeV photon data have been simulated with the GEANT program. For the simulation, the 70 MeV photon results have been taken directly from the monoenergetic response, and not from the interpolation of the 55 and 83 MeV results. However, the 70 MeV photons have been thrown isotropically at the 44-element array, and a cut of 2 MeV on the outer ring has been implemented. Figure 6.4 shows the plot of energy resolution against cluster size for the simulated 70 MeV positron and photons. From this plot, one can see that the energy resolution approaches its optimal value for an opening angle of 30°.

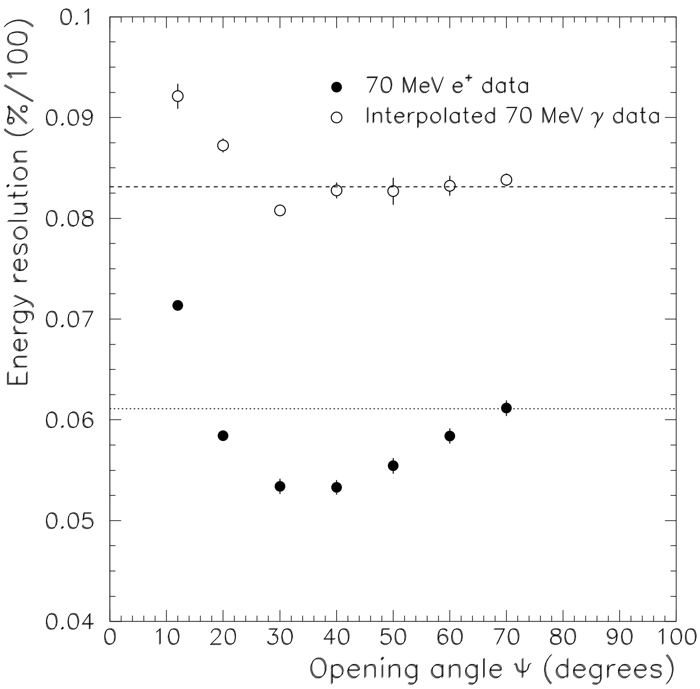

Figure 6.3: *Energy resolution, defined as full width half maximum divided by peak position of the response function, plotted as a function of the cone opening angle Ψ, for 70 MeV positron and interpolated 70 MeV photon data. The horizontal dotted lines represent the asymptotic values for 360° summing. Less than 2 MeV have been deposited in the outer ring of crystals for the photon results.*

6.2.2 Event Reconstruction Efficiency

The event reconstruction efficiency has been studied by implementing an algorithm which does the following:

1. For each event, the ADC values for the 44 CsI crystals in the array are summed.

2. For each event, the ADC values for each of the CsI crystal contained in the cluster defined by the cone from Sec. 6.1 are summed.

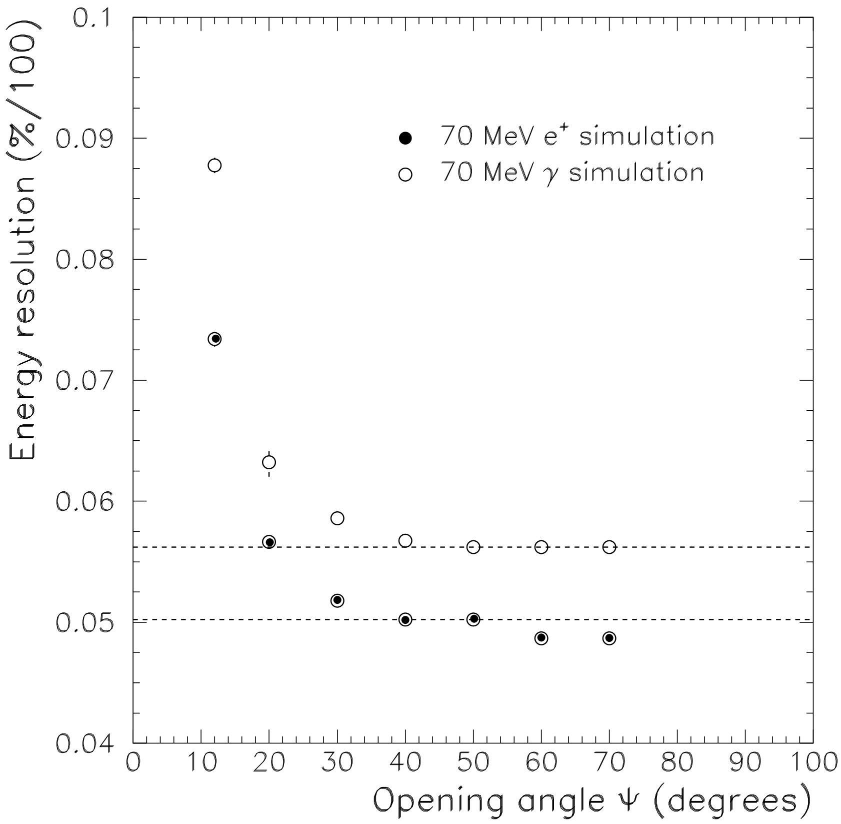

Figure 6.4: *Energy resolution, defined as full width half maximum divided by peak position of the response function, plotted as a function of the cone opening angle Ψ, for simulated 70 MeV positrons and 70 MeV photons. The dotted horizontal lines represent the asymptotic values for 360° summing.*

3. If the sums from steps 1 and 2 are both greater than or equal to 50 MeV, then the event has been successfully detected by the cluster.

4. If the sum from step 1 is greater than or equal to 50 MeV, but the sum from step 2 is less than 50 MeV, then the cluster has failed to detect the event.

Finally, the event reconstruction efficiency is defined as the number of events successfully detected by the cluster, divided by the total number of events detected by the whole array of CsI crystals.

The optimal cluster size for best event reconstruction efficiency can be inferred from a graph of efficiency plotted against Ψ, for simulated 70 MeV photons and positrons. Again, it is clear that the efficiency for $\Psi = 30°$ approaches the ideal value which occurrs at $\Psi = 360°$.

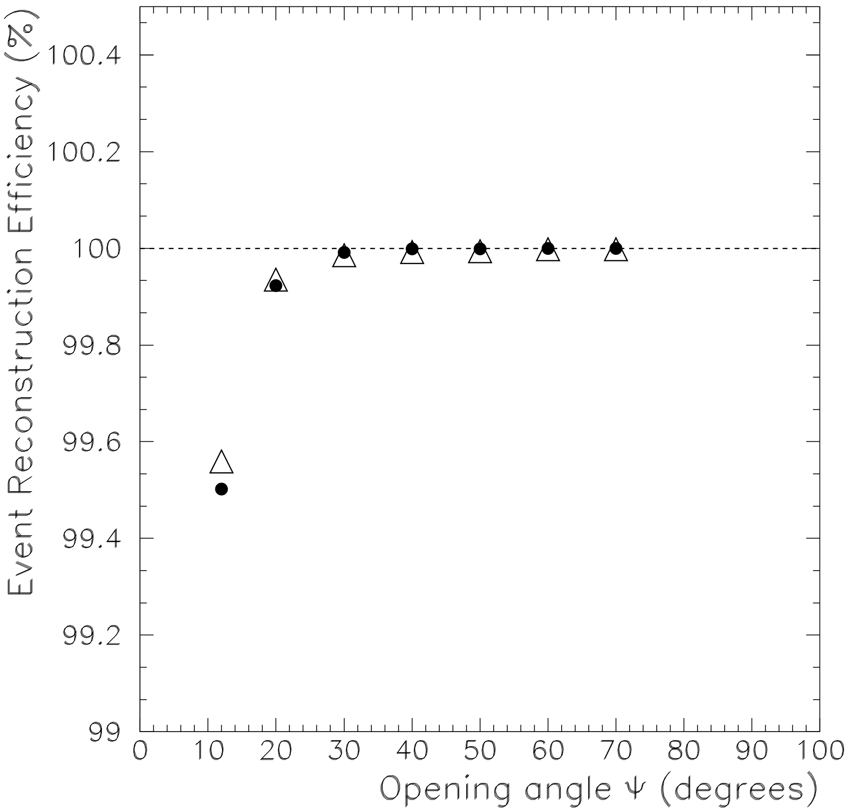

Figure 6.5: *Event reconstruction efficiency as a function of the cone opening angle Ψ, for simulated 70 MeV photons and positrons. The dotted horizontal lines represent the asymptotic values for 360° summing.*

From the plots in Figs. 6.3 through 6.5, one can deduce that the energy resolution and event reconstruction efficiency approach ideal values for a cone opening angle of $\Psi = 30°$. By inspection of the graphs in Fig. 6.2, one can see that this corresponds to a cluster size of about 17 crystals, or one central crystal surrounded by two concentric rings of crystals. This arrangement can be seen in the two dimensional projection of the whole 240-element PIBETA calorimeter, shown in Fig. 6.6.

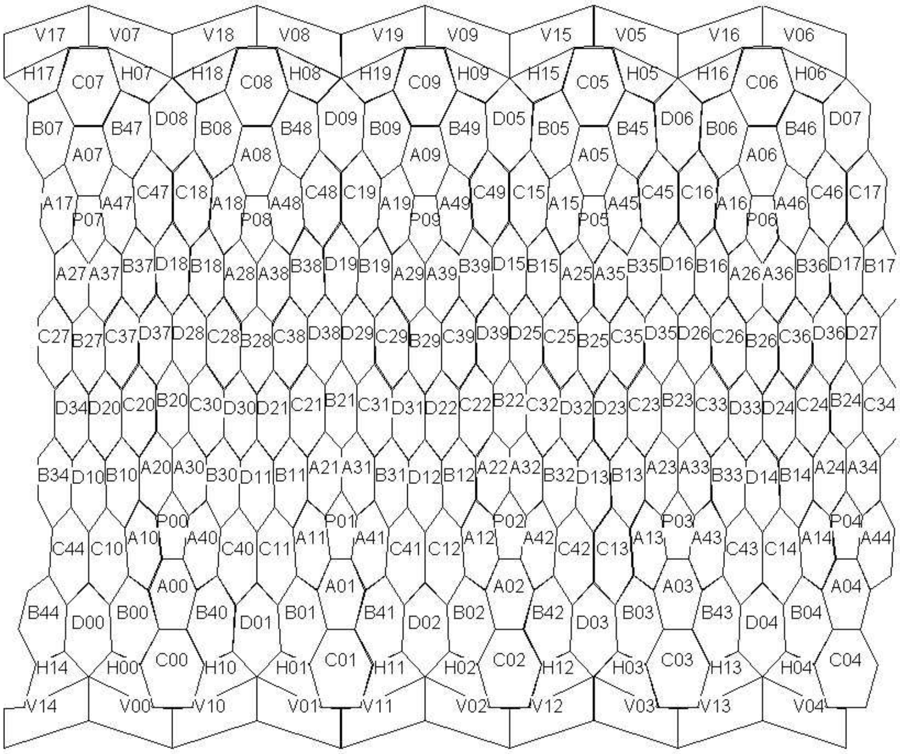

Figure 6.6: *Two dimensional view of PIBETA calorimeter. One can see that the optimal cluster size of ∼17 crystals corresponds to one central crystal surrounded by two rings of neighboring crystals.*

Chapter 7

Pion Single Charge Exchange and Capture Reactions

The pion single charge exchange and capture reactions, discussed in Chapter 1, can be detected with a two arm trigger and one arm trigger configuration, respectively. The Panofsky Ratio, defined in Chapter 1 as the ratio of the rates of these two reactions, is extracted from data taken with the single arm trigger.

7.1 Two Arm Trigger

The two arm trigger configuration requires a signal from at least one of two superclusters contained in the CsI array, in coincidence with a signal from the inner NaI detectors, and signals from both beam counters (B0 and B1). Photons emitted following the charge exchange reaction $\pi^- p \rightarrow \pi^0 n \rightarrow \gamma\gamma n$ are selected by the trigger when they are approximately anticollinear in the lab frame, along the line between the CsI and NaI arrays. The spectrum of measured opening angles between the two photons is shown in Fig. 7.1.

The momenta of the two photons are determined kinematically from the relative opening angle ξ between them, as discussed in Chapter 1. As $\xi \rightarrow 180°$, the momenta of the two photons (k_1 and k_2) approach 54.9 and 83.0 MeV,

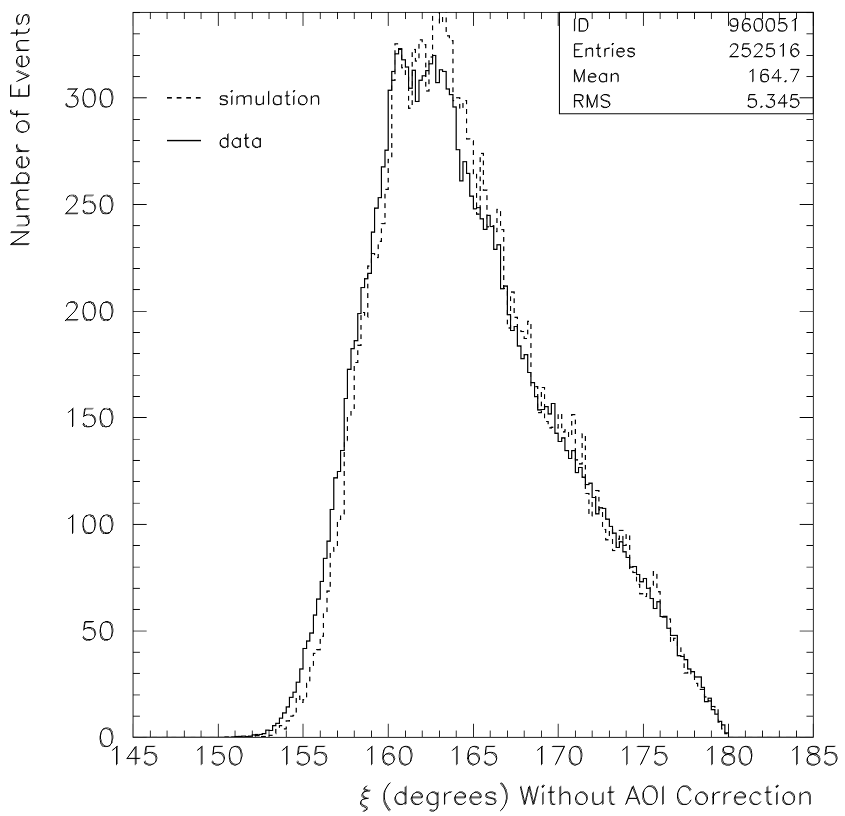

Figure 7.1: *Spectrum of measured opening angles, with angle-of-incidence (AOI) corrections, between the two photons originating from the pion single charge exchange reaction at rest. Charged particle events are vetoed by the plastic hodoscope.*

respectively, as calculated in Chapter 1. By making a cut on the relative angle ξ, one can select a range of photon energies. The spectra for four different such energy cuts are shown in Fig. 7.2. In order to check the effectiveness of the cut on ξ, one can plot the differences between the thrown energies of the photons in the simulation, and the monoenergetic endpoints of the photon box spectrum, for varying values of ξ. As the cut on ξ becomes tighter, one should see the

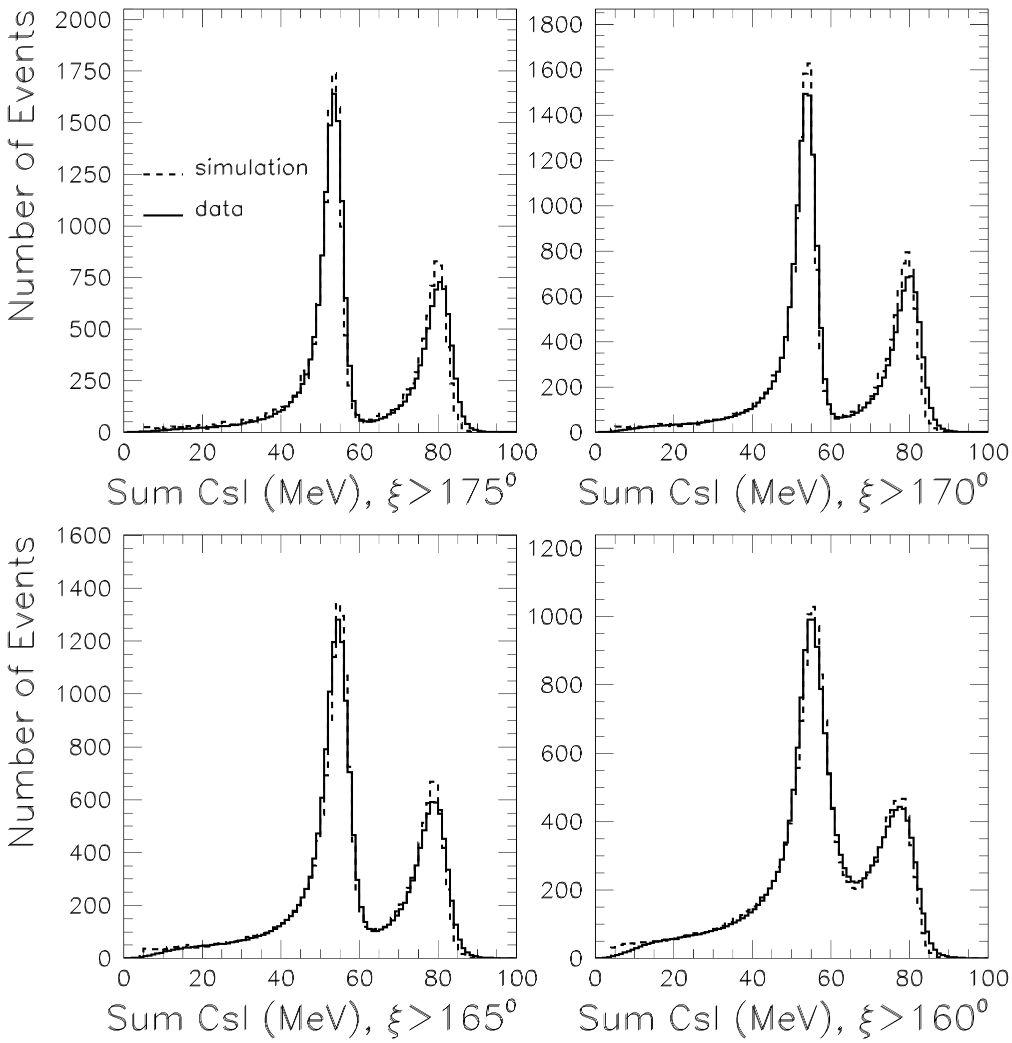

Figure 7.2: *CsI energy spectrum for the two arm trigger configuration, for four different minimum relative angles* ξ *(reconstructed) between the two photons from the charge exchange reaction. Charged particle events are vetoed by the plastic veto hodoscope.*

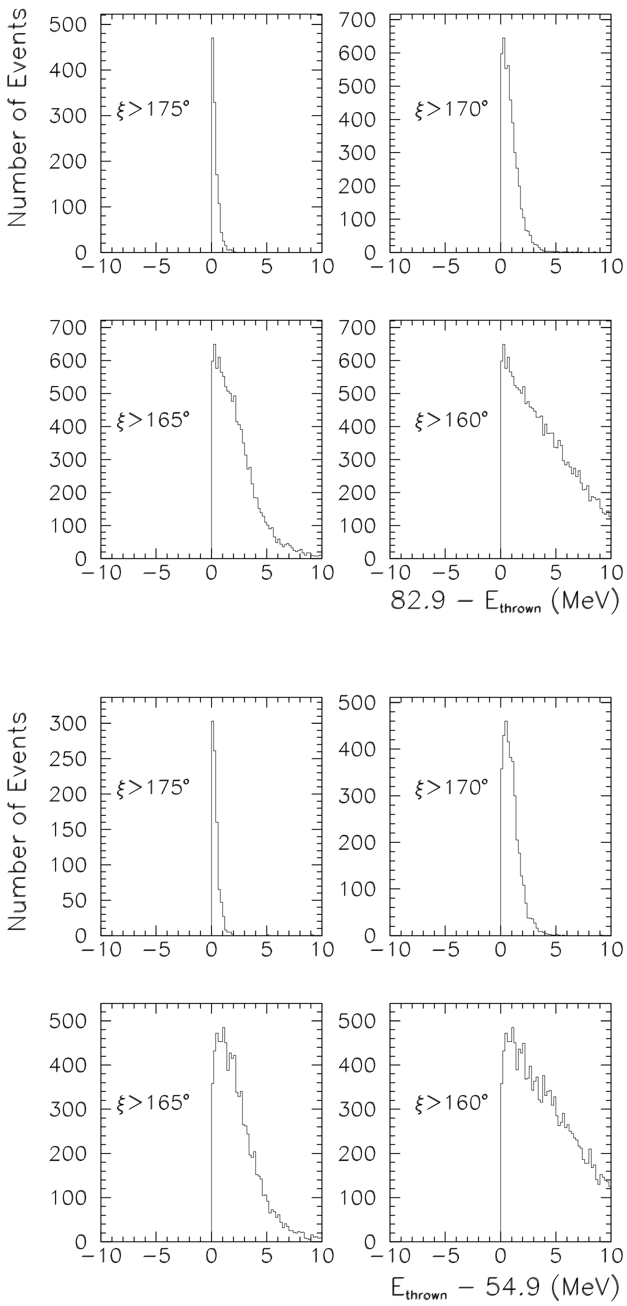

Figure 7.3: *Differences between the 83.0 MeV (top panel) and 54.9 MeV (bottom panel) endpoint and the thrown energies of the photon box spectrum from the single charge exchange reaction, for four different minimum relative angles ξ (reconstructed) between the two photons. Charged particle events are vetoed by the plastic hodoscope.*

energies of the two photons approaching 54.9 and 82.9 MeV. Figure 7.3 shows these plots. It is clear that a cut of $\xi > 175°$ is sufficient to reduce the spread in thrown energies to $\sim 1\ MeV$.

7.2 One Arm Trigger

7.2.1 Timing Corrections and Cuts

Time Slewing

An important step in the data analysis is to correct for slewing in the timing of the beam counter and the CsI detectors. The B0 beam counter slewing can be observed by plotting the B0 ADC against B0 TDC, as shown in the left panel of Fig. 7.4. The slewing is caused by the dependence of the B0 detector discriminator response on the B0 ADC pulse height. It is revealed by the amplitude-dependent timing of the data points in the scatter plot. In order to correct for the slewing, a function is devised to fit the graph and calculate the deviation from a fixed timing offset for every B0 ADC value. The best correction function was found to be a piece-wise straight line, positioned onto the scatter plot by naked-eye inspection. The resulting plot, following the slewing correction, is shown in the right panel of Fig. 7.4.

The time slewing in the CsI crystal TDC's is evident from the scatter plot in the top panel of Fig. 7.5, showing the sum of the CsI ADC values plotted against the B0 TDC. By inspecting the graph, one can see that the 129 MeV photons from the pion capture reaction $\pi^- p \rightarrow n\gamma$ appear $\sim$ 1 ns later in the B0 TDC spectrum than do the box spectrum of photons. This timing difference is caused by the fact that the CsI discriminators start the TDC for every event. The slewing results from a spread in the TDC start times based on the differing pulse heights from the individual CsI detectors. The corrected scatter plot,

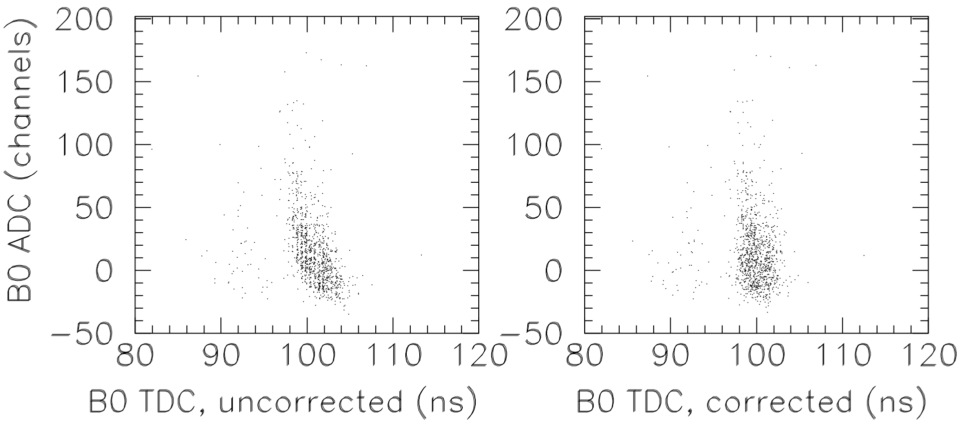

Figure 7.4: *B0 beam counter ADC value plotted against the B0 TDC value, before (left panel) and after (right panel) slewing correction.*

shown in the bottom panel of Fig. 7.5, is obtained by fitting a straight line to the uncorrected two-dimensional histogram in the top panel of Fig. 7.5, and using this line to calculate the deviation from a fixed time for every value of the sum of the CsI ADC values.

Beam Counter Timing Cut

After having corrected the beam counter timing for slewing, it is possible to make a cleaner cut in its TDC spectrum to remove accidental events and the fraction of the 8.9 MeV neutrons which passed the hardware trigger from the pion capture reaction $\pi^- p \rightarrow n\gamma$. Because of the longer time of flight of the neutrons in the CsI, they should appear earlier than the photons in the B0 TDC spectrum, as can be inferred from the single arm trigger configuration discussed in Chapter 2. By placing a cut on the data requiring that the B0 TDC value is greater than 97.0 ns and less than 104.0 ns (see Fig. 7.5), one can remove the accidental events coming from other beam buckets, as well as the characteristically slow neutrons.

Due to the timing cut on the B0 TDC spectrum, it is difficult to avoid cutting out events from the tails of the $\gamma\gamma$ box spectrum and the 129 MeV γ peak. Because of their relatively small pulse heights, these events may exhibit slewing which places them outside of the timing acceptance window. To remedy this problem, one can impose an energy threshold E_0 below which all events are ignored in the extraction of the Panofsky Ratio. In this way, the low energy events with significant TDC slewing can be ignored. By varying E_0, one can confirm that the results of the analysis remain unaffected, which proves that the events with energies above the E_0 threshold are not exhibiting enough slewing to be lost to the timing cut. Figure 7.6 shows the one arm trigger spectrum, with and without the B0 TDC timing cut. Figure 7.7 shows the subset of events which are cut out of the analysis by the B0 TDC cut. From this figure, one can see that many of the late events fall into the energy range expected of the neutrons (8.9 MeV $\cong$ 220 channels)

7.2.2 Noise in Outer Detectors

Six of the twenty-one outer detectors in the CsI calorimeter exhibit uncorrelated low energy noise. These detectors have an ADC value above 0.2 MeV two to three times more often than the other outer detectors. Moreover, this phenomenon is even more pronounced for events where more than 90 MeV is deposited into the CsI calorimeter. Figure 7.8 shows the count rates for the outer detectors for low energy events ($E < 90$ MeV), and high energy events ($E > 90$ MeV) where the effect is more prominent.

In order to check for correlations between the noisy detectors, a subset of their ADC values have been plotted against each other in Fig. 7.9. No correlation is

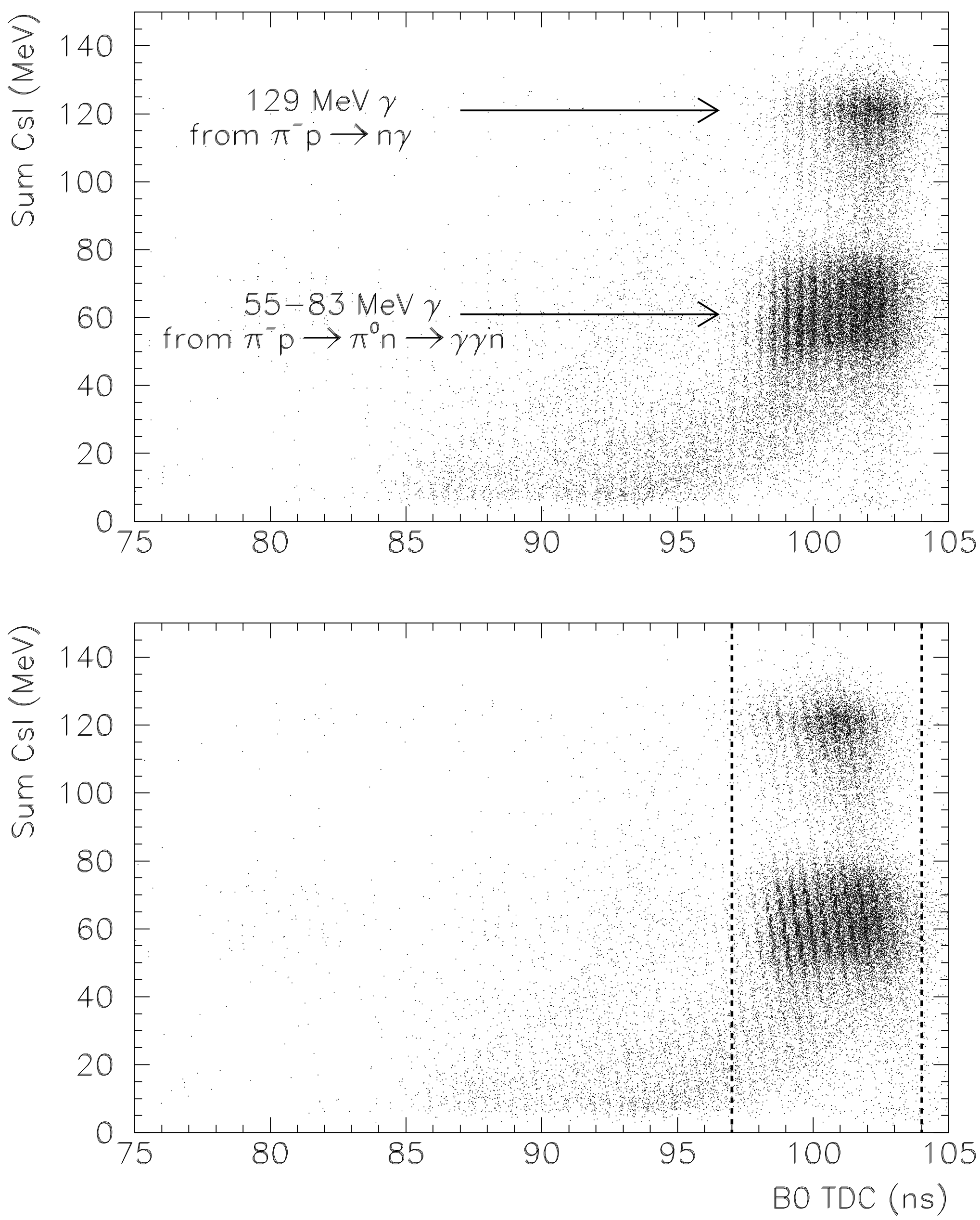

Figure 7.5: *Sum of 44 CsI ADC values plotted against the B0 TDC, before (top panel) and after (bottom panel) slewing correction for the single arm trigger configuration. Only events whose B0 TDC values are greater than 97 ns and less than 104 ns (dotted lines) are used in the extraction of the Panofsky Ratio value. Charged particle events are vetoed by the plastic hodoscope.*

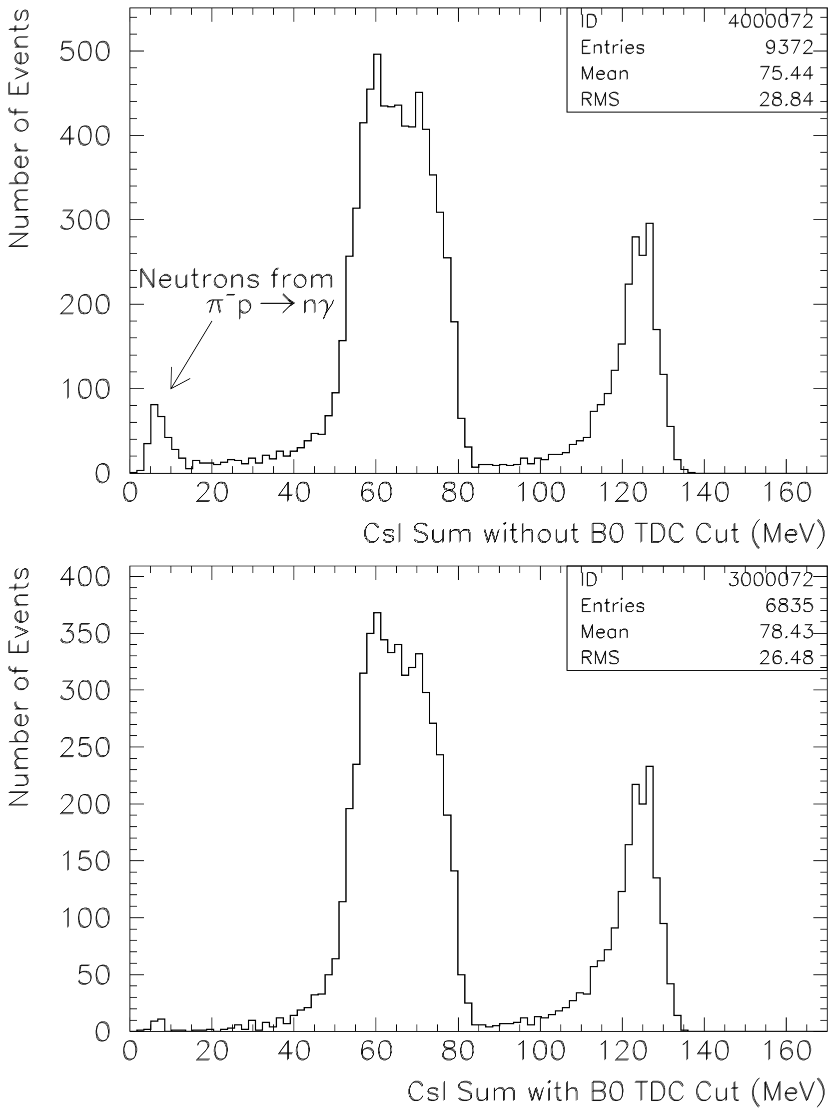

Figure 7.6: *The spectrum of photons from the $\pi^- p \rightarrow \pi^0 n \rightarrow \gamma\gamma$ and $\pi^- p \rightarrow n\gamma$ reactions, recorded with the single arm trigger configuration. The bottom panel includes the data timing cut on the B0 TDC spectrum (see Fig. 7.5), and the top panel does not. No more than 4% of the total energy is deposited outside the central six detectors. The residual low energy events in the bottom panel arise from from neutrons which are detected early by the B0 TDC.*

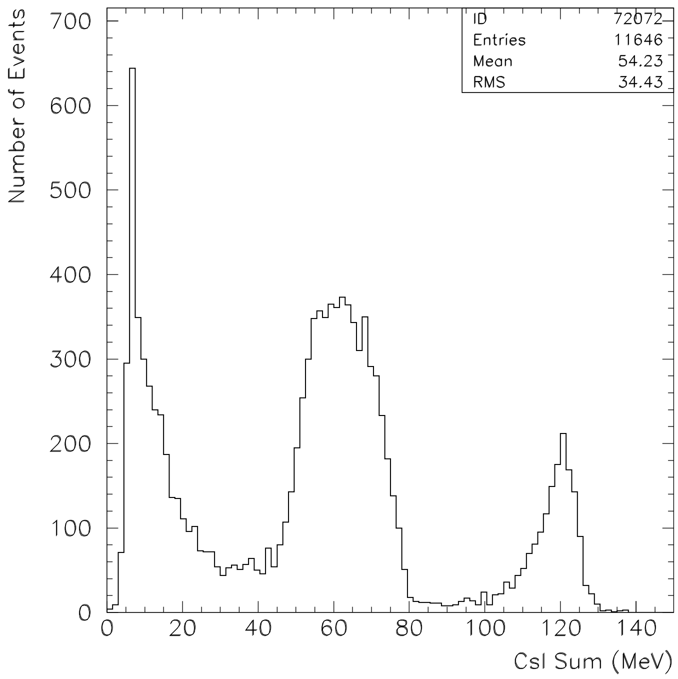

Figure 7.7: *Events for which the beam counter 'B0' TDC is less than 97.0 ns or greater than 104.0 ns. These events are excluded from the data set used in the Panofsky Ratio calculation.*

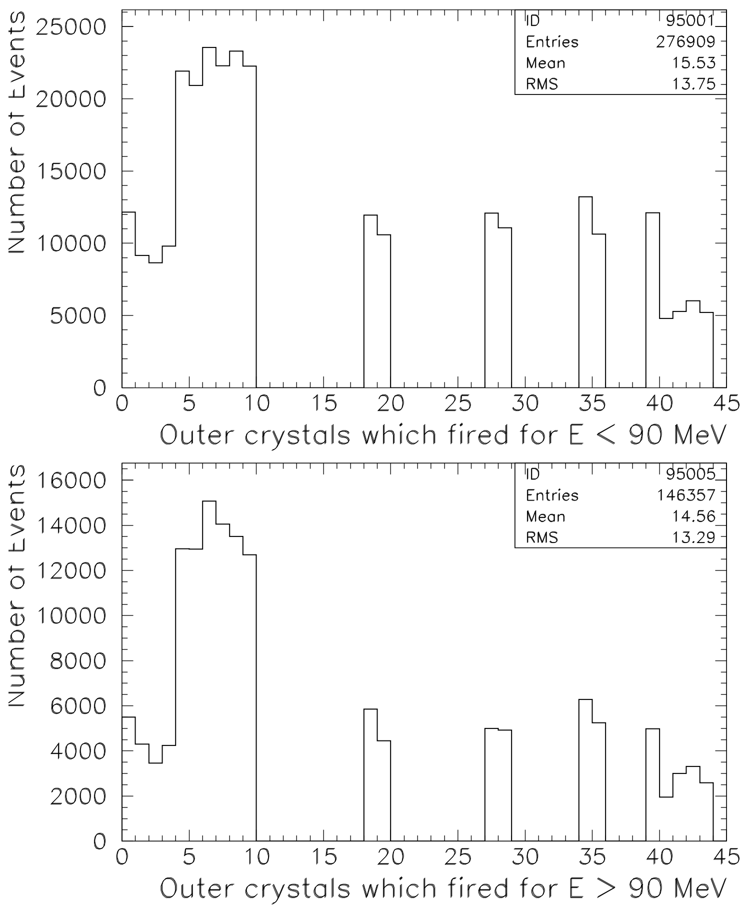

Figure 7.8: *Histograms showing count rates in outer detectors, for CsI Sum* $<$ *90 MeV (top panel) and CsI Sum* $>$ *90 MeV (bottom). A detector is determined to have fired if its ADC value is greater than a predetermined threshold (0.2 MeV). Detectors four through nine show an abnormally high counting rate, particularly in the bottom panel, when the total energy deposited into the calorimeter is greater than 90 MeV.*

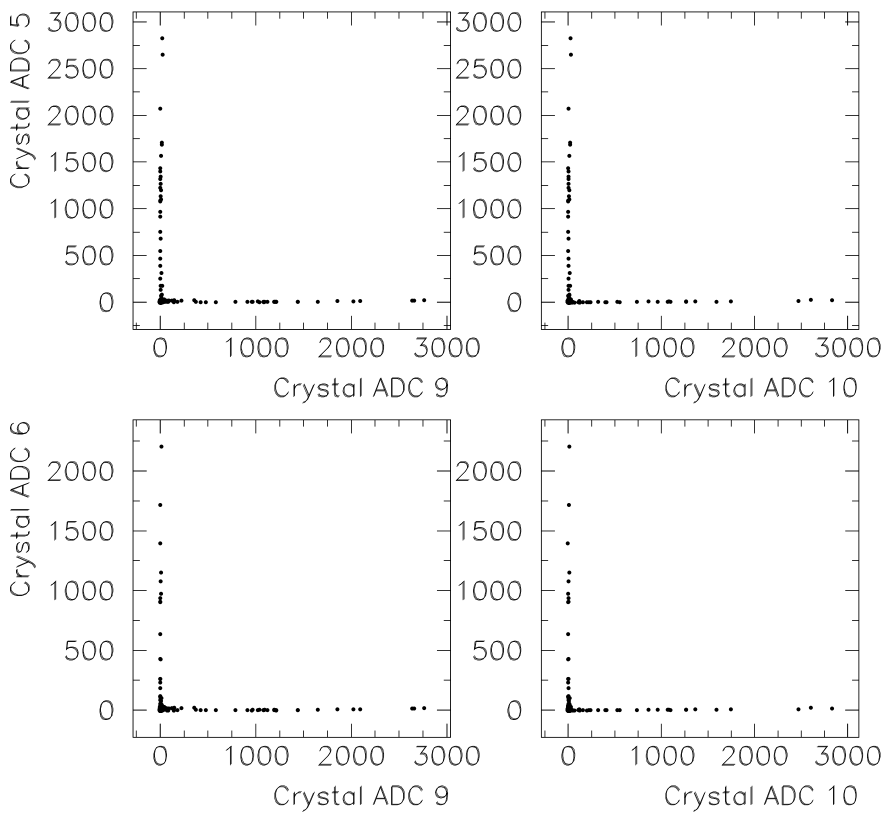

Figure 7.9: *ADC value correlation histograms between noisy detectors for the one arm trigger configuration. No correlation between these detectors is apparent, which rules out the possibility of cross talk.*

apparent.

Finally, one can inspect the raw ADC spectra, above 0.2 MeV, of two noisy outer detectors and two normal outer detectors in Fig. 7.10. The low energy noise is apparent in the spectra of detectors 8 and 9.

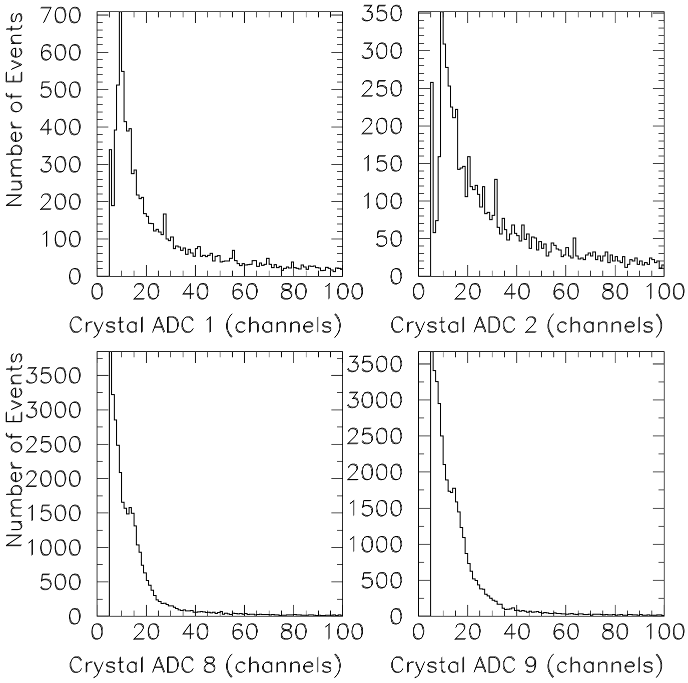

Figure 7.10: *CsI ADC spectra 0.2 MeV above the pedestal for two normal detectors (top panels) and two noisy detectors (bottom panels) for the single arm trigger configuration.*

7.2.3 Panofsky Ratio

In order to evaluate the Panofsky Ratio, defined in Chapter 1, the measured energy spectrum has been compared with the simulation obtained from the GEANT Monte Carlo simulation [7]. By varying the value of the Panofksy

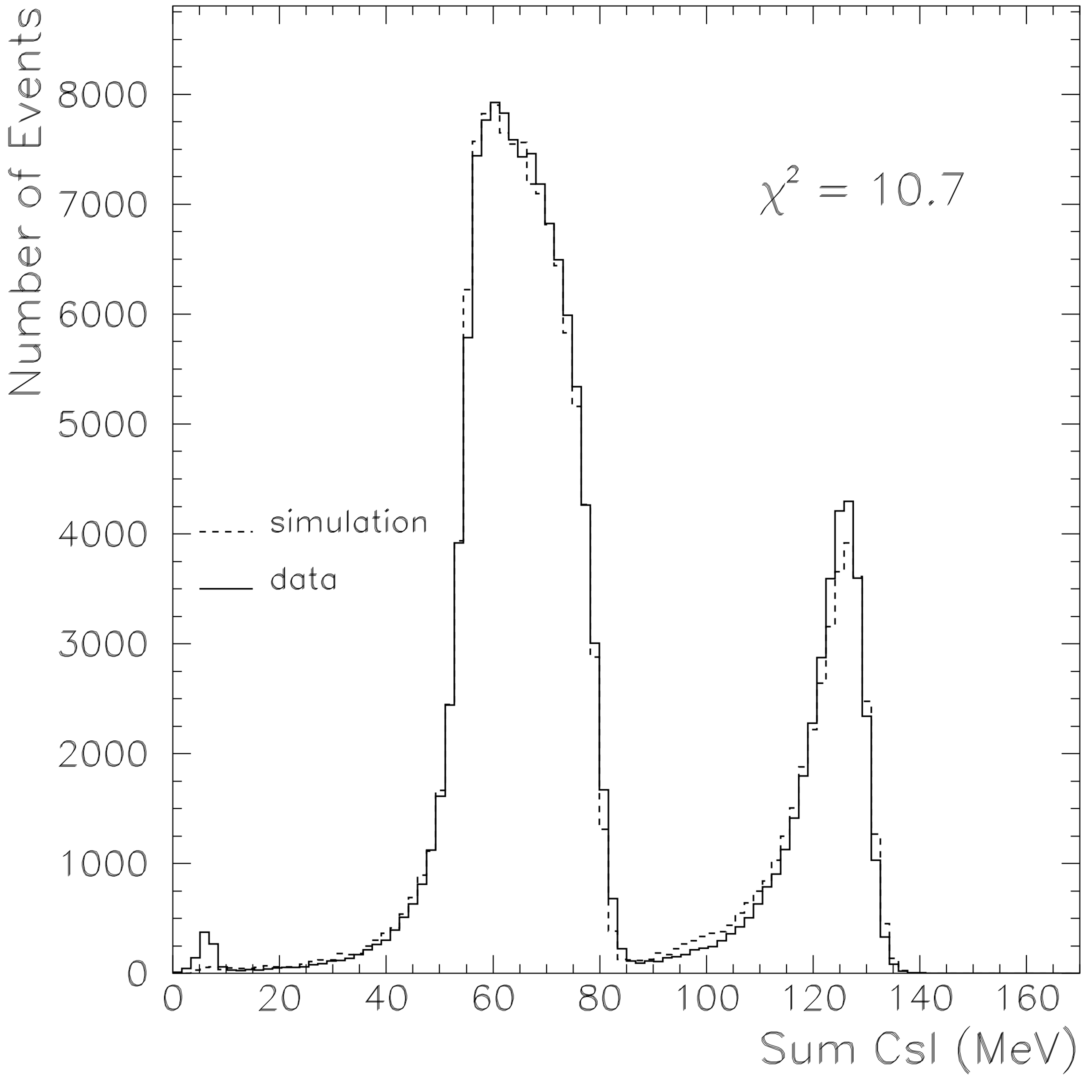

Figure 7.11: *Data (solid line) and simulation (dotted line) for the single arm trigger configuration. The Panofsky Ratio value used in the simulation is 1.49, with less than 4% of the total energy deposited outside the central six crystals. The χ^2 value is calculated for events which deposit more than 20 MeV into the calorimeter. Charged particle events are vetoed by the plastic hodoscope. The low energy feature represents residual neutrons which were not removed with the B0 TDC timing cut.*

Ratio entered into the simulation code, and optimizing the agreement with the data in terms of a minimum χ^2, one can deduce the most likely value for the Panofsky Ratio. Figure 7.11 shows an overlay of the experimental histogram and the simulated spectrum, both with the requirement that less than 4% of the total energy be deposited outside the central six crystals, for a Panofsky Ratio value of 1.5 .

In order to optimize the agreement between data and simulation, the total χ^2 value is calculated as

$$\chi^2 = \sum_i \frac{(S_i - D_i \times N_s/N_d)^2}{\sigma_i^2}, \tag{7.1}$$

where S_i is the number of events in bin i of the simulated spectrum, D_i is the number of events in bin i of the data spectrum, N_s is the total number of events in the simulated spectrum, and N_d that of the data spectrum. The standard deviation σ_i is taken to be the uncertainty of the data and simulation, combined in quadrature, such that

$$\sigma_i = \sqrt{\left(D_i \cdot \frac{N_s}{N_d} \times \frac{\sqrt{D_i}}{D_i}\right)^2 + \sqrt{S_i}^2} \tag{7.2}$$

$$= \sqrt{D_i \cdot \frac{{N_s}^2}{{N_d}^2} + S_i}. \tag{7.3}$$

Defined in this way, the χ^2 sum of the differences between experiment and simulation is minimized with respect to the simulated Panofsky Ratio. The "reduced χ^2" value is obtained by dividing the total χ^2 value by the number of degrees of freedom, which is equal to the number of bins in the histogram minus the number of variable parameters (one). A graph of the reduced χ^2 value plotted against the Panofsky Ratio is shown in Fig. 7.12. From the graph, the value of χ^2 is a minimum for a Panofsky Ratio of 1.49 . The uncertainty is taken to be the change in the Panofsky Ratio for a unit increase in the value of χ^2.

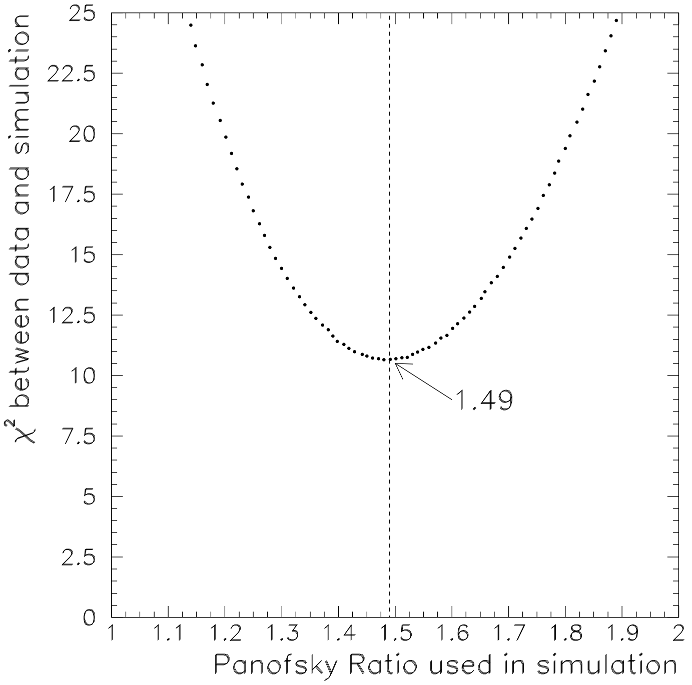

Figure 7.12: χ^2 *between the data and simulation plotted against the Panofsky Ratio value used in the GEANT simulation. The total* χ^2 *value is calculated according to Equ. 7.2.3. The analysis was performed for a minimum energy deposition of 20 MeV into the calorimeter (*E_0*=20 MeV), with less than 4% of the total energy deposited outside of the central six detectors.*

As discussed in Sec. 7.2.2, several of the outer detectors exhibit a large amount of low energy noise. Because the amount of this noise varies with the total energy deposited into the calorimeter, the Panofsky Ratio evaluation can be sensitive to the level of the veto energy threshold E_v placed on the detectors outside of the central six. Consequently, the summing threshold T_{CsI} defined in Sec. 4.1 has been raised to 1 MeV. Figure 7.13 shows the extracted value of the Panofsky Ratio plotted against E_v. From the graph, one can see that the Panofsky Ratio is constant with respect to E_v, for $E_v \lesssim 8\%$.

As mentioned in Sec. 7.2.1, the Panofsky Ratio should be evaluated above the energy threshold E_0 to avoid including events with significantly slewed timing in the analysis. This threshold should be varied to verify that the results are not sensitive to its value. Figure 7.13 shows the results for the analysis, done with four different values of E_0 ranging from 20 MeV to 50 MeV. The extracted value of the Panofsky Ratio in the region where more than 92% of the total energy is deposited in the central six crystals is 1.49$\pm$0.1.

As a final check in the analysis, it is useful to plot the reconstructed shower origin coordinates for the one arm trigger configuration in the data and in the simulation. With identical cuts imposed, the spatial reconstruction of the shower origins in the data and simulation should show good agreement. Figure 7.14 shows that agreement.

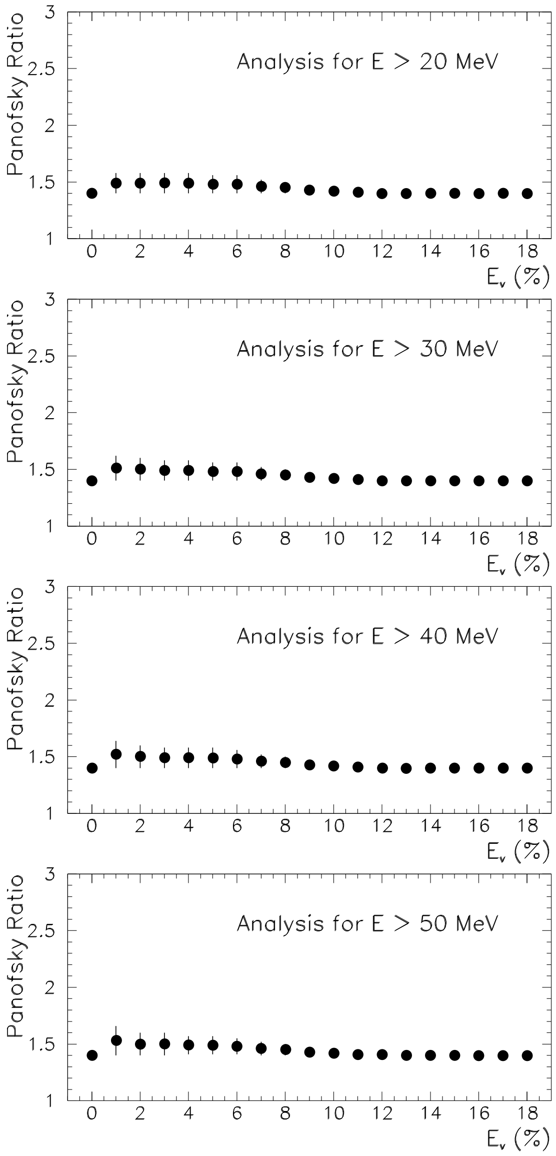

Figure 7.13: *The extracted Panofsky Ratio values plotted against the energy veto level E_v for crystals outside of the central six, evaluated for energies greater than four different values of the low energy threshold E_0.*

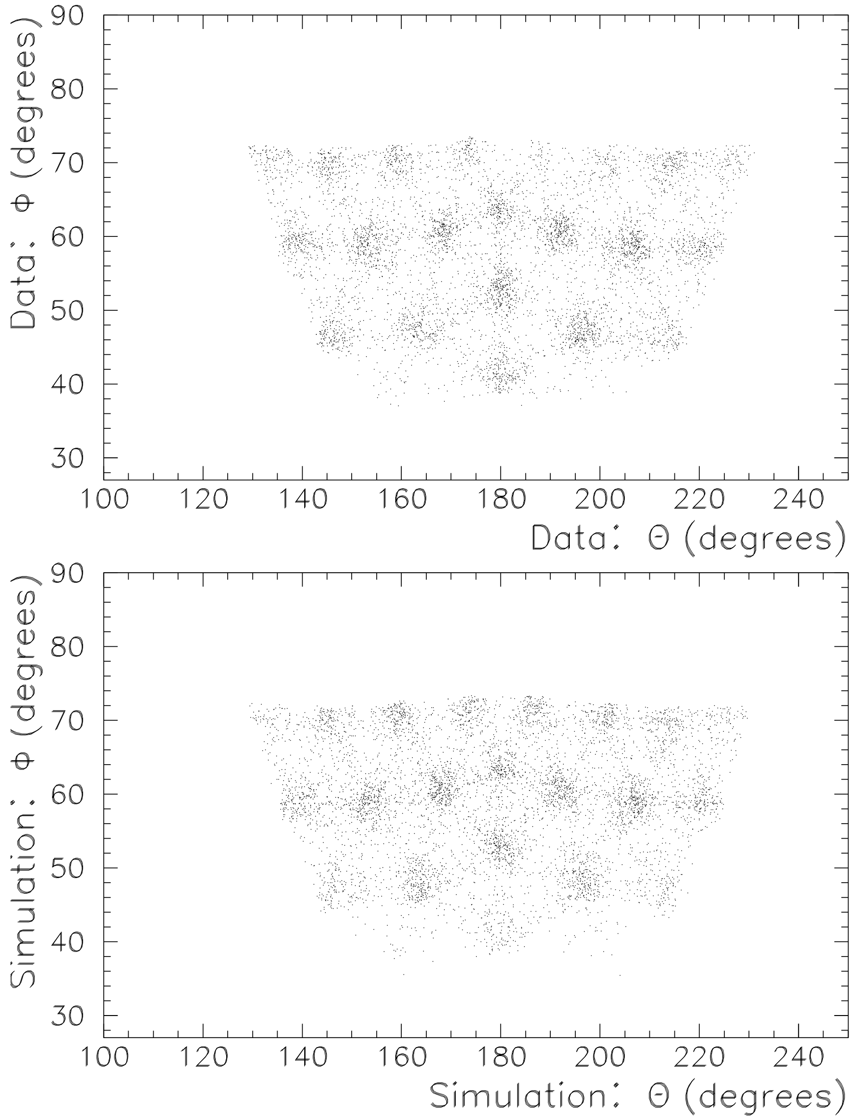

Figure 7.14: *Shower origin coordinates for the single arm trigger configuration. Charged particle events are vetoed by the plastic hodoscope. The top scatter plot represents the experimental data, and the bottom panel represents the simulation.*

Chapter 8

Conclusion

A precise measurement of the pion beta decay rate will provide the opportunity for stringent tests of the current Standard Model, specifically testing the Conserved Vector Current hypothesis and constraining the Cabbibo Kobayashi Maskawa quark mixing matrix. The relatively simple $0^+ \rightarrow 0^+$ transition of the pion beta decay, and the well understood radiative corrections, make this measurement a valuable and feasible task.

In the process of finishing construction of the PIBETA calorimeter, a measurement of the Panofsky Ratio has been made. This measurement is of interest because it connects the pion-nucleon scattering amplitude with the pion photoproduction amplitude, which facilitates the calculation of the former. By comparing information about the pion scattering amplitude derived from $\pi^{\pm}p$ scattering data with that obtained from the measured value of the Panofsky Ratio, one can test the principle of isospin symmetry in the πN system. The Panofsky Ratio value extracted from the 1997 measurement is 1.49$\pm$0.1, which agrees with the best measurement of 1.546$\pm$0.009. [19]

This Panofsky Ratio measurement is of use to the PIBETA collaboration because it can be compared with the known result, thereby providing a test of the performance of the CsI calorimeter. In addition, the products of the Panofsky

Ratio measurement include photons which are comparable in energy to those resulting from the pion beta decay reaction. Consequently, these photons have been used to determine the response of the PIBETA calorimeter in this energy range.

Because the Monte Carlo simulations of the experiments are crucial to the accurate extraction of the pion beta decay rate and the Panofsky Ratio, it is necessary to account for the light output and position-dependent nonuniformities of each CsI crystal in the calorimeter. These quantities have been measured using first cosmic muons and, most recently, 660 keV photons, and have been entered into the simulation as a smearing factor and a spatially dependent weighting function in the crystal energy depositions.

This spatially dependent weighting function has been shown to be most effective in the extraction of the Panofsky Ratio for events which are confined to the central six crystals of the forty-four element array. Because these six crystals were placed centrally for their exceptional light output uniformities, this would suggest that the Monte Carlo simulation has been more accurate in modeling the behavior of crystals with very uniform light reponses than otherwise. Consequently, it may be necessary to examine whether the tomography probe of 660 keV photons is sufficient to characterize the complete light reponse of the CsI crystals. However, a complete characterization may be unnecessary, because the final pion beta decay rate measurement involves photons and positrons with energies less than 70 MeV. These particles deposit their energy into regions of the CsI crystals which can be described adequately through tomography with the 660 keV photon probe.

Algorithms have been created for the absolute and relative energy calibration of the CsI crystals in the calorimeter. These algorithms have been shown to decrease the amount of noise in the data, as well as to improve the energy resolution of the calorimeter.

A shower reconstruction algorithm has been developed which locates the origin of the electromagnetic shower in the CsI and NaI arrays. Several parameters in the algorithm have been optimized to produce the best angular resolution. Geometric corrections have been applied based on the arrangement of the detectors. The resulting angular resolution is 1.8° and 1.2° for the CsI and NaI arrays, respectively.

A clustering algorithm has been tested which facilitates the study of optimal cluster size in the PIBETA calorimeter, for single particle final states in the 44-crystal array. The cluster size has been optimized with respect to energy resolution and event reconstruction efficiency. The optimal cluster size has been found to contain two rings of CsI crystals surrounding one central crystal.

Finally, with the calibrations and developments that have been presented here, a measurement of the pion beta decay should be feasible to within better than 0.5% accuracy.

Bibliography

[1] A. Bay, C. Joseph, J. F. Loude, J. P. Perroud, D. Ruegger, O. Schoeri, D. Steiner, and M. T. Tran. "A Modular NaI(Tl) Detector for Intermediate Energy Photons", *Nucl. Inst. Meth.* **A271** (1988) 497-506.

[2] Philip R. Bevington and D. Keith Robinson. *Data Reduction and Error Analysis for the Physical Sciences.* New York: McGraw-Hill Book Company, 1969.

[3] "BC-400 Premium Plastic Scintillator." *Bicron.* Online. Marinar Communications Group. 19 July 1998.

[4] "S83062E Photomultiplier." *Burle Industries Electron Tubes.* Online. LMI Web Communications. 19 July 1998.

[5] V. T. Cocconi, T. Fazzini, G. Fidecaro, M. Legros, N. H. Lipman, and A. W. Merrison. "A Redetermination of the Panofsky Ratio", *Il Nuovo Cimento* **22** (1961) 4194-4218.

[6] J. F. Crawford, M. Daum, R. Frosch, B. Jost, P. R. Kettle, R. M. Marshall, B. K. Wright, and K. O. H. Ziock. "Precision Measurement of the Pion Mass Difference $m_{\pi^-} - m_{\pi^+}$" *Phys. Rev. D* **43** (1991) 46.

[7] Application Software Group, Computing and Networks Division. *GEANT Detector Description and Simulation Tool.* CERN, Geneva, 1993.

[8] E. Frlež, I. Supek, K. A. Assamagan, C. Brönniman, T. Flügel, J. E. Koglin, B. Krause, D. W. Lawrence, D. Mzavia, D. Počanić, D. Renker, S. Ritt, M. E. Sadler, P. L. Slocum, N. Soić, B. K. Wright. "Cosmic Muon Tomography of Pure Cesium Iodide Crystals", to be submitted to *Nucl. Inst. and Meth. in Phys. Res. A.*

[9] G. Källén. *Elementary Particle Physics.* Reading, Massachusetts: Addison-Wesley Publishing Company, Inc., 1964.

[10] K. A. Assamagan. "A Precise Determination of the Pion Beta Decay Rate: Design and Calibration." *Diss.* University of Virginia, 1995.

[11] W. R. Leo. *Techniques for Nuclear and Particle Physics Experiments.* New York: Springer-Verlag, 1994.

[12] A. Sirlin. "General Properties of the Electromagnetic Corrections to the Beta Decay of a Physical Nucleon" *Phys. Rev.* **64** (1967) 1767-1775.

[13] W. J. Marciano and A. Sirlin. "Radiative Corrections to β Decay and the Possibility of a Fourth Generation" *Phys. Rev. Lett.* **56** (1986) 22-25.

[14] W. K. H. Panofsky, R. Lee Aamodt, and James Hadley. "The Gamma Ray Spectrum Resulting from Capture of Negative π^- Mesons in Hydrogen and Deuterium", *Phys. Rev.* **81** (1951) 565-574.

[15] D. Počanić, K. A. Assamagan, J. P. Chen, D. Day, E. Frlež, K. J. Keeter, R. M. Marshall, J. S. McCarthy, J. H. Mitchell, R. C. Minehart, B. E. Norum, O. A. Rondon-Aramayo, L. C. Smith, W. A. Stephens, B. K. Wright, K. O. H. Ziock, M. Daum, R. Frosch, D. Renker, T. Kozlowski, B. G. Ritchie, S. M. Korenchenko, N. A. Kuchinsky, N. P. Kravchuk, I. V. Kisel, A. S. Korenchenko, K. G. Nekrasov, D. B. Kozaikin, V. A. Baranov, A. Moiseenko, S. Jakovlev, Yu. Bagaturia, W. Djordjadze, D. Mzavia, G. Melitauri, T. Sachelashvili, A. Marušić, T. Petković, I. Supek, I.Šlaus, Ch. Broennimann, H. Pruys, R. Engfer. "A Precise Measurement of the $\pi^+ \to \pi^0 e^+ \nu$ Decay Rate". Proposal for Experiment, Paul Scherrer Institute, 1992.

[16] W. H. Press, S. A. Teukolsky, W. T. Vetterling, B. P. Flannery. *Numerical Recipes in C*, New York: Press Syndicate of the University of Cambridge, 1988.

[17] F. Foroughi. "piE1 Beam Line". *PSI Official WWW Home Page.* Online. Paul Scherrer Institute Internet. 19 July 1998.

[18] A. Sirlin, Letter to D. Počanić, 19 Mar. 1989.

[19] J. Spuller, D. Berghofer, M. D. Hasinoff, R. MacDonald, D. F. Measday, M. Salomon, T. Suzuki. "A Remeasurement of the Panofsky Ratio". *Phys. Lett.* **67B** (1977) 479-482.

[20] K.L. Brown, D.C. Carey, Ch. Iselin and F. Rothacker: Transport, a Computer Program for Designing Charged Particle Beam Transport Systems. See yellow reports CERN 73-16 (1973) and CERN 80-04 (1980).